

https://dspace.org/

Carbon with different functionalities as a hydrogen transport layer in ruthenium promoted Fischer -Tropsch catalysts

Buthelezi, Thuli Innocentia

2019-02

https://hdl.handle.net/10539/29593

Downloaded from a DSpace repository. https://dspace.org/



UNIVERSITY OF THE
WITWATERSRAND,
JOHANNESBURG

Carbon with different functionalities as a hydrogen transport layer in ruthenium promoted Fischer -Tropsch catalysts

---

Thuli Innocentia Buthelezi

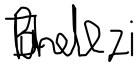
1778452

A thesis submitted to the School of Chemistry, Faculty of Science, University of the Witwatersrand, Johannesburg, in fulfilment of requirements for the Degree of Masters of Science.

February, 2019

Declaration

I hereby declare that the work reported in this thesis is my own unaided work. It is being submitted to the Faculty of Science, University of the Witwatersrand, Johannesburg, in fulfilment of requirements for the Masters of Science.


_____ on this ____ day of 20/08/19

(Candidate)

Abstract

Fischer-Tropsch synthesis (FTS) is the catalytic production of hydrocarbons from synthesis gas (carbon monoxide and hydrogen) which is derived from biomass, coal or oil. Cobalt (Co) is a highly active and selective metal catalyst used in FTS. Two ways of improving the activity of a Co catalyst are (i) by adding a Ru promoter and (ii) by using defective carbon (nitrogen doped carbon) as a support. A Ru promoter increases the activity of a Co catalyst by reducing a Co precursor at lower temperature through hydrogen spillover, which involves the transfer of hydrogen from a Ru surface to a Co precursor surface. A nitrogen doped carbon support provides stability to the Co nanoparticles and prevents particle agglomeration. Furthermore, the electron-rich nitrogen groups can enhance the electronic conductivity of the carbon support thus potentially improving hydrogen spillover.

In this study we used nitrogen doped hollow carbon spheres (NHCSs) as a carbon support for Ru (0.5%) promoted Co (10% and 15%) catalysts. The Co catalysts were synthesized by the hard templating method, using polystyrene as the hard template. The use of the NHCSs as a support allowed for the separation of the locations of the Co metal and the Ru metal, thus enabling hydrogen spillover studies. The study also explored the effect of varying synthesis parameters such as annealing time and the type of nitrogen doping (in situ nitrogen doping and post nitrogen doping) used on the hydrogen spillover effect. The supported catalysts were structurally characterized using a range of techniques; TEM, SEM, PXRD, TGA, Raman, BET, XPS and CHNS analyses. The reducibility of the catalysts was assessed using TPR analysis and in situ PXRD analysis. In preliminary studies, the activity of the catalysts was tested under low temperature FTS conditions.

TEM studies showed that polystyrene was a good and stable template for synthesizing the NHCSs as the formed carbon support was spherical and had a hollow morphology. The NHCSs had average diameters of 380 nm and shell thickness of 40 nm. The NHCSs was a good support and the hollow core effectively stabilized the Co and Ru metal nanoparticles as they were obtained in small sizes with narrow particle size distributions (Co@NHCS, 6.2 nm; Co@NHCS@Ru, 6.2 nm catalyst; Co-Ru@NHCS 4.5 nm). CHNS analysis and XPS analysis confirmed the successful presence and incorporation of N-atoms (5% - 7%) within the carbon matrix by a post doping method. Furthermore, XPS analysis confirmed that pyridinic-N, pyrrolic-N, quaternary-N and oxidised-N were present within the carbon matrix. BET

analysis showed the surface area of the NHCSs to be 188 m^2/g and those of the Co catalysts to be lower (143 m^2/g - 102 m^2/g) due to the blockage of the pores by nanoparticles and by the bulky nitrogen groups. All the catalysts have a mesoporous shell (2.5 nm - 4.7 nm). PXRD studies showed that the carbon was amorphous in nature (broad XRD peak; 22.3 °) and that the cubic spinel phase Co_3O_4 was formed. TGA studies showed that the NHCSs were more stable against oxidation than supported Co catalysts and this was attributed to the ability of Co_3O_4 nanoparticles to catalyse the oxidation of the carbon support.

The TPR analysis revealed that the direct contact between Co and Ru (Co-Ru@NHCS) promoted a primary hydrogen spillover effect ($Co_3O_4 \rightarrow$Co, 269 °C) whereas indirect contact (Co@NHCS@Ru) slightly enhanced the secondary hydrogen spillover effect ($Co_3O_4 \rightarrow$CoO, 347 °C; CoO→Co, 420 °C). In situ PXRD studies were in agreement with the TPR studies showing that the presence of direct contact between Co and Ru gave the highest degree of reduction (99 %) compared to indirect contact (97 %) and the unpromoted (59 %) Co catalyst. The high degree of reduction was due to the hydrogen spillover effect. Furthermore, the presence of Ru improved the relative abundance of the Co_{hcp} phase.

The TEM images of the Co catalysts supported inside the in situ nitrogen doped hollow carbon support (Co@NHCSI) showed good dispersion. The catalyst also showed the lowest oxidation (TGA analysis) and improved Co oxide reduction (TPR analysis) due to the nitrogen defects being present throughout the carbon matrix.

The preliminary results of the Fischer-Tropsch synthesis process showed that the unpromoted Co@NHCS catalyst had a higher CO conversion and catalytic activity than the promoted Co-Ru@NHCS catalyst. The low activity of the Co-Ru@NHCS catalyst could be attributed to low mass diffusion issues.

Dedication

Dedicated to:

- My late grandmother and best friend, may you rest in eternal peace T. J. Buthelezi.
- My pillars of strength, Z. M. Buthelezi and L. P. Buthelezi.

Acknowledgements

I would to give my highest praise to my creator, the Almighty God, thank You for giving me the gift of life.

My supervisor Professor Neil. J. Coville, thank you for your support, wisdom and guidance throughout my MSc journey. May God continue to bless you!

My co-supervisors; Dr Forbes, thank you for your assistance with the in situ PXRD analysis and interpretation of the results. Dr Linganiso, thank you for your guidance and motivation.

A big thank you to Dr Tumelo Phaahlamohlaka, Dr William Dlamini and Dr Bridget Mutuma thank you for your assistance and guidance with the synthesis and catalyst testing (FTS) processes.

My friends and colleagues; Dr Prakash Gangatharan, Alice Magubane, Pumza Mente, Victor Mashindi, Thomas Mongwe, Boitumelo Tlhaole, Xiluwa Mathebula, thank you all for the assistance. None of our conversations and advice went unnoticed. I appreciate you all, very much! A special thank you goes to Joy “my JoyJoy” Masilo, for being a supportive friend throughout the research process.

A great thank you to Prof Ziegler, Dr Manoko, Dr Tetana, Dr Linganiso, Dr Reddy and Mr Gerber, from the Microscopy and microscopy unit (MMU) for instrument trainings as well as for the assistance. Thank you to Mr Jordaan for the assistance with XPS analysis and Ms Monyai for the assistance with CHNS analysis.

Thank you to all the CATMAT group members, may we continue to grow and motivate each other.

Last but not least, I would like to thank SASOL for the financial support and Ms Mokgothu for her guidance.

Presentations and publications

Presentations

- T. I. Buthelezi, R. P. Forbes, L. Z. Linganiso, N. J. Coville, CATSA conference, "Carbon with different functionalities as a hydrogen transport layer in ruthenium promoted Fischer -Tropsch catalyst", November 2017.
- T. I. Buthelezi, R. P. Forbes, L. Z. Linganiso, N. J. Coville, CATSA conference, "Carbon with different functionalities as a hydrogen transport layer in ruthenium promoted Fischer -Tropsch catalyst", November 2018.
- T. I. Buthelezi, R. P. Forbes, L. Z. Linganiso, N. J. Coville, MSSA workshop, "Carbon with different functionalities as a hydrogen transport layer in ruthenium promoted Fischer -Tropsch catalyst", December 2018.

Publications

- T. I. Buthelezi, R. P. Forbes, L. Z. Linganiso, N. J. Coville, The use of N doped hollow carbon spheres to study spillover effects in Ru promoted Co catalysts. *In preparation*

List of figures

Figure 2.1 The hydrogen spill over process on a nitrogen doped carbon support.

Figure 2.2 The schematic representation of the FTS process from feedstocks to products

Figure 2.3 Various allotropes of carbon that are used as supports

Figure 2.4 A FTS reaction occurring in a nanoreactor and on a conventional oxidic support

Figure 2.5 Schematic representation of the synthesis of HCSs by hard templating

Figure 2.6 Nitrogen configurations incorporated into the carbon matrix.

Figure 2.7 Diagrammatic presentation of the hydrogen spillover process, detailing primary and secondary spillover

Figure 2.8 Schematic diagram of the production of the proton and electron upon adsorption of H_2 on Pt and subsequent spillover of H atoms to the reducible WO_3 support

Figure 2.9 Cost of various electronic promoters

Figure 2.10 Hydrogen spillover on carbon supports through surface diffusion

Figure 2.11 Presentation of the degree of reduction on a non-non-reducible support

Figure 3.1 Schematic representation of the synthesis methodology

Figure 3.2 Bragg's schematic and a typical setup on an XRD diffractometer

Figure 3.3 The Bruker D2 Phaser PXRD fitted with a LynxEye detector

Figure 3.4 Perkin Elmer TGA 6000 thermal analyser

Figure 3.5 Micromeritics RS232 Brunauer -Emmett-Teller (BET) analyser

Figure 3.6 Bruker Senterra Laser Raman spectrometer

Figure 3.7 Schematic of main components found in a TEM instrument

Figure 3.8 The FEI TECNAI T12 transmission electron microscope

Figure 3.9 Schematic of main components found in a SEM instrument

Figure 3.10 The FEI Nova Nanolab 600 FEG-SEM/FIB

Figure 3.11 The Micromeritics AutoChem II

Figure 3.12 A Bruker D8 Advance AXS diffractometer

Figure 3.13 A schematic illustration of the rig reactor design

Figure 3.14 A GC-TCD trace recorded during syngas calibration

Figure 3.15 A GC-FID trace recorded during six gas mixture calibration

Figure 3.16 A GC-TCD trace recorded during six gas mixture calibration

Figure 4.1 Structure of a hollow carbon sphere with a porous shell

Figure 4.2 Schematic representation of the synthesis methodology

Figure 4.3 SEM image with PSD, TEM image, PXRD pattern and TGA with DTG for polystyrene spheres

Figure 4.4 TEM and SEM image of N-doped hollow carbon spheres

Figure 4.5 TEM images with respective particle size distributions of the catalysts

Figure 4.6 PXRD patterns and TGA profiles of catalysts

Figure 4.7 Raman spectra of catalysts and survey XPS spectra of 10% Co@NHCS and survey XPS spectra of NHCSs

Figure 4.8 N_2 adsorption-desorption isotherm and the corresponding adsorption pore size distribution for NHCS

Figure 4.9 TPR reduction profiles for Co catalysts and catalyst support

Figure 4.10 PXRD patterns of Co catalysts, reduced in H_2 gas at 450 ^{o}C for 3 hours

Figure 4.11 Degree of reduction for Co catalysts

Figure 4.12 Schematic representation of the synthesis methodology

Figure 4.13 TEM images of catalyst supports and supported catalysts with corresponding metal particle size distribution when annealed for 1 hour

Figure 4.14 PXRD patterns and TGA profiles of catalysts

Figure 4.15 XPS N1s deconvulated spectra for the catalyst supports

Figure 4.16 TPR profile for supported catalysts

Figure 4.17 Schematic representation of the synthesis methodology

Figure 4.18 TEM images and particle size distributions of the supported catalysts

Figure 4.19 PXRD spectra and TGA thermographs of the catalysts

Figure 4.20 TPR profiles of supported catalysts

Figure 5.1 CO conversion (%) as a function of time in FTS of Co catalysts at different FTS temperature

Figure 4S.1 SEM images with respective EDX spectra of catalysts

Figure 4S.2 Derivative TGA profiles of catalysts

Figure 4S.3 N_2 adsorption-desorption isotherm and the corresponding adsorption pore size distribution for catalysts

Figure 4S.4 Derivative TGA profiles of catalysts annealed for 1 hour

Figure 4S.5 Derivative TGA profiles of catalysts annealed for 2 hours

Figure 4S.6 Derivative TGA profiles of catalysts supported inside the in situ nitrogen doped carbon and on the post nitrogen doped carbon

Figure 4S.7 TPR profiles of catalysts supported (**A &B**), $Co@NHCS_{1hr.}$

List of tables

Table 2.1 FTS reaction conditions and product selectivity

Table 2.2 Synthesis technique and conditions for nanoreactors

Table 2.3 Nitrogen doping methods, precursors and nitrogen content on carbon materials

Table 3.1 The GC operating conditions during synthesis

Table 3.2 The equations used in the FTS calculations

Table 3.3 The equations used in the FTS calculations

Table 4.1 Decomposition temperature, metal loading and particle size of catalysts

Table 4.2 The nitrogen content and Raman spectroscopy data

Table 4.3 BET surface area, pore size and pore volume data

Table 4.4 TPR reduction peak positions of catalysts and catalyst support

Table 4.5 PXRD patterns of Co catalysts, reduced in H_2 gas at 450 ^oC for 3 hours

Table 4.6 Thermal decomposition temperature, Co loading and Co particle size of the catalysts

Table 4.7 Nitrogen content, nitrogen cofiguration and Raman data of catalysts

Table 4.8 Surface areas, pore volume and pore size of catalyst supports and supported catalysts

Table 4.9 TPR reduction peak positions of Co catalysts

Table 4.10 Thermal decomposition temperature, metal loading, elemental content and Raman data of catalyst

Table 4.11 Surface area, pore volume and pore size of the catalysts

Table 4.12 TPR reduction peak positions of supported Co catalysts

Table 5.1 CO conversions, activity and selectivity of Co catalysts under FTS reaction

Table 4S.1 Co phases obtained for different supported Co catalysts, reduced in H_2 gas at 450 ^{o}C for 3 hours

List of abbreviation, nomenclatures and symbols

Abbreviation	*Description*
BET	Brunauer–Emmett–Teller
CHNS	Carbon, hydrogen, nitrogen and sulphur
CTAB	Hexadecyltrimethylammonium bromide
CVD	Chemical vapour deposition
FID	Flame ionization detector
fcc	Face-centered-cubic
FTS	Fischer-Tropsch synthesis
hcp	Hexagonal-close-packed
HTC	Hydrothermal catrbonization
HTFT	High temperature FTS
KPS	Potassium persulfate
LTFS	Low temperature FTS
NHCSs	Nitrogen doped hollow carbon spheres
PSSs	Polystryrene spheres
PVP	Polyvinylpyrollidone
PXRD	Powder X-ray diffraction
RF	Resorcinol-formaldehyde
SEM	Scanning electron microscopy
TCD	Thermally conductivity detector
TEM	Transmission electron microscope
TGA	Thermal gravimetric analysis
TPR	Temperature programmed reduction
XPS	X-ray photoelectron spectroscopy
FWHM	Full width at half maximum
WI	Wetness impregnation

Table of Contents

Declaration i

Abstract ii

Dedication iv

Acknowledgements v

Presentations and publications vi

List of figures vii

List of tables x

List of abbreviation, nomenclatures and symbols xii

CHAPTER 1 1

Introduction 1

1.1. Background/ Motivation of the study 1

1.2. Aims and objectives 2

1.2.1. Aims 2

1.2.2. Objectives 2

1.3. Dissertation outline 3

1.4. References 3

CHAPTER 2 8

Literature review 8

2.1. Introduction. 8

2.2. Fischer-Tropsch synthesis. 10

2.2.1. Background. 10

2.2.2. Cobalt FTS catalysts 13

2.2.3. Hollow carbon spheres: nanoreactors as support for FTS. 14

2.2.4. Synthesis methods used to make HCSs. 15

2.2.5. Structural modification of HCSs: nitrogen doping 18

2.3. Hydrogen spillover: promotion effects on Co Fischer-Tropsch catalysts. 20

2.3.1. Overview of hydrogen spillover. 20

2.3.2. Promotion of supported Co catalysts: Co-Ru systems for hydrogen spillover. 22

2.3.3. Efficiency of hydrogen spillover on carbon supports: effect of defects and distance. **24**
2.4. Concluding remarks **26**
2.5. References **26**
CHAPTER 3 **33**
General experimental methods and Fischer-Tropsch reactor conditions. **33**
3.1. Introduction **33**
3.2. Synthesis methodology **34**
3.2.1. Materials **34**
3.2.2 Synthesis of nitrogen doped hollow carbon spheres **34**
3.3. Material characterization techniques. **38**
3.3.1. Powder X-ray diffraction (PXRD). **38**
3.3.2. Thermal gravimetric analysis (TGA). **39**
3.3.3. Brunauer, Emmet and Teller (BET) method. **40**
3.3.4. Laser Raman spectroscopy. **41**
3.3.5. Transmission electron microscopy (TEM). **42**
3.3.6. Scanning electron microscopy (SEM). **44**
3.3.7. X-ray photoelectron spectroscopy (XPS). **46**
3.3.8 Carbon, hydrogen, nitrogen (CHN) analysis. **46**
3.4. Catalyst reducibility studies. **47**
3.4.1. Temperature programmed reduction (TPR). **47**
3.4.2. In situ powder X-ray diffraction (in situ PXRD). **48**
3.5. Catalyst testing: reactor set-up and equations. **49**
3.5.1. Fischer-Tropsch synthesis reactor set-up. **49**
3.5.2. Catalytic experiments. **50**
3.5.3. Instrument calibration and product analysis. **50**
3.5.4. Fischer-Tropsch synthesis conditions **54**
3.5.5. Mass balance equations: catalyst activity and selectivity. **55**
3.6. References **56**
CHAPTER 4 **59**
The study and characterization of cobalt and ruthenium nanoparticles encapsulated in N-doped hollow carbon spheres: evaluation of N-doped HCSs as a hydrogen transport layer and as a nanoreactor. **59**
4.1. The evaluation of N-doped HCSs as a support for Co and Ru nanoparticles. **59**
4.1.1. Introduction. **59**
4.1.2. Methodology. **61**

4.1.3. Characterization. **62**
4.1.4. Results and discussion. **63**
4.1.5. Conclusions. **79**
4.2. Synthesis of N-doped hollow carbon spheres: effect of annealing time. **81**
4.2.1 Introduction. **81**
4.2.2. Methodology and characterization. **81**
4.2.3. Results and discussion **82**
4.2.4. Conclusions. **92**
4.3. Synthesis of N-doped hollow carbon spheres: in situ doping versus post doping. **93**
4.3.1. Introduction. **93**
4.3.2. Methodology and characterization. **93**
4.3.3. Results and discussion. **95**
4.3.4. Conclusions. **103**
4.4. References **103**
CHAPTER 5 **108**
Fischer-Tropsch synthesis:Preliminary catalyst testing studies **108**
5.1. Introduction. **108**
5.2. Evaluation of FTS performance. **109**
5.2.1. Fischer-Tropsch synthesis: Catalyst evaluation. **109**
5.2.2. Conclusions **112**
5.3. References **113**
CHAPTER 6 **114**
Conclusions and recommendations **114**
6.1 Conclusions **114**
6.2. Recommendations **115**
Appendix **117**
Chapter 4: Supporting information **117**

CHAPTER 1

Introduction

1.1. Background/ Motivation of the study

Hollow carbon spheres (HCSs) have been found to be useful and stable support materials [1-4] for cobalt (Co) catalysts in Fischer-Tropsch synthesis [5-7] (FTS) reactions. The success of HCSs as applicable supports can be attributed to their tuneable properties which can be achieved by modifying their inner diameters [8-10], shell thickness [11-15], porosity [16-18] and surface functionalization [19-23].

Pristine supports made of carbon allow for high dispersion of nanoparticles, can facilitate mass transfer of the reactants/products and offer limited support-to-metal interactions. These effects can be attributed to the high surface area, porosity and inertness of carbon. These properties allow for catalysts to maintain high catalytic activity and selectivity during low-temperature Fischer-Tropsch synthesis (FTS), where they facilitate the hydrogenation of carbon monoxide. The activity of supported Co catalysts can be further enhanced by electronic promotion [24-25] of a cobalt catalyst precursor. Electronic promotion of a catalyst is obtained by the addition of small amounts of noble metals such as ruthenium (Ru) [26-28], rhodium (Rh) [29-31] or platinum (Pt). [32-34] Ru has a high affinity towards hydrogen dissociation and facilitates low temperature reduction of a cobalt precursor through a process known as hydrogen spillover. [35-40] Briefly, upon dissociation of the hydrogen molecule by the promoter metal, the activated hydrogen species diffuse, directly or indirectly, to the cobalt precursor and hence reduce it to the active cobalt metal phase.

However, inevitable sintering of Co nanoparticles supported on pristine carbon supports during calcination treatment is one major obstacle incurred in the catalyst preparations steps. Additionally, pristine carbon supports facilitates limited hydrogen diffusion when the contact of the metal catalyst and the promoter is indirect. This effect can be attributed to limited electronic conductivity within the pristine carbon matrix[35, 36, 38, 39], thus requiring more energy (high temperature) for the reduction process to occur. These effects have called for the optimization studies of catalysts with improved activity.

Doping [41-45] of carbon supports through the incorporation of dopants/defects such as nitrogen (N) [46-50], boron (B) [51-53] and sulphur (S) [54-56] into the carbon matrix has been found to alter the electron conductivity of a carbon support. The comparable size between carbon and nitrogen allows for ease of nitrogen doping. [57- 58] Nitrogen precursors such as melamine [59-61] and ammonia [62-64] have been found to successfully incorporate nitrogen with different nitrogen configuration into a carbon matrix and to enhance the electronic conductivity of the of carbon supports. Nitrogen as an electron donor, has an available lone pair of electrons, helps to anchor Co nanoparticles and thus enhances metal dispersion and limits sintering effects.

To study the effect of N-doping on the spillover effect we have used nitrogen doped hollow carbon spheres as a support. The focus was to assess the effect of nitrogen on the hydrogen spillover in the Ru promoted Co FT catalysts.

1.2. Aims and objectives

1.2.1. Aims

The proposed study aimed to synthesize nitrogen doped hollow carbon spheres (NHCSs) using a polystyrene template and to use the NHCSs as a model catalyst support for a Ru promoted Co FT catalyst. A primary consideration was to investigate the effect of the presence of nitrogen on the carbon support on the hydrogen spillover during activation of a low temperature Co FTS catalyst.

1.2.2. Objectives

The specific objectives of the study were;

1. To synthesize Co/Ru catalysts encapsulated inside the NHCSs and characterize them using various analytical techniques (TGA, PXRD, TEM, SEM, BET, XPS and Raman spectroscopy).

2. To study the effect that annealing time and nitrogen doping method has on the hydrogen spillover process.

3. To study the reduction behaviour of the supported catalysts using the temperature programmed reduction (TPR) technique as well as in situ powder X-ray diffraction. The TPR study will allow for the delineation between primary and secondary hydrogen spillover effects, thus allowing for elucidation of a mechanism for the Co oxide promotion. The in situ PXRD will provide the degree of reducibility of the catalysts and the resultant Co phase.

4. In preliminary studies, to assess the catalytic activity and selectivity of the supported catalyst during low temperature Fischer-Tropsch reaction conditions.

1.3. Dissertation outline

Chapter 1 is the introductory chapter presenting, the problem statement, the background, motivation, aims and objectives of the undertaken study.

Chapter 2 presents a detailed literature review on the application of modified carbon-based supports, the promotion of Co catalysts and mechanistic information of the hydrogen spillover in FTS catalysts.

Chapter 3 presents details of the synthesis procedures and characterization techniques used to characterize catalysts. This chapter also details the FTS reactor set-up and calculation procedure used.

Chapter 4 presents the effect of nitrogen incorporation into the support framework, the effect of annealing time and the effect of the nitrogen doping process (in situ doping versus post doping) on the hydrogen spillover process.

Chapter 5 assesses the catalytic activity of the Ru promoted and the unpromoted Co catalyst supported inside the NHCSs.

Chapter 6 gives concluding remarks of the study and recommendations for the future use of modified supports in hydrogen spillover and FTS studies.

1.4. References

1. Li, S.; Pasc, A.; Fierro, V.; Celzard, A. *Journal of Materials Chemistry A* **2016**, *4* (33), 12686–12713.
2. Kim, M.; Yoon, S. B.; Sohn, K.; Kim, J. Y.; Shin, C. H.; Hyeon, T.; Yu, J. S.

Microporous and Mesoporous Materials **2003**, *63* (1–3), 1–9.

3. Wang, G.; Wang, R.; Liu, L.; Zhang, H.; Du, J.; Zhang, Y.; Liu, M.; Liang, K.; Chen, A. *Materials Letters* **2017**, *197*, 71–74.
4. Hu, F. P.; Wang, Z.; Li, Y.; Li, C.; Zhang, X.; Shen, P. K. *Journal of Power Sources* **2008**, *177* (1), 61–66.
5. Xiong, K.; Li, J.; Liew, K.; Zhan, X. *Applied Catalysis A: General* **2010**, *389* (1–2), 173–178.
6. Pirola, C.; Scavini, M.; Galli, F.; Vitali, S.; Comazzi, A.; Manenti, F.; Ghigna, P. *Fuel* **2014**, *132*, 62–70.
7. Phaahlamohlaka, T. N.; Kumi, D. O.; Dlamini, M. W.; Forbes, R.; Jewell, L. L.; Billing, D. G.; Coville, N. J. *ACS Catalysis* **2017**, *7* (3), 1568–1578.
8. Mezzavilla, S.; Baldizzone, C.; Mayrhofer, K. J. J.; Schüth, F. *ACS Applied Materials and Interfaces* **2015**, *7* (23), 12914–12922.
9. Wang, C. W.; Liu, K. W.; Chen, W. F.; Zhou, J. De; Lin, H. P.; Hsu, C. H.; Kuo, P. L. *Inorganic Chemistry Frontiers* **2016**, *3* (11), 1398–1405.
10. Zhang, H.; Noonan, O.; Huang, X.; Yang, Y.; Xu, C.; Zhou, L.; Yu, C. *ACS Nano* **2016**, *10* (4), 4579–4586.
11. Fang, X.; Zang, J.; Wang, X.; Zheng, M. Sen; Zheng, N. *Journal of Materials Chemistry A* **2014**, *2* (17), 6191–6197.
12. Liu, H.; Li, W.; Shen, D.; Zhao, D.; Wang, G. *Journal of the American Chemical Society* **2015**, *137* (40), 13161–13166.
13. Zhang, Y.; Zhao, Z.; Chen, J.; Cheng, L.; Chang, J.; Sheng, W.; Hu, C.; Cao, S. *Applied Catalysis B: Environmental* **2015**, *165*, 715–722.
14. Tang, J.; Liu, J.; Salunkhe, R. R.; Wang, T.; Yamauchi, Y. *Chemical Communications* **2015**, *52* (3), 505–508.
15. J. Hou, T. Cao, F. I. and C. C. *Nanoscale* **2016**, *8*, 451–457.
16. Yan, Z.; Xie, J.; Zong, S.; Zhang, M.; Sun, Q.; Chen, M. *Electrochimica Acta* **2013**, *109*, 256–261.
17. Fan, Y.; Liu, P. F.; Huang, Z. Y.; Jiang, T. W.; Yao, K. L.; Han, R. *Journal of Power Sources* **2015**, *280*, 30–38.
18. Yang, X.; Zhang, Z.; Fu, Y.; Li, Q. *Nanoscale* **2015**, *7* (22), 10198–10203.
19. Wang, G. H.; Cao, Z.; Gu, D.; Pfänder, N.; Swertz, A. C.; Spliethoff, B.; Bongard, H. J.; Weidenthaler, C.; Schmidt, W.; Rinaldi, R.; Schüth, F. *Angewandte Chemie - International Edition* **2016**, *55* (31), 8850–8855.

20. Yuan, C.; Liu, X.; Jia, M.; Luo, Z.; Yao, J. *Journal of Materials Chemistry A* **2015**, *3* (7), 3409–3415.
21. Tetana, Z. N.; Mhlanga, S. D.; Coville, N. J. *Diamond and Related Materials* **2017**, *74*, 70–80.
22. Chen, A.; Li, Y.; Liu, L.; Yu, Y.; Xia, K.; Wang, Y.; Li, S. *Applied Surface Science* **2017**, *393*, 151–158.
23. Song, X.; Zhang, H.; Yang, Y.; Zhang, B.; Zuo, M.; Cao, X.; Sun, J.; Lin, C.; Li, X.; Jiang, Z. *Advanced Science* **2018**, *5* (7), 1–8.
24. Pendyala, V. R. R.; Jacobs, G.; Gnanamani, M. K.; Hu, Y.; Maclennan, A.; Davis, B. H. *Applied Catalysis A: General* **2015**, *495*, 45–53.
25. Pedersen, E. Ø.; Svenum, I. H.; Blekkan, E. A. *Journal of Catalysis* **2018**, *361*, 23–32.
26. Cook, K. M.; Perez, H. D.; Bartholomew, C. H.; Hecker, W. C. *Applied Catalysis A: General* **2014**, *482*, 275–286.
27. Eslava, J. L.; Sun, X.; Gascon, J.; Kapteijn, F.; Rodríguez-Ramos, I. *Catalysis Science and Technology* **2017**, *7* (5), 1235–1244.
28. Alayat, A.; Echeverria, E.; Mcllroy, D. N.; McDonald, A. G. *Fuel Processing Technology* **2018**, *177* (March), 89–100.
29. Nabaho, D.; Niemantsverdriet, J. W.; Claeys, M.; Steen, E. van. *Catalysis Today* **2016**, *275*, 27–34.
30. Aluha, J.; Abatzoglou, N. *Gold Bulletin* **2017**, *50* (2), 147–162.
31. Jermwongratanachai, T.; Jacobs, G.; Shafer, W. D.; Pendyala, V. R. R.; Ma, W.; Gnanamani, M. K.; Hopps, S.; Thomas, G. A.; Kitiyanan, B.; Khalid, S.; Davis, B. H. *Catalysis Today* **2014**, *228*, 15–21.
32. Den Otter, J. H.; Nijveld, S. R.; De Jong, K. P. *ACS Catalysis* **2016**, *6* (3), 1616–1623.
33. Zhang, R.; Liu, H.; Li, Q.; Wang, B.; Ling, L.; Li, D. *Applied Surface Science* **2018**, *453*, 309–319.
34. Martinelli, M.; Mehrbod, M.; Dawson, C.; Davis, B. H.; Lietti, L.; Cronauer, D. C.; Kropf, A. J.; Marshall, C. L.; Jacobs, G. *Applied Catalysis A: General* **2018**, *559* (March), 153–166.
35. Qian, L.; Cai, W.; Zhang, L.; Ye, L.; Li, J.; Tang, M.; Yue, B.; He, H. *Applied Catalysis B: Environmental* **2015**, *164*, 168–175.
36. Collins, S. S. E.; Cittadini, M.; Pecharromán, C.; Martucci, A.; Mulvaney, P. *ACS Nano* **2015**, *9* (8), 7846–7856.
37. Wang, L.; Yin, C.; Yang, R. T. *Applied Catalysis A: General* **2016**, *514*, 35–42.

38. Konda, S. K.; Chen, A. *Materials Today* **2016**, *19* (2), 100–108.
39. Karim, W.; Spreafico, C.; Kleibert, A.; Gobrecht, J.; Vandevondele, J.; Ekinci, Y.; Van Bokhoven, J. A. *Nature* **2017**, *541* (7635), 68–71.
40. Wu, Z.; Duan, Y.; Ge, S.; Yip, A. C. K.; Yang, F.; Li, Y.; Dou, T. *Catalysis Communications* **2017**, *91*, 10–15.
41. Shi, Q.; Zhang, R.; Lv, Y.; Deng, Y.; Elzatahrya, A. A.; Zhao, D. *Carbon* **2015**, *84* (1), 335–346.
42. Li, Z.; Liu, R.; Xu, Y.; Ma, X. *Applied Surface Science* **2015**, *347*, 643–650.
43. Zhuang, Z.; Giles, S. A.; Zheng, J.; Jenness, G. R.; Caratzoulas, S.; Vlachos, D. G.; Yan, Y. *Nature Communications* **2016**, *7*, 1–8.
44. Youn, D. H.; Patterson, N. A.; Park, H.; Heller, A.; Mullins, C. B. *ACS Applied Materials and Interfaces* **2016**, *8* (41), 27788–27794.
45. Ren, S.; Huang, F.; Zheng, J.; Chen, S.; Zhang, H. *International Journal of Hydrogen Energy* **2017**, *42* (8), 5105–5113.
46. Chen, X.; Deng, D.; Pan, X.; Hu, Y.; Bao, X. *Chemical Communications* **2015**, *51* (1), 217–220.
47. Yuan, Y. H.; Liu, Z. X.; Li, R. S.; Zou, H. Y.; Lin, M.; Liu, H.; Huang, C. Z. *Nanoscale* **2016**, *8* (12), 6770–6776.
48. Li, S.; Yao, N.; Zhao, F.; Li, X. *Catalysis Science and Technology* **2016**, *6* (7), 2188–2194.
49. Oschatz, M.; Hofmann, J. P.; van Deelen, T. W.; Lamme, W. S.; Krans, N. A.; Hensen, E. J. M.; de Jong, K. P. *ChemCatChem* **2017**, *9* (4), 620–628.
50. Park, H.; Kim, K. Y.; Youn, D. H.; Choi, Y. H.; Kim, W. Y.; Lee, J. S. *ChemCatChem* **2017**, *9* (21), 4098–4104.
51. Lee, W.; Kim, G. M.; Baik, S.; Lee, J. W. *Electrochimica Acta* **2016**, *210*, 743–753.
52. Wu, J.; Wang, L.; Lv, B.; Chen, J. *ACS Applied Materials and Interfaces* **2017**, *9* (16), 14319–14327.
53. Siang, T. J.; Bach, L. G.; Singh, S.; Truong, Q. D.; Ho, V. T. T.; Huy Phuc, N. H.; Alenazey, F.; Vo, D. V. N. *International Journal of Hydrogen Energy* **2018**, 1–12.
54. Kemache, N.; Hamoudi, S.; Arul, J.; Belkacemi, K. *Industrial and Engineering Chemistry Research* **2010**, *49* (3), 971–979.
55. Böttger-Hiller, F.; Mehner, A.; Anders, S.; Kroll, L.; Cox, G.; Simon, F.; Spange, S. *Chemical Communications* **2012**, *48* (85), 10568–10570.
56. Li, X.; Lau, S. P.; Tang, L.; Ji, R.; Yang, P. *Nanoscale* **2014**, *6* (10), 5323–5328.

57. Ayala, P.; Arenal, R.; Rümmeli, M.; Rubio, A.; Pichler, T. *Carbon* **2010**, *48* (3), 575–586.
58. Guo, D.; Shibuya, R.; Akiba, C.; Saji, S.; Kondo, T.; Nakamura, J. *Science* **2016**, *351* (6271), 361–365.
59. Ren, Y.; Lu, P.; Huang, X.; Ding, J.; Wang, H.; Zhou, S.; Chen, Y.; Liu, B. *RSC Advances* **2015**, *5* (69), 55994–56000.
60. Lee, W. H.; Lee, D. W.; Kim, H. *Journal of the Electrochemical Society* **2015**, *162* (7), F744–F749.
61. Salinas-Torres, D.; Léonard, A. F.; Stergiopoulos, V.; Busby, Y.; Pireaux, J. J.; Job, N. *Microporous and Mesoporous Materials* **2018**, *256*, 190–198.
62. Matsoso, B. J.; Ranganathan, K.; Mutuma, B. K.; Lerotholi, T.; Jones, G.; Coville, N. J. *Nanotechnology* **2017**, *28* (10), 105602.
63. Mutuma, B. K.; Rodrigues, R.; Ranganathan, K.; Matsoso, B.; Wamwangi, D.; Hümmelgen, I. A.; Coville, N. J. *Journal of Materials Chemistry A* **2017**, *5* (6), 2539–2549.
64. Chimowa, G.; Matsoso, B.; Coville, N. J.; Ray, S. S.; Flahaut, E.; Hungria, T.; Datas, L.; Mwakikunga, B. W. *Physica Status Solidi (A) Applications and Materials Science* **2017**, *214* (10), 1600930.

CHAPTER 2

Literature review

2.1. Introduction

Fischer-Tropsch synthesis (FTS) is a process whereby synthesis gas (a mixture of carbon monoxide and hydrogen) is catalytically activated to produce hydrocarbons.[1] This process occurs on the surface of a metal catalyst such as cobalt (Co), which has good activity and product selectivity.

Support materials have been found to effectively enhance the activity of Co nanoparticles during FTS reactions by enhancing the dispersion of the nanoparticles. These support materials include oxidic and carbon shaped supports.

Unfortunately the oxidic supports such as alumina; silica and titania, have been found to form strong metal to support interactions [1] during calcination, thus decreasing the reducibility or activation of the Co oxide precursors. The shaped carbon materials such as solid carbon spheres (CSs), carbon nanotubes (CTNs) and hollow carbon spheres (HCSs) have been shown in literature to be good alternative support materials that do not form strong bonds with the catalyst. This arises from the physiochemical properties of the carbon which includes chemical inertness; high surface area; high electronic conductivity; and tuneable surface functionality. These properties broaden the application possibilities when using the carbon supports.

The surface properties of HCS support materials can be easily tailored by the incorporation of heteroatoms, i.e nitrogen, boron or sulphur, within the carbon matrix. This process is known as chemical doping. Chemical doping using nitrogen as the heteroatom (N-doping) has the advantage of ease of incorporation arising from the comparable sizes of the carbon and nitrogen atoms. Incorporation of nitrogen atoms within a carbon matrix can take one of a range of nitrogen bonding configurations which include pyridinic, pyrrolic, quaternary and oxidised nitrogen. [2, 3] These configurations are shown in figure 2.1. The continuous interest in the use of N-doped carbons as support materials for metal catalysts has been attributed to

their ability to enhance the electronic conductivity of the carbon support as well as to enhance the stability and activity of metal nanoparticles during FTS reactions.

Alternatively, the activity of the metal nanoparticles can be enhanced by electronic promotion, by the addition, in low content, of noble metals such Ru. The electronic promotion is facilitated so as to improve the reduction of the metal catalyst precursor (Co oxide). The noble metals have a high affinity for hydrogen dissociation which is necessary for the reduction of the Co oxide. Briefly, noble metals dissociatively adsorb the hydrogen atoms which then migrate by diffusion towards a catalyst precursor. This process is known as hydrogen spillover [2] and is represented in figure 2.1.

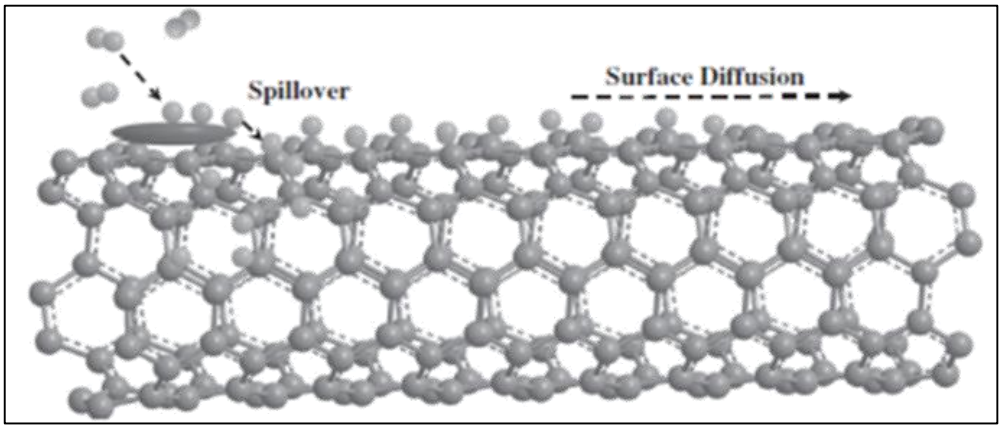


Figure 2.1 The hydrogen spill over process on a carbon support.[2, 3.]

Herein, we review the research developments in modifying HCSs, through doping, for the use as catalyst supports for the hydrogen spillover process. Our main focus will be on N-doping of HCSs as a means of improving hydrogen spillover and FTS catalytic activity.

2.2. Fischer-Tropsch synthesis

2.2.1. Background

As the demand for energy increases, environmental concerns are also on the rise. One major environmental concern is global warming that arises from the emission of greenhouse gases as by-products during technological processes. Researchers, particularly engineers and scientists have been tasked to find ways to lower industrial related contributions towards global warming. Catalytic processes and selective catalysts can be used to reduce the production of harmful by-products.

A commercial technological process used for energy production is Fischer-tropsch synthesis (FTS). [4] The FTS process is an exothermic reaction that is conducted at high pressure and is described as:-

$$CO + 2H_2 \rightarrow CH_x + H_2O \qquad \Delta H°_{298K} = -165\ kJ/mol$$

By definition FTS is the catalytic hydrogenation of carbon monoxide (CO) by hydrogen (H_2) to form hydrocarbons that are necessary for the production of energy, fuels and chemicals. The synthesis gas can be derived from feedstocks such as biomass, oil, natural gas and coal.

The commercial FTS process is mainly composed of three main reaction steps, namely: (i) production and purification of synthesis gas, (ii) FTS: hydrogenation of CO over a metal catalyst and (iii) product upgrading, as shown below in figure 2.2. The production of clean synthesis gas is facilitated through steam/CO_2 reforming and partial oxidation processes. During this step, the removal of ash, tar, as well as sulphur, hydrogen and nitrogen containing compounds is also facilitated. Subsequently, reactors which have been conditioned to maintain even distribution of heat and separation of products containing Co/Fe metal catalysts are employed to facilitate the FTS process. Lastly the products, obtained during FTS, such as waxes and liquids are upgraded to gasoline and diesel products, through isomerisation and hydrocracking, respectively.

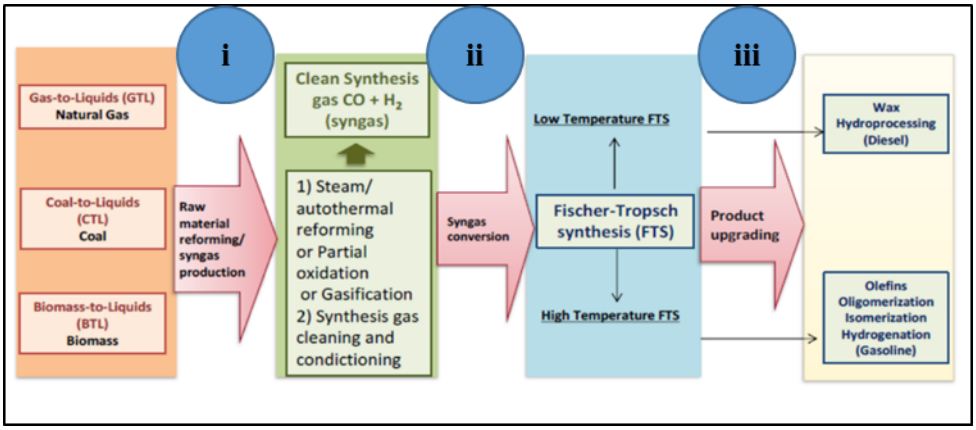


Figure 2.2 The schematic representation of the FTS process from feedstocks to products.[4]

Historically, CO hydrogenation was first documented by Sabatier and Senderens in 1902. [5] The German researchers managed to synthesize the methane hydrocarbon. Two decades later, Fischer and Tropsch produced "Synthol", a mixture of oxygen-containing derivatives of hydrocarbons. The synthol was catalytically obtained using an alkali treated Fe catalyst. [6] In 1925 Fischer and Tropsch successfully improved the selectivity of the reaction to yield predominantly hydrocarbons when they used Fe/ZnO or Co/Cr_2O_3 as catalysts at temperatures of 250 °C – 300 °C and at a standard pressure. In 1936, Fischer and Pichler observed that using pressures between 5 - 30 atm and a Co or Fe catalyst that the product yield and lifespan of the catalyst could be improved. [6-8] A further increase in temperature and pressure was found to give a high selectivity to long hydrocarbons. Hence from these reports it is clear that product selectivity of a FTS process is dependent on temperature, pressure and catalysts employed. [7]

During FTS, various carbon length chains are produced with primary products being paraffins, olefins, branched hydrocarbons and some oxygenates. The main reactions that take place during FTS are shown in equation 2.1 to 2.3 where *n* is the carbon number.

Paraffin formation:

$$nCO + (2n + 1)H_2 \rightarrow C_nH_{2n+2} + nH_2O \quad \ldots\ldots\ldots\ldots\ldots 2.1$$

Olefin formation:

$$nCO + 2nH_2 \rightarrow CnH_{2n} + nH_2O \quad \ldots\ldots\ldots\ldots\ldots\ldots\ldots\ldots\ldots 2.2$$

Water-gas shift (WGS) reaction:

$$CO + H_2O \leftrightarrow CO_2 + H_2 \quad \ldots\ldots\ldots\ldots\ldots\ldots\ldots\ldots\ldots\ldots 2.3$$

The formation of paraffins and olefins is represented by equations 2.1 and 2.2 respectively. In addition to the product selectivity factors reported above, the H_2:CO ratio and H_2O concentration have also been reported to have an effect on selectivity of products. [6-8] The paraffins have been reported to form as a results of the greater hydrogenating abilities of catalysts in the presence of high H_2:CO ratios, whereas the inverse is reported for the formation of olefins. The WGS reaction is a side reactions that occurs when the FTS product H_2O reacts with the reactant CO to give H_2 and the CO_2. [6-8]

The FTS process may be operated in generally one of the two operating regimes based on temperature, namely: low temperature FTS (LTFT) and high temperature FTS (HTFT), with opeating regimes as shown in table 2.1. [9] The LTFT regime is operated at temperatures between 220 ^oC and 240 ^oC, using cobalt catalyst in a multitubular fixed bed reactor and has high selectivy to praffins. In constrast, the HTFT regime is operated at higher temperatures, between 320 ^oC and 350 ^oC , on a Fe catalsyt in a fixed bed fluidised reactor and has greater selectivity towards oxygenated products.[9, 10]

Table 2.1 FTS reaction conditions and product selectivity. [9, 10]

Parameter	LTFT	HTFT
Catalyst	Cobalt (Co) Iron (Fe)	Iron (Fe)
Temperature	220 ^oC – 240 ^oC	320 ^oC – 350 ^oC
Reactor	Multitubular fixed bed	Fixed fluidised bed
Products/Selectivity	Paraffins Wax diesel: alkanes : alkenes	Gasoline: oxygenates : hydrocarbons

2.2.2. Cobalt FTS catalysts

The optimization of the FTS process is attainable through careful design and tuning of the catalyst, to give better CO conversions and selectivity. The factors that influence the resulting activity and selective are the preparation method, particle size of the metal catalyst, nature of the catalyst support and calcination temperature used. [11]

The transition metals of group 8 to group 10 show some activity during FTS reactions, [12] but only Fe and Co are used at an industrial scale because they are relatively easy to prepare, cheap and have good stability; selectivity and activity. Although the cost of a Co catalyst is much higher than that of a Fe catalysts, a Co catalyst has the advantage of product selectivity towards higher alkanes (C_{5+} hydrocarbons), a low hydrogenation capacity, longer lifetime [13] and shows a lesser affinity towards the water gas shift reaction. [14]

The Co catalyst, in the metallic state, exists in two crystalline forms, the face centred cubic (fcc) structure and hexagonal close packed (hcp) structure. The formation of these phases is dependent upon the kinetics of the chemical reaction and thermodynamics. [15] During FTS reactions, the hcp phase has been found to show higher CO conversions and selective towards C_{5+} hydrocarbons. [16] This is attributed to the presences of more defects found on the surface of the hcp phase.

Supported Co catalysts have also been reported to have a catalytic activity that is dependent on the nature and interaction between the support material and the Co nanoparticles that are more pronounced at elevated temperature used to calcine catalysts.[16, 17] An extensive study by Das and Deo reported a decrease in the catalytic activity of supported Co catalysts due to high support-metal interactions. The decrease in the catalytic activity was attributed to the unavailability of the metal-support interface. [18]

A promising approach to supporting Co nanoparticles is the use of carbon materials. Xiong and co-workers reported on the advantage of using carbon based supports, CNTs and CSs. They reported that in addition to lower support-metal interactions, the carbon supports also facilitated Co_xO_y auto-reduction at 480 °C, had good metal dispersion and a high catalytic activity to C_{5+} hydrocarbons selectivity. [19]

2.2.3. Hollow carbon spheres: nanoreactors as support for FTS

Carbon nanomaterials, are without a doubt, a promising material being used in nanotechnology studies. It has been over 3000 years since the first use and synthesis of carbon allotropes [20], where carbon black was applied as an ink. Since then, further discoveries of carbon shaped materials such as fullerene[21], graphene [22,23] and carbon nanotubes[24-26] have broadened the application possibilities of carbon materials[27-30]. Various carbon shaped materials, within the nano-size range, have since been introduced. This includes, carbon onions[31], carbon dots[32] and hollow carbon spheres[33] (HCSs). Various carbon allotropes of carbon are shown in figure 2.3. The properties of these carbon nanomaterials are usually optimized to best suit applications such as when they are used as heterogeneous catalyst supports, fuel cell electrodes and hydrogen storage materials. [34-36]

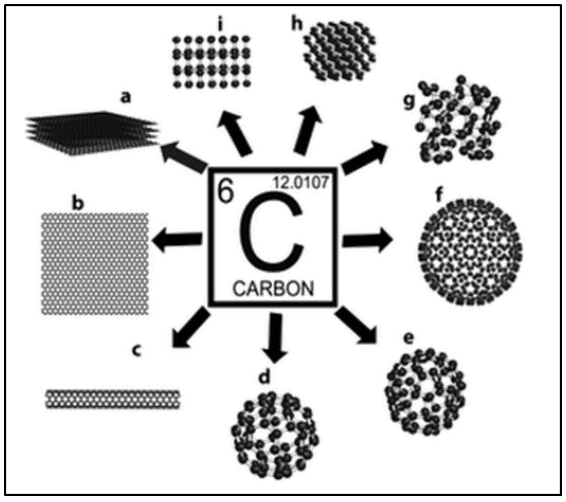


Figure 2.3 Various allotropes of carbon that are used as supports; graphite (a), graphene (b), carbon nanotube (c), fullerene (d), C_{70} (e) , hollow carbon spheres (f), amorphous carbon (g), lonsdaleite (h), diamond (i). [37]

Among the above mentioned carbon shaped materials, HCSs[38-42] have been applied as nanoreactors in heterogeneous catalysis such as FTS. [29, 30] The HCSs are made of spherical layers of graphitic carbon with a hollow core. They have gained momentum due to their tuneable physiochemical properties. These include chemical inertness, large surface area (2 m^2/g-1200 m^2/g), porous (2 nm-20 nm), diameter (50 nm-1000 nm), shell thickness and surface functionalization. [34]

Studies have shown that the use of nanoreactors in catalytic processes such as FTS, aims to limit the sintering of catalytic nanoparticles by encapsulating the nanoparticle [43-45] within the hollow core and to tune the selectivity through mass transfer of reactants (synthesis gas) into the hollow core and products (hydrocarbons) out of the hollow core, which is facilitated through the pores as depicted in figure 2.4. A study by Liu and co-workers showed that the use of the Au@C catalyst gave high conversions (~ 99 %) with time on line while preventing catalyst deactivation due to Au particles being encapsulated. [46] Phaahlamohlaka and co-workers synthesized two FTS catalyst of varying porosity, Ru@HCS and Ru@mesoporous-HCS. These catalysts had metal particles size of 5.5 nm and 3.2 nm respectively. The pore size of the catalysts were reported to be 2 nm for the Ru@HCS catalyst and 8 nm for the Ru@mesoporous-HCS catalyst. Both catalysts showed good FTS activity without diffusion limitations and low particle sintering but had a high methane selectivity. The selectivity towards methane was attributed to the small Ru nanoparticles. [47]

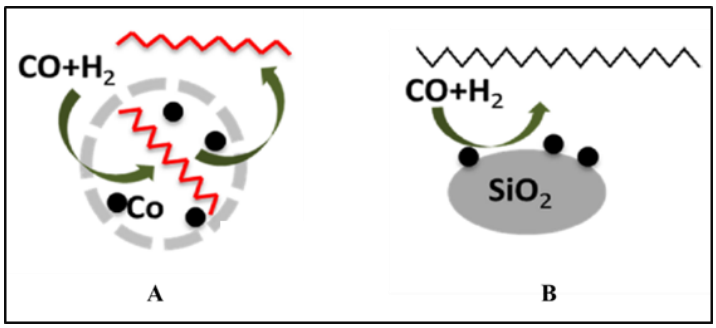


Figure 2.4 A FTS reaction occurring in a nanoreactor (A) and on a conventional oxidic support (B). [43]

2.2.4. Synthesis methods used to make HCSs

Nanoreactors are new generation support materials in catalysis. Particularly in heterogeneous catalysis, they offer good stability for the active phase within a hollow space and also provide selective diffusion in and out of a hollow cavity, as described above. Nanoreactors include zeolites, carbon nanotubes and HCSs. For the purpose of this section, we will only discuss HCSs.

The synthesis routes to make HCSs usually involves templating methods. [48] The synthesis routes and techniques used during synthesis of HCSs is dependent on the type of template and the carbon source that is employed during synthesis. Common templates are silica and

polystyrene. The templating technique is comprised of at least three main steps, namely (i) the synthesis of the template, (ii) the shell formation of the desired material on the template surface i.e. coating of a carbon shell around the template through polymerization, pyrolysis; chemical vapour deposition (CVD); hydrothermal carbonizatoion (HTC) and (iii) the template removal through decomposition. This is shown in figure 2.5.

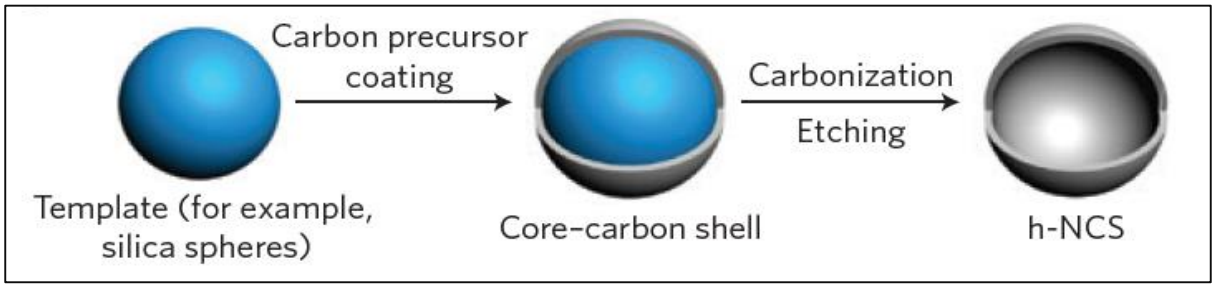


Figure 2.5 Schematic representation of the synthesis of HCSs by hard templating. [49, 50]

Templating methods can be categorised into two types, the hard-templating and soft-templating types, as summarized in Table 2.2. The soft templating method has been found interesting due to the ease of template removal. Emulsion droplets, micelles or vesicles arising from carbonaceous precursors are used as soft templates in an in situ process to form the HCSs. The precursor molecules self-assemble or are linked together followed by carbonization under mild heat treatment to form HCSs. Limitations of the templating technique are the inability to control product morphology and mono-dispersity of the HCSs. [20] To overcome these limitations most researcher have focused on using the hard templating method.

Hard templating processes make use of hard sacrificial templates that are chemically dissolved or thermally decomposed after a spherical carbon shell has been formed around them. Spherical silica, polystyrene and metals are some of the hard templates that have been used [20] which have the advantage of allowing for controlled morphology through the use of the sacrificial template. The characteristics of these solid templates are very important because the resulting HCSs are their replicas hence maintaining the morphology and diameters of the template. Other properties of HCSs such as porosity, and shell thickness may be tuned during synthesis by the addition of surfactants and varying the amount of the carbon precursor. For example, Chen and co-workers used silica spheres as a template and gaseous acetylene as the carbon precursor to synthesize HCSs through the CVD technique. Highly graphitic HCSs were obtained and these had a large surface area of 771 m^2/ g. [51, 52] Yang et

al. synthesized HCSs with different shell thickness, using a silica template and by varying the amount of the carbon precursor resorcinol-formaldehyde. When the concentration of resorcinol-formaldehyde was increased from $1.36x10^{-3}$ mol/L to $2.05x10^{-3}$ mol/L, the shell thickness was increased 180 nm to 360 nm. [53] In another study Chen et al. reported on the use of a silica template, acetylene carbon precursor and octadecyltrimethoxysilane as a surfactant to synthesize mesoporous-HCSs. They obtained high surface area mesoporous-HCSs (948 m^2/g) with a shell thickness of 90 nm, pore size of 1.4 nm and a pore volume of 0.3824 cm^3/g after etching out the silica template, using hydrofluoric acid. [54] The polystyrene template is an attractive template in material science. The advantage of using the polystyrene template is because it is easily decomposed when used as a carbon template. Han and co-workers used spherical polystyrene as the templates and aniline as the solid carbon precursor. The aniline was polymerised and annealed to obtain HCSs with a surface area of 213 m^2/g. [30] Lee and co-workers synthesized microporous-HCSs with ultrahigh surface area of 1724 m^2/g by using polystyrene spheres as a template and coordination polymer zeolitic imidazolate frameworks (ZIF-8) as the carbon source. [55]

Table 2.2 Synthesis technique and conditions for nanoreactors. [20]

Strategy	Technique	Synthesis conditions	Carbon source
Hard-templating	CVD (a) HTC (b) pryrolysis	>600 ^oC 150 ^oC >800 ^oC	Gaseous Polymer, biomass Polymer, biomass
Soft-templating	Emulsion Surfactant HTC (b)	Mild Mild Mild (150 ^oC – 200 ^oC)	Carbonaceous polymers Carbonaceous polymers Polymer, biomass

(a) Chemical vapour deposition; (b) hydrothermal carbonization (HTC)

Metal nanoparticles have a catalytic effect on the growth of HCSs as has been reported in some publications.[33, 56] However, these metals can also be used as solid templates. Bai et al. used Zn metal as a template and acetylacetone as the carbon precursor to synthesize HCSs. The carbon shell around the Zn metal was formed using the HTC method and Zn metal was

removed by washing with dilute HCl. [57] The templating abilities of Fe, Mo and Al metals have also been explored. [58-60]

2.2.5. Structural modification of HCSs: nitrogen doping

The properties of HCSs such as electrical conductivity, inertness and hydrophobicity can be tailored through chemical modification such as oxidative treatment [61-63] and doping [64, 65]. Doping allows for chemical modification to occur through the introduction of heteroatoms (dopant) into the carbon matrix. The most studied dopant is nitrogen [26, 66, 67] due to its high abundance and its ease of incorporation into the carbon matrix as it has a comparable size to the carbon atom. The synthesis of nitrogen containing carbon materials is similar to that of pristine carbon materials (as detailed in the section above). The different configurations of nitrogen dopant that can be incorporated into carbon matrix during nitrogen doping are the pyridinic N, pyrrolic N, oxidied N and quaternary N types. [68] These N-configurations are shown on figure 2.6. Compounds that are rich in nitrogen such as ammonia, acetonitrile, pyrrole and melamine are used as nitrogen precursors during the doping of carbon. [69-71] It is also noteworthy that N-atoms possess an additional electron which provides nucleation sites on the support.

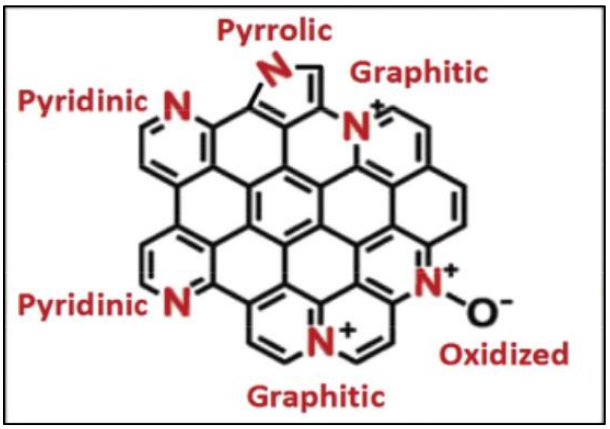


Figure 2.6 Nitrogen configurations incorporated into the carbon matrix. [23]

N-atoms may be incorporated into the carbon matrix in one of two ways, which is by in-situ doping or post doping. In in-situ doping, the N-atoms are incorporated during the synthesis of the carbon shell. In contrast, post nitrogen doping is when the N-atom replaces some of the carbon atoms within the carbon matrix after the carbon matrix has formed or by adding an N-

doped layer to the original carbon matrix. Table 2.3 gives a summary of doped carbon materials with the corresponding nitrogen content.

Table 2.3 Nitrogen doping methods, precursors and nitrogen content on carbon materials.

Nitrogen precursor	Synthesis technique	Type of doping	Nitrogen content (wt %)	Reference
Melamine and formaldehyde	Polymerization and pyrolysis	In situ doping	~8 %	72
Melamine	Pyrolysis	Post doping	0.2 % - 21 %	73
Pyrrole	HTC and pyrolysis	In situ doping	~9 %	74
acetonitrile	CVD	In situ doping	~9 %	28, 84
Dopamine	Pyrolysis	In situ doping	~6 %	75

The incorporation of the N-types within the carbon matrix has been found to influence the properties of a carbon support and of a metal catalyst supported on the carbon. These include; (i) provision of nucleation and growth sites by C-N defective site for metal particles [76, 77], (ii) enhanced interaction between support and catalyst particles due to hybridization between the π orbitals of nitrogen and the d orbitals of the transition metal [78], (iii) the N-site can act as a ligand and thus form a complex with a metal particle [79] and (iv) enhanced carbon basicity that leads to better dispersion in solvents through charge transfer. [80]

Catalysis research has shown that improvement of the activity of catalysts can be achieved when the catalyst is supported on nitrogen-doped carbons during FTS. [81-83] The nitrogen doping enhances the metal dispersion, provides anchoring sites to a metal catalyst, facilitates auto-reduction of metal particles and provides donor sites thus limiting the sintering effects during calcination reactions. A study by Xiong and co-workers [84] revealed that the use of a nitrogen doped carbon support facilitated the auto-reduction of supported cobalt oxide nanoparticle to small catalytically active metallic Co particles for FTS. This effect was later attributed to the nitrogen content by Yang and co-workers [85]. In another study [86], higher CO conversion was attributed to electron transfer by pyrrolic-N towards Co^{2+} atoms. Nitrogen promotion effects were studied by Lu et al. on Fe/N-CNTs catalyst. Their CO TPD studies showed that nitrogen atoms introduced some basicity which enhanced CO chemisorption. In

addition, nitrogen atoms donated lone pair electrons to empty 3d orbital of the Fe metal thus enhancing the bond strength of Fe-C allowing for ease of CO dissociation. [87] Additionally, Chew et al [88] studied and compared oxygen and nitrogen functional groups and their effect on the dispersion of a Fe catalyst on supports. Nitrogen groups were stable and were not removed during annealing at high temperatures and a high activity and less sintering of Fe particles on the supports was noted. This was also attributed to the retention of the more stable oxygen groups on the carbon support after annealing. Yang et al. [89] and Xiong et al. [64] also assessed the FTS efficiency using N-doped mesoporous carbon as a support for catalyst nanoparticles. A high methane selectivity was obtained due to the small particle sizes of the metals. A high dispersion of small nanoparticles was obtained and correlated to the sp^2 regions on the support, providing nucleation sites for catalyst particles.

2.3. Hydrogen spillover: promotion effects on Co Fischer-Tropsch catalysts

2.3.1. Overview of hydrogen spillover

Hydrogen spillover is the surface diffusion of hydrogen ions from a dissociating surface to another that is not dissociating under the same reaction conditions. [90] Systematically, the hydrogen spillover process is composed of (i) the hydrogen activating species which is typically a noble metals e. g. Pt, (ii) a support material that facilitates surface diffusion and (iii) accepting species, the metal oxide to be activated by the reduction reaction.[91]

There are two types of hydrogen spillover processes that have been reported. These are the primary and secondary hydrogen spillover processes [92], as shown in figure 2.7. The two processes are dependent on the type of contact between the activating and the accepting species. In primary spillover there is a direct contact between the initiating species and the accepting species. On the other hand, secondary spillover occurs when the initiating species and the accepting species have an indirect contact, thus the spilled over hydrogen has to migrate/diffuse via the support. [93, 94]

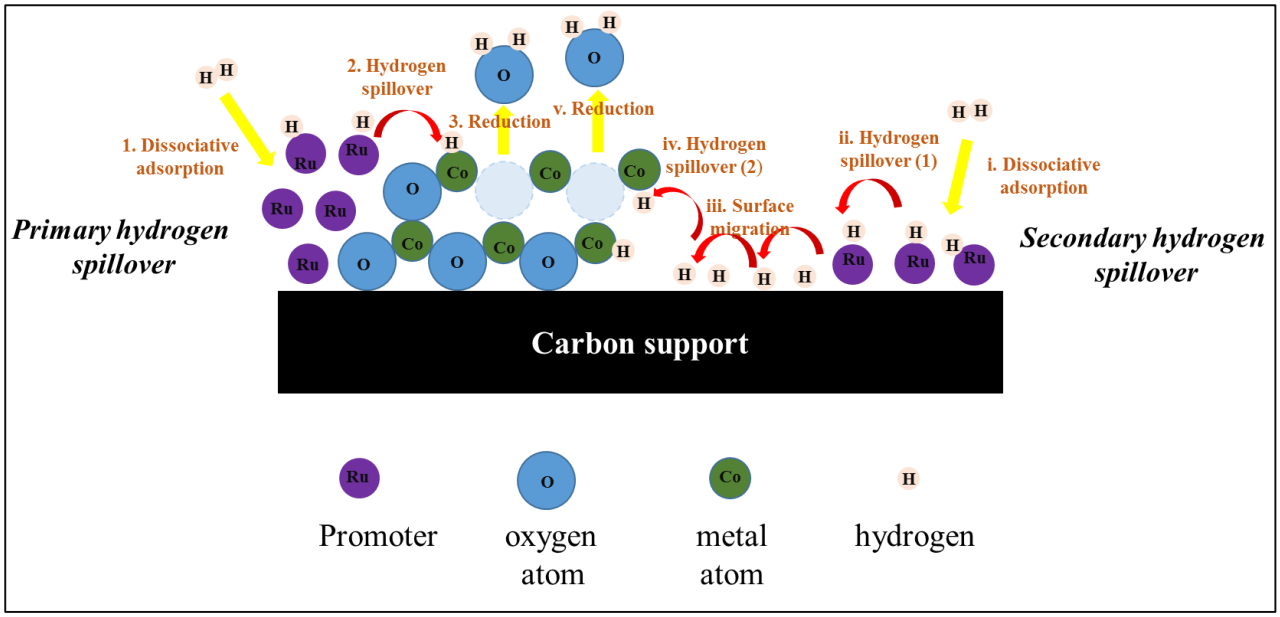


Figure 2.7 Diagrammatic presentation of the hydrogen spillover process, detailing primary and secondary spillover. [92]

The concept of hydrogen spillover process was first experimentally presented by Khoobiar in 1964 [95] when he attributed the resultant blue colour of WO_{3-x} to its reduction by H_2 which dissociatively chemisorbed on the surface of the nearby Pt metal. Years later, the process was defined as hydrogen spillover and the reduction was to be said to be facilitated by electrons and protons. Briefly, the dissociated hydrogen from the surface of the Pt metal diffused to the WO_3 where the H_2 lost its electrons and generated H^+ ions. The protons moved quickly through the WO_3 lattice via hydrogen bonding and the electrons reduced the W^{+6} to W^{+5} and moved through the lattice via W^{+6}-W^{+5} exchange, as shown in figure 2.8. [95, 96] Density functional theory (DFT) calculations confirmed the mobility to be that of proton and electrons, not hydrogen atoms. [97]

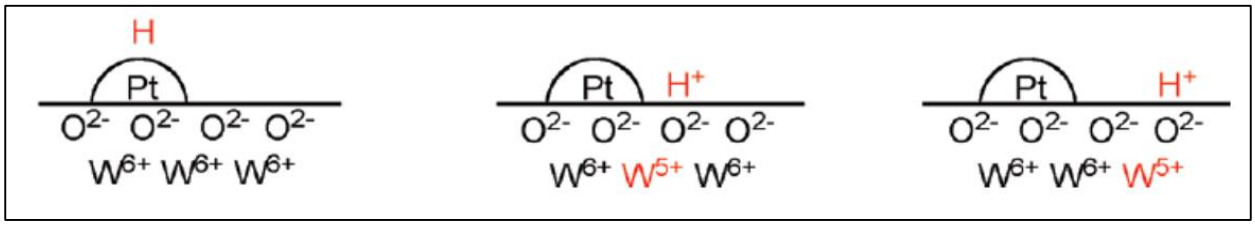


Figure 2.8 Schematic diagram of the production of the proton and electron upon adsorption of H_2 on Pt and subsequent spillover of H atoms to the reducible WO_3 support. [95, 96]

Non-reducible oxidic supports such as silica and alumina, have also been observed to facilitate hydrogen spillover by hydrogen atoms from a metal surface, although the process is energetically unlikely unless there are defects present. [95, 96]

2.3.2. Promotion of supported Co catalysts: Co-Ru systems for hydrogen spillover

Low temperature FTS Co catalysts require activation in a H_2 environment and hence are introduced into the reactor as the precursor, Co_3O_4, which is then reduced to the active metal state, Co^o. The complete reduction of Co_3O_4 is important for improved FTS activity because of the higher number of active sites available on the reduced Co metal. The activation step is facilitated through a reduction process typically by hydrogen molecules. [92] The activation of cobalt oxide occurs in two steps:-

$$(i)\ Co_3O_4 + H_2 \rightarrow 3CoO + H_2O$$

$$(ii)\ 3CoO + 3H_2 \rightarrow 3Co + 3H_2O$$

The activity and reducibility of supported Co_3O_4 nanoparticles has been reported to be dependent on factors such as particle size, calcination conditions and the nature of the support. [98, 98] For example, small crystallite sized particles have a stronger interaction with an oxidic alumina support. Thus after catalyst calcination, formation of a cobalt-aluminate compound results. The cobalt-aluminate compound has limited reducibility. In a report by Jung et al. it was shown that different thermal treatment environments have an effect on the resulting Co phase and subsequently on the FTS activity. The researchers prepared 15% Co-Ru catalysts supported on alumina. The catalysts was subjected to thermal treatment in air and/or in H_2 at 400 °C for 4 hours. The reducibility of the catalysts was then studied under a flow of 5% H_2 in Ar (40 ml/min). It was found that more hcp metallic Co phase resulted when a catalyst was thermally treated in a H_2 environment whereas more of the fcc metallic Co phase was produced when catalyst was thermally treated in air. As expected the catalyst treated in H_2 (Co hcp; more defective sites) had a higher FTS activity. [100]

One way to enhance the reducibility of Co_3O_4 is by the addition of small amounts of noble metals. This process is known as promotion. [101] These noble metals are known as electronic promoters. Common electronic promoters for a Co catalyst include, Ru, Pt, Re and Pd. [92, 101]

Promoters have a high hydrogen dissociating activity in a reducing environment. The promotion effect occurs by hydrogen spillover. The hydrogen spillover phenomena was described in the previous section. The advantage of a promoter metal is that it allows for optimization of catalyst performance by (i) promoting hydrogen spillover, thus facilitating effective reduction of the metal oxide, (ii) preventing coke accumulation and (iii) coordinating with cobalt species to induce electronic effects and (iv) enhancing the metal dispersion by providing nucleation sites. [92]

Supported Co catalysts promoted with noble metals displayed the following order of FT catalytic activity: CoRu > CoPd > CoPt > CoRe. [13] The choice of ruthenium as a promoter is due to its cost (as shown in figure 2.9); it is cheaper than platinum, and has a great affinity for hydrogen dissociation. [102]

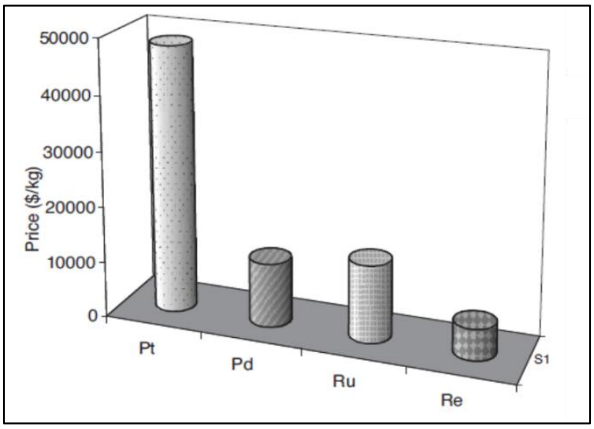


Figure 2.9 Cost of various electronic promoters. [109]

The study on the effect of using 0.2 wt. % of Pt and Ru as promoters for CNT supported catalysts was done by Zhang et al. The study revealed that the presence of the promoter improved Co reducibility and C_{5+} product selectivity. [103] Ru as a promoter has also been found to have improved the dispersion of Co nanoparticles supported on low surface area supports, as reported by Hong et al. [104]

Promotion may also lead to the formation of bimetallic (Co-Ru) cobalt-noble metal particles during oxidative calcination treatments at 300 ^{o}C. Promotion also leads to synergy between the catalytic metal and the promoter by influencing the electronic properties of the catalytic metal and thus enhancing FTS activity. Additionally, the bimetallic system promotes charge polarization and may lower the binding energy of the reactants. [102, 105]

2.3.3. Efficiency of hydrogen spillover on carbon supports: effect of defects and distance

Hydrogen spillover, as mentioned above, is a fundamental phenomenon in the heterogeneous catalysis field. Catalyst supports play in important role in spillover and these can be various metal oxides or differently shaped carbons. [106] The main role of the support to provide a path for hydrogen atoms to move form an activating metal surface to an accepting metal surface, through diffusion. [3, 106] An example of spillover over a carbon nanotube is shown in figure 2.10.

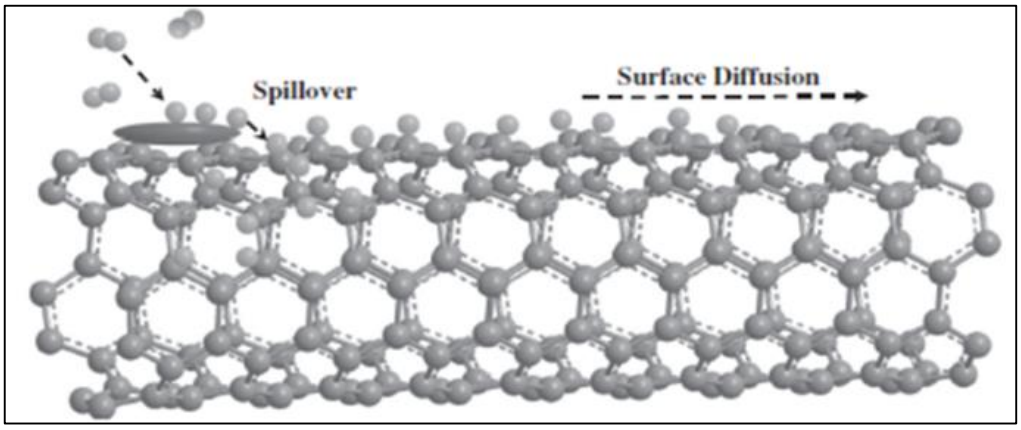


Figure 2.10 Hydrogen spillover on carbon supports through surface diffusion.[3]

Effective hydrogen spillover has been reported for short distances [2, 107]. This is linked and more pronounced in non-reducible supports, [2] For example, when an iron oxide catalyst supported on alumina, and its promoter and iron oxide are overlapping, effective hydrogen spillover is observed. However, when the metal oxide and promoter are apart and at a distance of 15 nm or greater minimum hydrogen spillover is measured (see figure 2.11). In a study by Nabaho and co-workers [92] Au was studied as a potential promoter, in comparison to the known Pt promoter. When a cobalt catalyst was supported on alumina, hydrogen spillover was more pronounced when the Co precursor and Au promoter were in close proximity. This was attributed to Au having lower hydrogen dissociation energy then the cobalt oxide. It was noted that in the presences of the promoters, Au or Pt, the reducibility of CoO species did not improved when compared to the reducibility of the Co3O4 species. This was due the alumina support, which stabilizes the divalent CoO species and hence decreasing the reducibility.

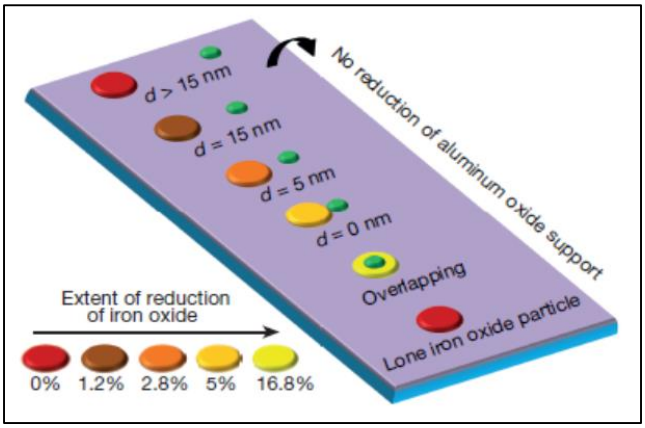


Figure 2.11 Presentation of the degree of reduction on a non-non-reducible support.[2]

In carbon materials it has been proposed that the carbon surface area is important. In one study, Wang and Yang analysed various carbon-based materials as hydrogen storage adsorbents. They reported that the storage mechanism occurred via hydrogen spillover and that the surface area of the carbon support was one of the main contributing factors to the spillover process. [3]

For most metals the binding energy of the metal-hydrogen bond is approximately 250 kJ/mol. Thus for hydrogen spillover to be thermodynamically feasible bond formation with similar energy should occur when support-H bonds are formed. [94, 108, 109] In carbon based supports, hydrogen spillover has been reported to be facilitated through the formation of C-H and O-H bonds. [110, 111] In an early study by Chen et al., spillover of hydrogen was found to be slow on the surface of CNTs and graphene. [111] Therefore it can be proposed that graphitic carbons may not be able to facilitate appreciable hydrogen spillover, unless some defects are present within the carbon matrix. These defects may be incorporated through metal doping and heteroatom doping. Pyle et al. reported that hydrogen spillover can be improved through metal doping of a pristine carbon support. They correlated this to the presence of defects and surface oxygen groups which were able to break the π-conjugation and create highly reactive sites which provided nucleation sites for hydrogen clustering. [112]

The effect of intimacy between the Ru promoter and Co_3O_4 supported on mesoporous carbon in the shape of a hollow carbon sphere (MHCS) was studied by Phaahlamohlaka [42] and co-workers. An unpromoted catalyst, Co/MHCS, was used as a standard catalyst in H_2 reduction studies using TPR analysis. The reduction study of the catalyst revealed hydrogen consumption peaks at the temperature of 282 °C and 429 °C in the TPR profile. A direct contact system of Co-Ru/MHCS catalyst showed enhanced Co_3O_4 reduction through a

primary hydrogen spillover process, due to the synergistic effect between the promoter and metal oxide. In contrast to this observation of direct contact system, the indirect contact system of the Ru@MHCS@Co catalyst showed less impact of Ru on the Co. In the system the Co and the Ru metal are separated by the MHCS support and so a primary spillover effect was not possible and hence secondary hydrogen spillover was showed. However promotion of CoO reduction by Ru was also observed to promote CoO →Co reduction.

2.4. Concluding remarks

The use of Co catalysts on carbon supports in heterogeneous catalysis, as well as other fields, has grown significantly throughout the years. The promotion effects of carbon supports resulting from incorporation of support defects and electronic factors show great potential as methods to improve hydrogen spillover.

2.5. References

1. Cornils, B.; Herrmann, W. A.; Schlogl, R.; Wong, C. H. *Catalysis from A to Z: concise encyclopedi*a, *Platinum metals review* **2000**, 167.
2. Karim, W.; Spreafico, C.; Kleibert, A.; Gobrecht, J.; Vandevondele, J.; Ekinci, Y.; Van Bokhoven, J. A. *Nature* **2017**, *541* (7635), 68–71.
3. Wang, L.; Yang, R. T. *Catalysis Reviews - Science and Engineering* **2010**, *52* (4), 411–461.
4. Pardo-tarifa, F. *Cobalt catalyst supports for Fischer-Tropsch synthesi*s **2017**, KTH Royal institute of technology, Sweden.
5. Sabatier, P.; Senderens, J. B. *C. R. Acad. Sci. Paris* **1902**, *134*.
6. Casci, J. L.; Lok, C. M.; Shannon, M. D. *Catalysis Today* **2009**, *145* (1–2), 38–44.
7. Henrici-Olivé, G.; Olivé, S. *Journal of Molecular Catalysis* **1978**, *3* (6), 443–446.
8. Henrici-Olivé, G.; Olivé, S. *Angewandte Chemie International Edition in English* **1976**, *15* (3), 136–141.
9. De Klerk, A. *Green Chemistry* **2008**, *10* (12), 1249–1279.
10. You, S.; Ok, Y. S.; Tsang, D. C. W.; Kwon, E. E.; Wang, H.; You, S.; Ok, Y. S.; Tsang, D. C. W.; Kwon, E. E.; Wang, C. *Critical Reviews in Environmental Science and Technology* **2017**, *0* (0), 1–48.

11. Bezemer, G. L.; Radstake, P. B.; Koot, V.; Van Dillen, A. J.; Geus, J. W.; De Jong, K. P. *Journal of Catalysis* **2006**, *237* (2), 291–302.
12. Vannice, M. A. *Journal of Catalysis* **1977**, *37* (2), 449–461.
13. Khodakov, A. Y.; Chu, W.; Fongarland, P. *Chemical Reviews* **2007**, *107* (5), 1692–1744.
14. Fu, T.; Li, Z. *Chemical Engineering Science* **2015**, *135*, 3–20.
15. Kalyan Kamal, S. S.; Sahoo, P. K.; Premkumar, M.; Rama Rao, N. V.; Jagadeesh Kumar, T.; Sreedhar, B.; Singh, A. K.; Ram, S.; Chandra Sekhar, K. *Journal of Alloys and Compounds* **2009**, *474* (1–2), 214–218.
16. Gnanamani, M. K.; Jacobs, G.; Shafer, W. D.; Davis, B. H. *Catalysis Today* **2013**, *215*, 13–17.
17. Das, T.; Deo, G. *Journal of Molecular Catalysis A: Chemical* **2011**, *350* (1–2), 75–82.
18. Das, T.; Deo, G. *Catalysis Today* **2012**, *198* (1), 116–124.
19. Xiong, H.; Motchelaho, M. A. M.; Moyo, M.; Jewell, L. L.; Coville, N. J. *Journal of Catalysis* **2011**, *278* (1), 26–40.
20. Li, S.; Pasc, A.; Fierro, V.; Celzard, A. *Journal of Materials Chemistry A* **2016**, *4* (33), 12686–12713.
21. Kroto, H. W.; Heath, J. R.; O'Brien, S. C.; Curl, R. F.; Smalley, R. E. *Nature* **1985**, *318*, 162.
22. Z. Wang, P. Li, Y. Chen,* Jingbo Liu, Hongjun Tian, Jinhao Zhou, W. Z. and Y. L. *Polymer Preprints, Japan* **2014**, *2*, 7396–7401.
23. Matsoso, B. J.; Ranganathan, K.; Mutuma, B. K.; Lerotholi, T.; Jones, G.; Coville, N. J. *RSC Advances* **2016**, *6* (108), 106914–106920.
24. Hlekelele, L.; Franklyn, P. J.; Tripathi, P. K.; Durbach, S. H. *RSC Advances* **2016**, *6* (80), 76773–76779.
25. Song, A.; Yang, W.; Yang, W.; Sun, G.; Yin, X.; Gao, L.; Wang, Y.; Qin, X.; Shao, G. *ACS Sustainable Chemistry and Engineering* **2017**, *5* (5), 3973–3981.
26. Ayala, P.; Arenal, R.; Rümmeli, M.; Rubio, A.; Pichler, T. *Carbon* **2010**, *48* (3), 575–586.
27. Hu, B.; Wang, K.; Wu, L.; Yu, S. H.; Antonietti, M.; Titirici, M. M. *Advanced Materials* **2010**, *22* (7), 813–828.
28. Nongwe, I.; Ravat, V.; Meijboom, R.; Coville, N. J. *Applied Catalysis A: General* **2013**, *466*, 1–8.
29. Xiong, H.; Motchelaho, M. A.; Moyo, M.; Jewell, L. L.; Coville, N. J. *Applied*

Catalysis A: General **2014**, *482*, 377–386.

30. Han, J.; Xu, G.; Ding, B.; Pan, J.; Dou, H.; MacFarlane, D. R. *Journal of Materials Chemistry A* **2014**, *2* (15), 5352–5357.
31. Plonska-Brzezinska, M. E.; Molina-Ontoria, A.; Echegoyen, L. *Carbon* **2014**, *67*, 304–317.
32. Li, Q.; Zhang, S.; Dai, L.; Li, L. S. *Journal of the American Chemical Society* **2012**, *134* (46), 18932–18935.
33. Wang, G.; Wang, R.; Liu, L.; Zhang, H.; Du, J.; Zhang, Y.; Liu, M.; Liang, K.; Chen, A. *Materials Letters* **2017**, *197*, 71–74.
34. Li, W.; Chen, D.; Li, Z.; Shi, Y.; Wan, Y.; Wang, G.; Jiang, Z.; Zhao, D. *Carbon* **2007**, *45* (9), 1757–1763.
35. Li, R.; Cao, A.; Zhang, Y.; Li, G.; Jiang, F.; Li, S.; Chen, D.; Wang, C.; Ge, J.; Shu, C. *ACS Applied Materials and Interfaces* **2014**, *6* (23), 20574–20578.
36. Fang, B.; Kim, M.; Kim, J. H.; Yu, J. S. *Langmuir* **2008**, *24* (20), 12068–12072.
37. http://www.Askiitian.com/iit-jee-s-and-p-block-elements/allotropes-of-carbon/ 23/02/2017
38. Hu, F. P.; Wang, Z.; Li, Y.; Li, C.; Zhang, X.; Shen, P. K. *Journal of Power Sources* **2008**, *177* (1), 61–66.
39. Wu, J.; Jin, C.; Yang, Z.; Tian, J.; Yang, R. *Carbon* **2015**, *82* (C), 562–571.
40. Yan, W.; Wang, L.; Chen, C.; Zhang, D.; Li, A. J.; Yao, Z.; Shi, L. Y. *Electrochimica Acta* **2016**, *188*, 230–239.
41. Zhou, T.; Zhou, Y.; Ma, R.; Zhou, Z.; Liu, G.; Liu, Q.; Zhu, Y.; Wang, J. *Carbon* **2017**, *114*, 177–186.
42. Phaahlamohlaka, T. N.; Kumi, D. O.; Dlamini, M. W.; Forbes, R.; Jewell, L. L.; Billing, D. G.; Coville, N. J. *ACS Catalysis* **2017**, *7* (3), 1568–1578.
43. Subramanian, V.; Cheng, K.; Lancelot, C.; Heyte, S.; Paul, S.; Moldovan, S.; Ersen, O.; Marinova, M.; Ordomsky, V. V.; Khodakov, A. Y. *ACS Catalysis* **2016**, *6* (3), 1785–1792.
44. Zhang, Z.; Xiao, F.; Xi, J.; Sun, T.; Xiao, S.; Wang, H.; Wang, S.; Liu, Y. *Scientific Reports* **2014**, *4*, 1–5.
45. Bian, S. W.; Liu, S.; Guo, M. X.; Xu, L. L.; Chang, L. *RSC Advances* **2015**, *5* (16), 11913–11916.
46. Liu, R.; Qu, F.; Guo, Y.; Yao, N.; Priestley, R. D. *Chemical Communications* **2014**, *50* (4), 478–480.

47. Phaahlamohlaka, T. N.; Kumi, D. O.; Dlamini, M. W.; Jewell, L. L.; Coville, N. J. *Catalysis Today* **2016**, *275*, 76–83.
48. Liu, Y.; Goebl, J.; Yin, Y. *Chemical Society Reviews* **2013**, *42* (7), 2610–2653.
49. Liu, J.; Wickramaratne, N. P.; Qiao, S. Z.; Jaroniec, M. *Nature Materials* **2015**, *14* (8), 763–774.
50. Ouyang, Y.; Shi, H.; Fu, R.; Wu, D. *Scientific Reports* **2013**, *3*, 1–6.
51. Chen, X.; Kierzek, K.; Jiang, Z.; Chen, H.; Tang, T.; Wojtoniszak, M.; Kalenczuk, R. J.; Chu, P. K.; Borowiak-Palen, E. *Journal of Physical Chemistry C* **2011**, *115* (36), 17717–17724.
52. Chen, X.; Kierzek, K.; Cendrowski, K.; Pelech, I.; Zhao, X.; Feng, J.; Kalenczuk, R. J.; Tang, T.; Mijowska, E. *Colloids and Surfaces A: Physicochemical and Engineering Aspects* **2012**, *396*, 246– 250
53. Yang, T.; Liu, J.; Zheng, Y.; Monteiro, M. J.; Qiao, S. Z. *Chemistry - A European Journal* **2013**, *19* (22), 6942–6945.
54. Chen, X.; Kierzek, K.; Wenelska, K.; Cendrowski, K.; Gong, J.; Wen, X.; Tang, T.; Chu, P. K.; Mijowska, E. *Chemistry - An Asian Journal* **2013**, *8* (11), 2627–2633.
55. Lee, H. J.; Choi, S.; Oh, M. *Chemical Communications* **2014**, *50* (34), 4492–4495.
56. Yin, C.; Huang, Q.; Liu, B.; Wang, X.; Xie, Y.; He, L.; Zhang, M.; Yang, X. *Materials Letters* **2007**, *61* (19–20), 4015–4018.
57. Bai, Z.; Zhang, Y.; Fan, N.; Guo, C.; Tang, B. *Materials Letters* **2014**, *119*, 16–19.
58. Li H.; Zhao, N.; He, C.; Shi, C.; Du, X.; L.i, J. *Journal of Alloys and Compounds* **2008**, *465*, 387–390.
59. Chien, C. H.; Sheng, P. S.; Wang, C. H.; Huang, C. H.; Lin, H. K.; Lee, C. Y.; Chiu, H. T. *Materials Letters* **2008**, *62* (8–9), 1176–1178.
60. Zhang, J.; Wang, K.; Guo, S.; Wang, S.; Liang, Z.; Chen, Z.; Fu, J.; Xu, Q. *ACS Applied Materials and Interfaces* **2014**, *6* (3), 2192–2198.
61. Boëhm, H. P. *Carbon* **2002**, *40*, 145–149.
62. Figueiredo, J. L.; Pereira, M. F. R.; Freitas, M. M. A.; Órfão, J. J. M. *Carbon* **1999**, *37*, 1379–1389.
63. Saha, M. S.; Kundu, A. *Journal of Power Sources* **2010**, *195* (19), 6255–6261.
64. Xiong, H.; Moyo, M.; Motchelaho, M. A.; Tetana, Z. N.; Dube, S. M. A.; Jewell, L. L.; Coville, N. J. *Journal of Catalysis* **2014**, *311*, 80–87.
65. Corpuz, A. R.; Wood, K. N.; Pylypenko, S.; Dameron, A. A.; Joghee, P.; Olson, T. S.; Bender, G.; Dinh, H. N.; Gennett, T.; Richards, R. M.; O'Hayre, R. *Journal of Power*

Sources **2014**, *248*, 296–306.

66. Qi, J.; Li, Y.; Wei, G.; Li, J.; Sun, X.; Shen, J.; Han, W.; Wang, L. *Separation and Purification Technology* **2017**, *188*, 112–118.
67. Yoon, H.; Ko, S.; Jang, J. *Chemical Communications* **2007**, No. 14, 1468–1470.
68. Chen, Y.; Wang, J.; Liu, H.; Banis, M. N.; Li, R.; Sun, X.; Sham, T. K.; Ye, S.; Knights, S. *Journal of Physical Chemistry C* **2011**, *115* (9), 3769–3776.
69. Feng, Y.; Yang, W.; Wang, N.; Chu, W.; Liu, D. *Journal of Analytical and Applied Pyrolysis* **2014**, *107*, 204–210.
70. Kente, T.; Mhlanga, S. D. *Journal of Crystal Growth* **2016**, *444*, 55–72.
71. Lee, W. H.; Moon, J. H. *ACS Applied Materials and Interfaces* **2014**, *6* (16), 13968–13976.
72. Jeong, H. M.; Lee, S. Y.; Shin, W. H.; Kwon, J. H.; Shakoor, A.; Hwang, T. H.; Kim, S. Y.; Kong, B. S.; Seo, J. S.; Lee, Y. M.; Kang, J. K.; Choi, J. W. *RSC Advances* **2012**, *2* (10), 4311–4317.
73. Wu, Z.; Webley, P. A.; Zhao, D. *Journal of Materials Chemistry* **2012**, *22* (22), 11379–11389.
74. Liao, Y.; Gao, L.; Zhang, X.; Chen, J. *Materials Research Bulletin* **2012**, *47* (7), 1625–1629.
75. Yang, F.; Zhang, Z.; Du, K.; Zhao, X.; Chen, W.; Lai, Y.; Li, J. *Carbon* **2015**, *91*, 88–95.
76. Li, Y. H.; Hung, T. H.; Chen, C. W. *Carbon* **2009**, *47* (3), 850–855.
77. Choi, B.; Yoon, H.; Park, I. S.; Jang, J.; Sung, Y. E. *Carbon* **2007**, *45* (13), 2496–2501.
78. Arrigo, R.; Schuster, M. E.; Xie, Z.; Yi, Y.; Wowsnick, G.; Sun, L. L.; Hermann, K. E.; Friedrich, M.; Kast, P.; Hävecker, M.; Knop-Gericke, A.; Schlögl, R. *ACS Catalysis* **2015**, *5* (5), 2740–2753.
79. Zhang, L.; Wang, A.; Wang, W.; Huang, Y.; Liu, X.; Miao, S.; Liu, J.; Zhang, T. *ACS Catalysis* **2015**, *5* (11), 6563–6572.
80. Su, D. S.; Perathoner, S.; Centi, G. *Chemical Reviews* **2013**, *113* (8), 5782–5816.
81. Stonkus, O. A.; Kibis, L. S.; Podyacheva, O. Y.; Slavinskaya, E. M.; Zaikovskii, V. I.; Hassan, A. H.; Hampel, S.; Leonhardt, A.; Ismagilov, Z. R.; Noskov, A. S.; Boronin, A. I. *ChemCatChem* **2014**, *6* (7), 2115–2128.
82. Liu, X.; Sui, Y.; Duan, T.; Meng, C.; Han, Y. *Catalysis Science and Technology* **2015**, *5* (3), 1658–1667.

83. Chen, S.; Qi, P.; Chen, J.; Yuan, Y. *RSC Advances* **2015**, *5* (40), 31566–31574.
84. Xiong, H.; Moyo, M.; Rayner, M. K.; Jewell, L. L.; Billing, D. G.; Coville, N. J. *ChemCatChem* **2010**, *2* (5), 514–518.
85. Yang, Y.; Jia, L.; Hou, B.; Li, D.; Wang, J.; Sun, Y. *ChemCatChem* **2014**, *6* (1), 319–327.
86. Li, S.; Yao, N.; Zhao, F.; Li, X. *Catalysis Science and Technology* **2016**, *6* (7), 2188–2194.
87. Lu, J.; Yang, L.; Xu, B.; Wu, Q.; Zhang, D.; Yuan, S.; Zhai, Y.; Wang, X.; Fan, Y.; Hu, Z. *ACS Catalysis* **2014**, *4* (2), 613–621.
88. Chew, L. M.; Xia, W.; Düdder, H.; Weide, P.; Ruland, H.; Muhler, M. *Catalysis Today* **2016**, *270*, 85–92.
89. Yang, Y.; Jia, L.; Hou, B.; Li, D.; Wang, J.; Sun, Y. *Journal of Physical Chemistry C* **2014**, *118* (1), 268–277.
90. Conner, W. C.; Falconer, J. L. *Chemical Reviews* **1995**, *95* (3), 759–788.
91. Psofogiannakis, G. M.; Froudakis, G. E. *Chemical Communications* **2011**, *47* (28), 7933–7943.
92. Nabaho, D.; Niemantsverdriet, J. W.; Claeys, M.; Steen, E. van. *Catalysis Today* **2016**, *216*, 17–27.
93. Im, J.; Shin, H.; Jang, H.; Kim, H.; Choi, M. *Nature Communications* **2014**, *5*, 1–8.
94. Prins, R. *Chemical Reviews* **2012**, *112* (5), 2714–2738.
95. Khoobiar, S. *Journal of Physical Chemistry* **1964**, *68* (2), 411–412.
96. Pimerzin, A. A.; Nikulshin, P. A.; Mozhaev, A. V.; Pimerzin, A. A.; Lyashenko, A. I. *Applied Catalysis B: Environmental* **2015**, *168–169*, 396–407.
97. Sha, X.; Chen, L.; Cooper, A. C.; Pez, G. P.; Cheng, H. *Journal of Physical Chemistry C* **2009**, *113* (26), 11399–11407.
98. Jermwongratanachai, T.; Jacobs, G.; Shafer, W. D.; Pendyala, V. R. R.; Ma, W.; Gnanamani, M. K.; Hopps, S.; Thomas, G. A.; Kitiyanan, B.; Khalid, S.; Davis, B. H. *Catalysis Today* **2014**, *228*, 15–21.
99. M. de Beer, A. Kunene, D. Nabaho, M. Claeys, E. van S. *The Journal of The Southern African Institute of Mining and Metallurgy* **2014**, *114*, 157–165.
100. Jung, J. S.; Lee, J. S.; Choi, G.; Ramesh, S.; Moon, D. J. *Fuel* **2015**, *149*, 118–129.
101. Ma, W.; Jacobs, G.; Keogh, R. A.; Bukur, D. B.; Davis, B. H. *Applied Catalysis A: General* **2012**, *437–438*, 1–9.

102. Diehl. F.; Khodakov. A. Y. *Oil & Gas Science and Technology - Revue d'IFP Energies nouvelles* **2009**, *64* (1), 11–24.

103. Hong, J.; Chernavskii, P. A.; Khodakov, A. Y.; Chu, W. *Catalysis Today* **2009**, *140* (3–4), 135–141.

104. Zhang, H.; Chu, W.; Zou, C.; Huang, Z.; Ye, Z.; Zhu, L. *Catalysis Letters* **2011**, *141*, 438–444

105. Carlsson, A. F.; Naschitzki, M.; Bäumer, M.; Freund, H. J. *Journal of Physical Chemistry B* **2003**, *107* (3), 778–785.

106. Wang, L.; Yang, R. T. *Energy and Environmental Science* **2008**, *1* (2), 268–279.

107. Beaumont, S. K.; Alayoglu, S.; Specht, C.; Kruse, N.; Somorjai, G. A. *Nano Letters* **2014**, *14* (8), 4792–4796.

108. Tománek, D.; Mukherjee, S.; Kumar, V.; Bennemann, K. H. *Surface Science* **1982**, *114* (1), 11–22.

109. Choi, M.; Yook, S.; Kim, H. *ChemCatChem* **2015**, *7* (7), 1048–1057.

110. Chen, L.; Cooper, A. C.; Pez, G. P.; Cheng, H. *Journal of Physical Chemistry C* **2007**, *111* (51), 18995–19000.

111. Psofogiannakis, G. M.; Froudakis, G. E. *Journal of American Chemical Society: communication* **2009**, *131*, 15133–15135.

112. Pyle, D. S.; Gray, E. M. A.; Webb, C. J. *International Journal of Hydrogen Energy* **2016**, *41* (42), 19098–19113.

CHAPTER 3

General experimental methods and Fischer-Tropsch reactor conditions

3.1. Introduction

In the field of material sciences, a wide range of carbon based materials (in the nano scale) have synthesized. These include carbon nanotube, carbon dots, nano onions, solid carbon spheres, and hollow carbon spheres. These carbon materials have been used in numerous devices, as catalysts and as supports. Herein, nitrogen-doped hollow carbon spheres were studied as a possible hydrogen transport layer and a Fischer-Tropsch catalyst support. Evaluation of the physio-chemical properties of carbon based material is important for an understanding of their possible success in applications. This chapter provides a thorough explanation of the catalyst synthesis procedures and characterization techniques used in the dissertation.

The hard templating method and a horizontal chemical vapour deposition (CVD) reactor were used during the synthesis of nitrogen-doped hollow carbon spheres. The CVD reactor was used to facilitate the annealing of the polymeric carbon precursor, incorporation of nitrogen groups and decomposition of the template.

Several analytical techniques were employed to evaluate the chemical and physical properties of the catalysts. The catalysts were analysed using transmission electron microscopy (TEM) to determine the features of the internal morphology of the carbon and scanning electron microscopy (SEM) to evaluate the external morphology of the materials. SEM was coupled with energy dispersive X-ray spectroscopy (SEM-EDS) to evaluate the elemental composition; Laser Raman spectroscopy (LRS) was used to establish the graphitic nature of the carbon support; Brunauer–Emmett–Teller (BET) was used to facilitate the surface area and pore volume measurements; powder x-ray diffraction (PXRD) was used to establish the crystallographic planes of the elements detected by EDS; thermo gravimetric analysis (TGA) was used to establish the thermal stability of the catalysts and the metal loading on the catalysts; X-ray photoelectron spectroscopy (XPS) was used to determine the bonding

configurations within the carbon support and CHNS for the determination of light elements. The reducibility of the catalysts was assessed using the in situ powder X-ray diffraction (in situ PXRD) technique and the temperature programmed reduction (TPR) technique. The Fischer Tropsch synthesis setup used during the catalytic evaluation of the catalysts will also be described in this chapter.

3.2. Synthesis methodology

3.2.1. Materials

Most of the chemicals used in this research project were purchased from Merck or Sigma Aldrich, and were used without further purification. Styrene (Sigma), polyvinylpyrollidone (PVP, MW 40 k, Sigma), potassium persulfate (KPS, Eimer and Amend), cobalt nitrate hexahydrate ($Co(NO_3)_2.6H_2O$, Sigma), ruthenium chloride hydrate ($RuCl_3.H_2O$, Sigma), hydrazine (35 %, Sigma), ammonia solution (25%, Fluka), hexadecyltrimethylammonium bromide (CTAB, Sigma), resorcinol (Sigma), formaldehyde solution (37 %, Sigma) ethanol (98 %, Merck), melamine (Sigma), methanol (Merk), urea (Promark chemicals), ethylene glycol (Sigma). Deionized water was used in the experiments and was supplied by the School of Chemistry.

3.2.2 Synthesis of nitrogen doped hollow carbon spheres

Carbonaceous spheres with spherical and hollow morphology were synthesized using the hard templating technique [1-3]. The hard templating technique is comprised of three main steps:-

(i) Synthesis of the template

(ii) Shell formation of the desired material on the template surface i.e. loading metal catalyst and/or coating with carbon source around the template

(iii) Template decomposition [4]

Herein, polystyrene [5-6] was used as the hard template and resorcinol-formaldehyde [7] as the carbon precursor. Melamine was used as the nitrogen precursor and incorporated by a post doping [8] technique. The synthesis methodology is schematically illustrates on figure 3.1.

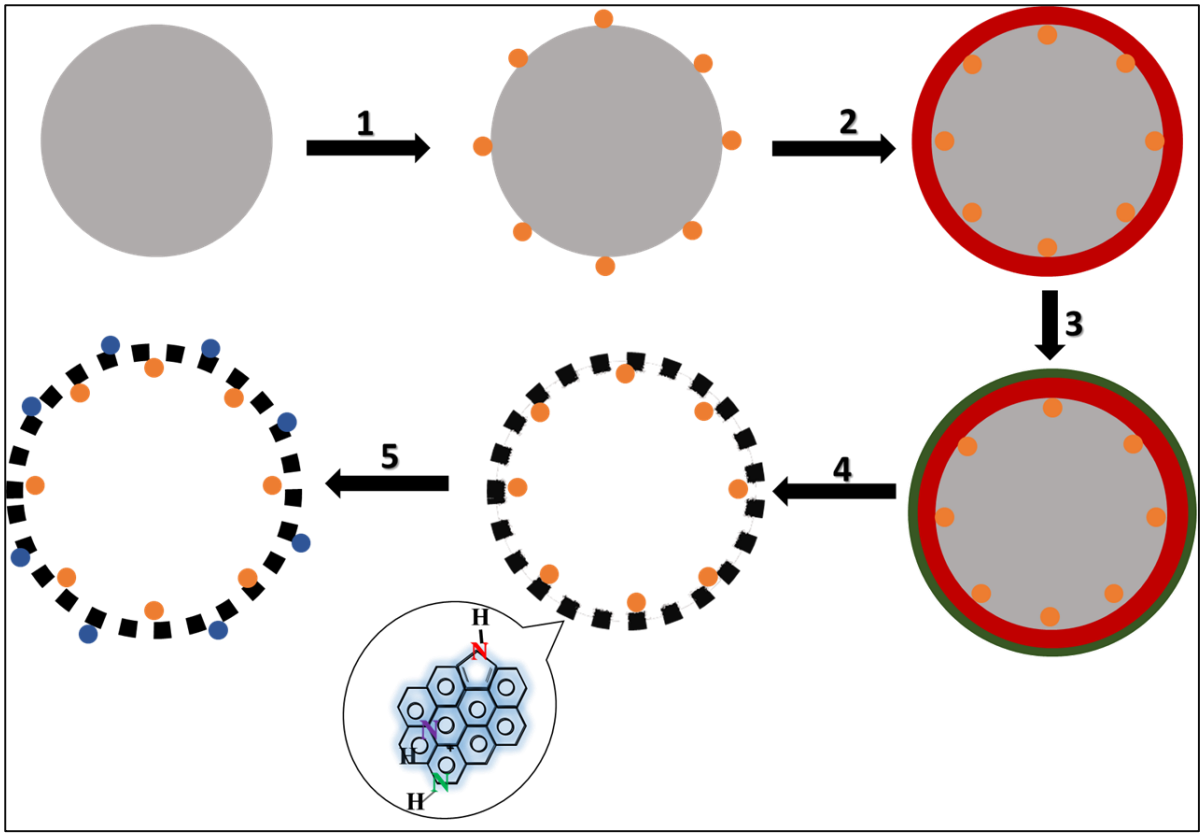


Figure 3.1 Schematic representation of the synthesis methodology. **(1)** Metal (Ru and Co) loaded onto a polystyrene template; **(2)** resorcinol-formaldehyde (carbon precursor) coating; **(3)** melamine (nitrogen precursor) coating, **(4)** template decomposition and annealing and **(5)** Ru metal loaded onto the nitrogen doped carbon support.

3.2.2.1. Synthesis of hard template (polystyrene spheres)

A water-ethanol mixture (200 mL water and 50 mL ethanol) was magnetically stirred inside a round-bottom flask for 10 minutes to obtain a homogeneous solution. To this solution, styrene (8 mL) and PVP (0.1 g), were added and the resulting mixture was ultra-sonicated for 30 minutes. Furthermore a separately prepared KPS solution (0.15 g in 20 mL water) was added and the mixture was allowed to stir magnetically for 15 minutes. The mixture was then heated at 80 °C under reflux for 24 hours. The product was collected by centrifugation, washed 3 times using ethanol and dried overnight at 60 °C. The dry product was crushed and stored in a sample vial and labelled PSS. The product yield was calculated to be 95 %.

3.2.2.2. Loading metal nanoparticles on a template surface

This step was successfully conducted by a homogeneous deposition precipitation method, using hydrazine as the reducing agent. [9] The hydrated salts of Co and Ru were used as the metal precursors. Briefly, polystyrene spheres (PSS, 2 g) were added to a water-ethanol solution (50 mL water and 15 mL ethanol) followed by a 30 minutes ultra-sonication so as to disperse the polystyrene spheres. The hydrated Co salt (Co $(NO_3)_2.6H_2O$, 0.3 g) was added to the sonicated mixture and stirred for 5 minutes as to dissolve and disperse the metal salt. The co-deposition of the Co metal and the Ru metal was done by mixing together the hydrated Co salt (Co $(NO_3)_2.6H_2O$, 0.3 g) with a solution of the Ru salt ($RuCl_3.H_2O$, 0.01M, 4 mL) and then added to the sonicated mixture. Subsequently, a solution of hydrazine (2 M, 10 mL) was slowly added to adequately reduce the metal precursors. During this step a change of colour (red to blue for Co and red to grey for Co-Ru) within the reaction was attributed to the success of reduction of metals to their metallic state. The mixture was stirred for 24 hours, then filtered, washed with ethanol and dried in air at 80 °C for 12 hours.

The dried samples were ground and stored in a sample vial labelled Co/PSS or Co-Ru/PSS.

3.2.2.3. Synthesis of pristine and metal encapsulated nitrogen doped hollow carbon spheres

A metal loaded template or a pristine template (Co/PSS or Co-Ru/PSS or PSS, 2 g) was added into a homogeneous water-ethanol-ammonia solution (50 mL water; 100 mL ethanol and 1 mL ammonia) and sonicated for 30 minutes as to disperse the template. A separated homogenous mixture was prepared containing 50 mL ethanol, 1 g CTAB, 0.75 g resorcinol, and 1.5 mL formaldehyde. The two mixtures were added together and sonicated for 10 minutes and further stirred at room temperature for 24 hours to coat the resorcinol-formaldehyde (RF) polymer around the spherical template. The resulting reddish-brown solution was filtered, washed 4 times with 100 mL distilled water and dried at 80 °C for 12 hours.

The dried samples were ground and stored in a sample vial labelled Co/PSS@ RF or Co-Ru/PSS@RF or PSS@RF.

Nitrogen incorporation was conducted using the post doping method. Briefly, melamine (0.5 g) was added into methanol (100 mL) and this mixture was stirred for an hour to disperse the melamine. The composite (Co/PSS@ RF or Co-Ru/PSS@RF or PSS@RF; 2 g) was added to the melamine-ethanol solution. The resulting mixture was stirred until all the methanol had

evaporated. This resulting composite was ground and stored in a sample vail labelled Co/PSS@RF-melamine or Co-Ru/PSS@RF-melamine or PSS@RF-melamine.

The carbonization of the samples was successfully conducted using a horizontal CVD reactor, under inert conditions using inert gas (nitrogen) at flow rate of 50 mL/min. This was done in a successive two-step process, which involved the decomposition of the template (350 °C) and the carbon annealing (600 °C). Briefly, 0.5 g composite (Co/PSS@RF-melamine or Co-Ru/PSS@RF-melamine or PSS@RF-melamine.) was weighed in a quartz boat (60 mm length, 30 mm width, 15 mm height and 5 mm quarts thickness), placed in the middle of a quartz tube and placed (quartz tube with boat) inside the horizontal CVD reactor. The decomposition temperature of the template was set to 350 °C, with a ramping rate of 3 °C/min and holding time of 1 hour. The carbon annealing temperature of the polymer was set to 600 °C with a ramping rate of 3°C/min and holding time of 1 or 2 hour (s). The black product was ground and stored in a sample vial labelled Co@NHCS or Co-Ru@NHCS or NHCS.

The catalysts, Co@NHCS and Co-Ru@NHCS, were calcined at 210 °C for 2 hours under a flow of 5% O_2/bal Ar (50mL/min) gas mixture. This step was done to ensure that all metallic Co was converted to Co_3O_4 phase.

3.2.2.4. Loading metal nanoparticle on nitrogen doped hollow carbon spheres

The synthesis of the Co and Ru catalysts was done using the wetness impregnation (WI) method. [10] Briefly, a calculated and weighed amount of the metal salt was dissolved in 5 mL ethanol. The metal salt solution was then added drop wise onto the Co@NHCSs catalyst or NHCS support while stirring vigorously to form a thick paste. The paste was stirred until the ethanol solution had evaporated and dried at 60 °C for 12 hours. The dried sample was thermally treated at 300 °C for 2 hours under nitrogen to decompose the metal precursor. This sample was labelled Co@NHCS@Ru or Co-Ru/NHCS or Co/NHCS.

The catalysts Co@NHCS@Ru, Co-Ru/NHCS and Co/NHCS were calcined at 210 °C for 2 hours under a flow of 5% O_2/bal Ar (50mL/min) gas mixture. This step was done to ensure that all metallic Co was converted to Co_3O_4 phase.

3.3. Material characterization techniques

3.3.1. Powder X-ray diffraction (PXRD)

Powder X-ray diffraction (PXRD) is a bulk technique which assists in the qualitative and quantitative identification of phases in powdered solid samples. The identification or fingerprint of a sample is in the form of a diffraction pattern that results from the interaction of X-rays with the solid (crystalline or amorphous) sample. The interaction follows Bragg's law which is mathematically given as $n\lambda = 2d \sin\theta$, where n is an integer, λ is the wavelength of the X-rays, d is the lattice spacing and θ is the angle of diffraction. [11]

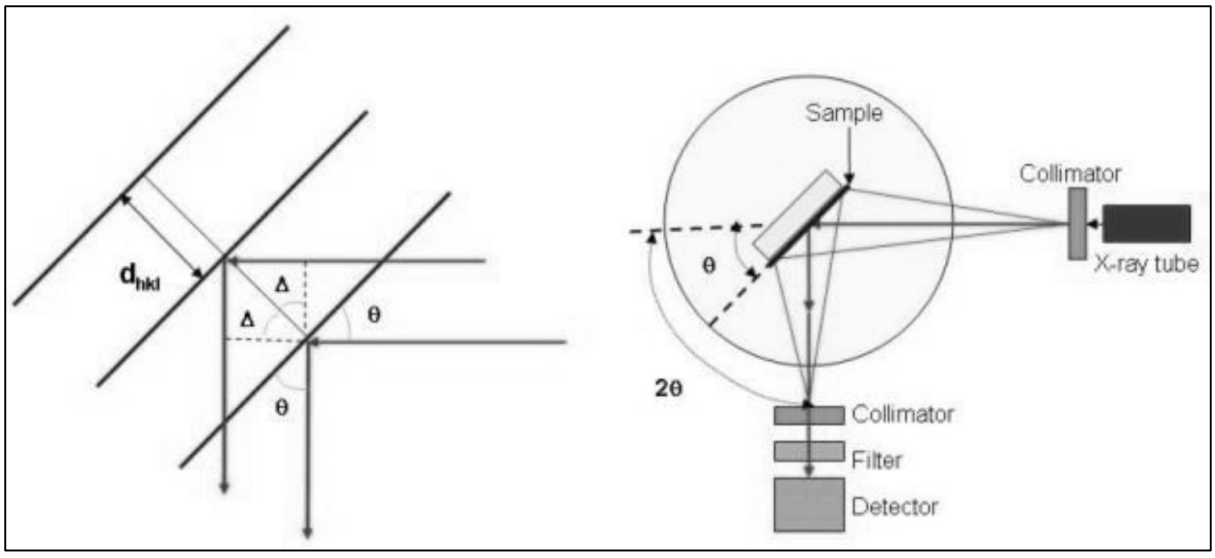


Figure 3.2 Bragg's schematic and a typical setup on an XRD diffractometer. [12]

For this study, catalysts were characterized using a Bruker D2 Phaser PXRD, as shown in figure 3.3. The instrumentation utilized a Cu-Kα radiation ($\lambda_{K\alpha}$ = 1.54 Å), a Lynxeye detector, operated at 30 kV voltage and 30 mA current with scan range of $2\theta = 10° - 90°$. The samples were prepared using the packing preparation method, whereby the finely powdered sample was packed onto the sample holder and made flat using a clean glass plate.



Figure 3.3 The Bruker D2 Phaser PXRD fitted with a LynxEye detector.

3.3.2. Thermal gravimetric analysis (TGA)

The thermal gravimetric analysis (TGA) technique is used to assess the thermal stability and purity, as loss of mass over time, of supported metal catalysts and other materials under oxidizing conditions. The changes in mass of the sample could result from oxidation or decomposition. Metals are known to have high thermal stability, hence this technique allows for the calculation of the metal loading which remains as residue after a carbon support has been fully oxidised to carbon dioxide. The basic principle of this technique is that a sample is subjected to gaseous condition (flow of air and nitrogen gases) and is continuously heated at a programmed rate of gas flow and heat increment. A thermograph (% weight vs. time) and derivative thermograph are obtainable and these are interpreted to give a pattern of mass loss and exact decomposition temperature respectively.

For this study, the thermal stability of the catalysts was characterized using a Perkin Elmer TGA 6000, as shown in figure 3.4. For an analysis, approximately 10 mg of catalyst was weighed and placed inside the alumina sample pan using a spatula. Using a tweezer, the sample pan was carefully held and placed centrally on the analytical balance of the instrument. The sample was then purged at room temperature with an inert gas (nitrogen, 10

mL/min) for 5 minutes. Subsequently, the furnace chamber was continuous heated up to 900 °C at a heating rate of 10 °/min.

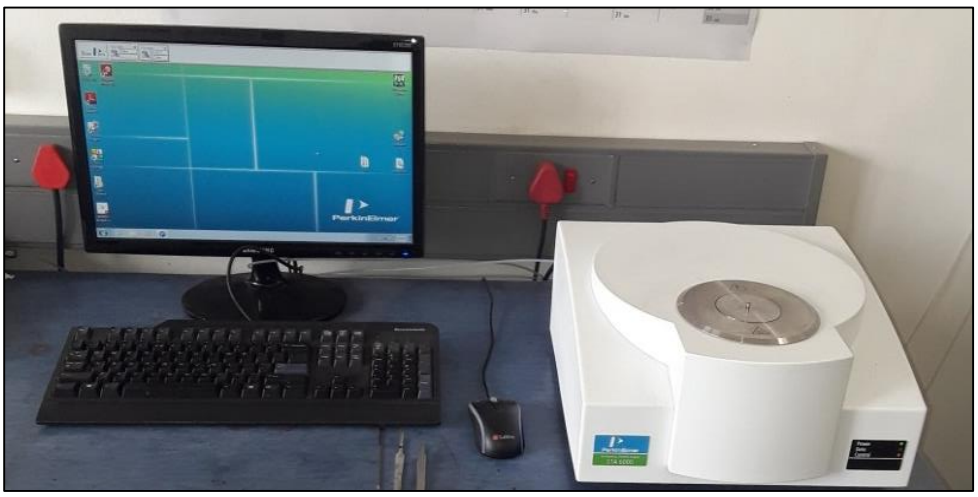


Figure 3.4 Perkin Elmer TGA 6000 thermal analyser.

3.3.3. Brunauer, Emmet and Teller (BET) method

Nanotechnology application fields such as catalysis rely highly on surface area and hence the importance of surface area characterization of nanomaterials prior to use is important. Nanomaterials have an enhanced surface area to volume ratio in comparison to their bulk counterparts. Brunauer, Emmet and Teller (BET) analysis, named after its authors Stephen Brunauer; Paul Hugh Emmett and Edward Teller in 1938, is an extensively used characterization technique for the total surface area measurements through surface adsorption. The BET analysis extends on the Langmuir theory thus represents surface area based on monolayer adsorption and partial multilayer adsorption capacity and assumes that during the adsorption process there is surface homogeneity, complete gas adsorption at saturation level, limited interaction of molecules and kinetic limitations.[13] During BET analysis, a liquid nitrogen bath (-195 °C) is used as an adsorbate.

Following the above mentioned assumption, the elementary reaction rates can be used to determine the rates of adsorption and desorption, allowing for the BET equation shown in equation (1) where v is the adsorbed volume of gas, v_m is the adsorbed monolayer volume, p is the equilibrium gas pressure, p_0 is the saturation pressure and $\boldsymbol{c}$ is the BET constant. [14]

$$v = \frac{v_m cp}{(p_{0-}\ p)[1+(c-1)\frac{p}{p_0}]} \quad (1)$$

In this study, a Micromeritics Tristar 3000 (RS232), shown on figure 3.5, was used for surface area and porosity analyses. Prior to the start of recording the surface area and porosity, a precisely weighed 200 mg sample was degassed in an inert environment (nitrogen gas) at 170 °C for 12 hours using a vacuum pump to remove all adsorbed volatiles. Subsequently, the degassed sample was placed in a liquid nitrogen bath (-195 °C) and ultra-pure nitrogen gas was passed over the sample and the adsorption was recorded.



Figure 3.5 Micromeritics RS232 Brunauer -Emmett-Teller (BET) analyser.

3.3.4. Laser Raman spectroscopy

Raman spectroscopy is a simple, non-destructive and high resolution technique used for the characterisation of carbon allotropes of different dimensions such as graphene (2D); graphite (3D) and carbon nanotubes (1D) through inelastic scattering of light phonons. Raman spectroscopy helps to characterize the carbon allotropes and to relate their properties to electronic (crystallography) and structural (layering) properties. For example, the interaction of phonons with the sample electrons give an indication of defects or edges in a sample. [15] Moreover, Raman spectra (intensity vs. wavenumber) of carbon have two dominant peaks (among others), known as the D peak at lower wave number (1350 cm^{-1}) and the G peak at higher wavenumbers (1590 cm^{-1}). The D peak corresponds to the sp^3 breathing modes while

the G peak corresponds to the high-frequency E_2g vibrations. [16] Thus the intensity and region of the peaks in a Raman spectrum are able to clearly indicate the amorphous nature or disorder resulting from the incorporation of defects (doping).

For this study a Bruker Senterra laser Raman spectrometer, shown on figure 3.6, fitted for imaging was used. A 532 nm excitation wavelength and a 50 X objective lens were used during imaging. The analysis was done in triplicate to obtain an averaged spectrum.

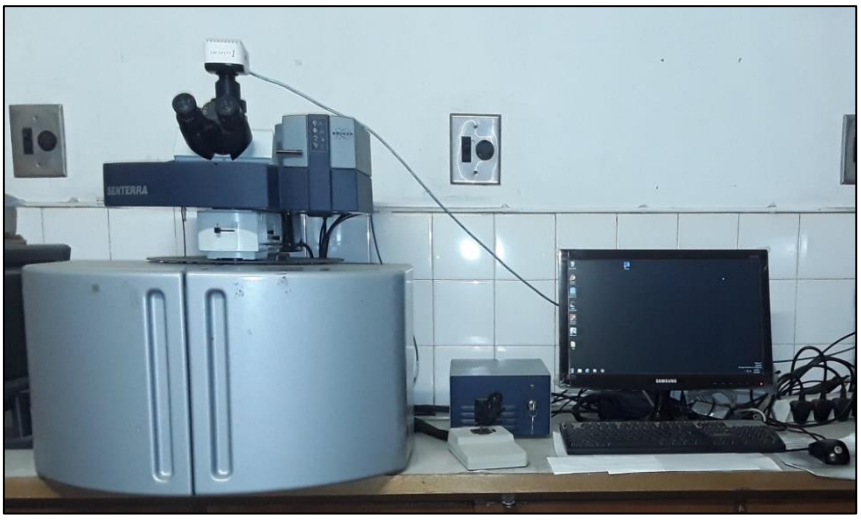


Figure 3.6 Bruker Senterra Laser Raman spectrometer.

3.3.5. Transmission electron microscopy (TEM)

The internal structure of catalysts, and their shape and size, was analysed using transmission electron microscopy (TEM), a high resolution imaging technique. The TEM imaging instrument is a long column instrument comprised of (i) a field emission gun that generated a high energy (high voltage) beam of electrons, (ii) a series of lenses (condenser and objective) and apertures that respectively focus/direct the monochromatic electron downwards of the column to the sample and decrease spherical or chromatic aberration or stigmatism, (iii) a florescence screen that illuminates the sample and (iv) a charge-coupled device (CCD) camera which facilitated the visualization and image capturing. [17]

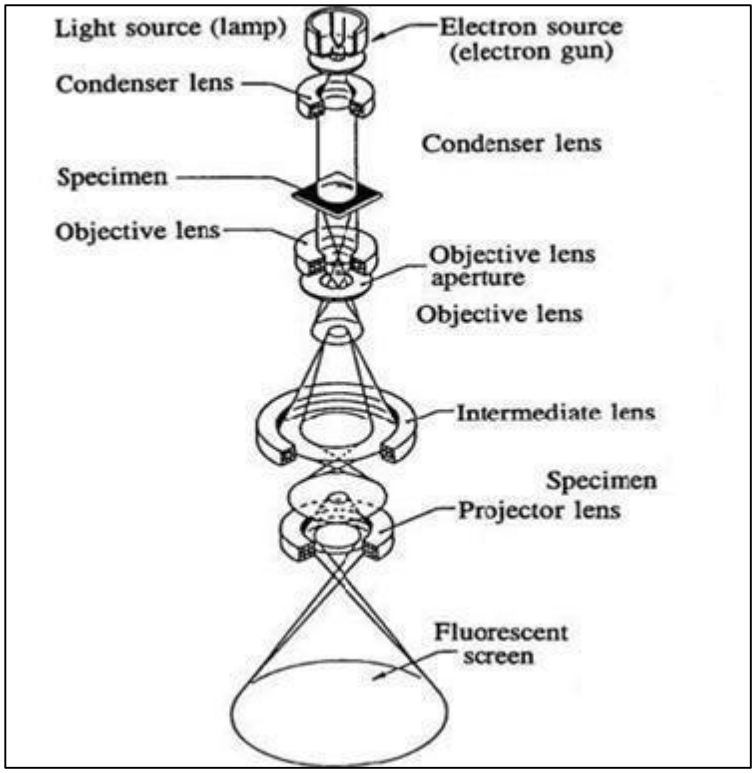


Figure 3.7 Schematic of main components found in a TEM instrument. [18]

For this study, a FEI Tecnai T12 transmission electron microscope, shown in fig. 3.8, in the bright field mode was used to morphologically characterize the catalysts. The preparation of the samples involved dispersing a small amount of the material in methanol (1 mg in 10 ml) and ultrasonicating for 20 minutes. The 2 drops of the sonicated solution were then added to a clean SPI (Structure Probe, Inc.) carbon-coated copper grid (200 mesh) and allowed to dry before the start of the analysis.

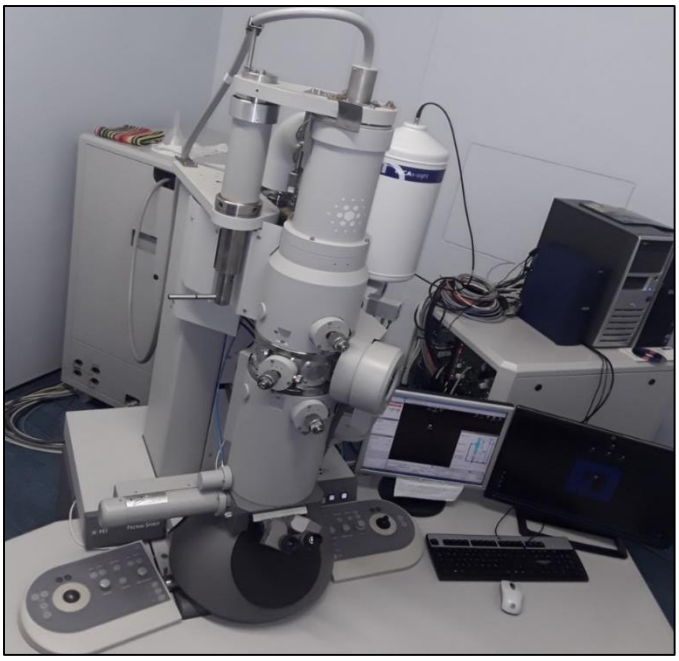


Figure 3.8 The FEI TECNAI T12 transmission electron microscope.

3.3.6. Scanning electron microscopy (SEM)

Scanning electron microscopy (SEM) was used for the characterization of the external morphology of the catalysts and carbon supports. The instrumentation is similar to the TEM instrument discussed above, however SEM only generates topographical information as electrons only scan the sample surface. The main components of an SEM instrument, as shown in fig. 3.2.1, includes the electron gun (in high vacuum) for the generation an electron beam, electromagnetic lenses and coils to direct a precisely controlled shape and sized beam towards the sample and detectors that are energy/depth-sensitive to specific sample emissions. Mechanistically, upon interaction of a beam (primary electrons) with the sample, scattering occurs to give backscattered (elastic) and secondary (inelastic) electrons. The compositional information relies on the backscattered electron as they penetrate more deeply into the sample in comparison to the secondary electrons.[19]

For this study, a FEI Nova Nanolab 600 SEM, shown in figure 3.10, was used. It was operated at a voltage and spot size of 30 kV and 0.63 nA respectively. The samples were prepared by mounting the sample onto carbon tape. Briefly double sided carbon tape was placed on a stub and a small amount of sample was mounted onto the carbon tape. The

samples were then sputter coated with carbon and gold/palladium coatings as they were non-conductive, thus preventing charging during analysis.

Energy dispersive spectroscopy (EDS) was used to characterize the elemental composition on the catalysts. The EDS analysis was done as a complementary assessment during SEM analysis on the FEI Nova Nanolab 600 SEM using the INCA Microanalysis Suit software.

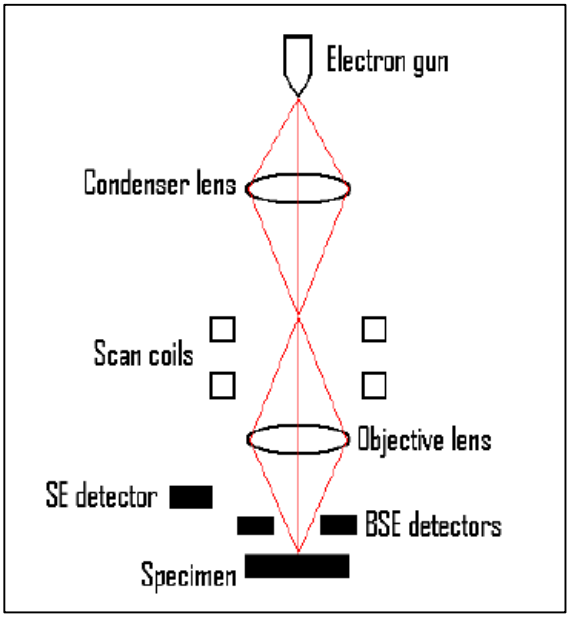


Figure 3.9 Schematic of main components found in a SEM instrument. [19]



Figure 3.10 The FEI Nova Nanolab 600 FEG-SEM/FIB.

3.3.7. X-ray photoelectron spectroscopy (XPS)

X-ray photoelectron spectroscopy (XPS) is a standard and efficient surface technique for characterizing the chemical composition and bonding structure of matter. [20] As a surface technique, penetration of a sample to a depth of 2-10 nm to qualitatively and quantitatively characterize composition of the sample is used. [21]

The process of photoionization is used in XPS, whereby energetic X-rays (photon) are used as radiation to ionize an atom at its core and valence level within a sample, thus releasing the electrons with measurable kinetic energy. These energies thus allow for the determination of the change in binding energy (assume to be relatively proportional to the charge of the atom) that results at different core energy levels as atoms are ionized. Therefore, the more negatively charged compounds have lower binding energies (C<N<O) in comparison to their positive counterparts. [21]

Elements such as C and N can exist in a wide range of bonding configurations and therefore having various hybridizations (sp^1, sp^2 or sp^3). The location of a peak within an XPS spectrum is in itself indicative of its oxidation state and structural identity. The deconvolated spectrum of carbon 1s energies are found to vary from 283 to 288 eV whereas the nitrogen 1s energies are found at 397 eV to 405 eV. [22]

The XPS analysis was done on a Thermo ESCAlab 250Xi using monochromatic X-rays produced from the Al Kα radiation i.e. the 1486.7eV electrons were used, and the experiments were performed at a pressure of 10^{-11} bar. For this study all XPS analyses were conducted at NMISA, CSIR campus in Pretoria.

3.3.8 Carbon, hydrogen, nitrogen (CHN) analysis

The major constituting elements in organic compounds are carbon (C), hydrogen (H) and nitrogen (N). These elements are quantitatively characterized using CHN analysis. During analysis the organic samples are oxidatively decomposed by high temperature treatment in pure oxygen to give their corresponding oxides which are then analysed to give elemental C, H and N. The main components of a CHN analysis are a high temperature reactor; an inert carrier gas, an oxidative catalyst, a reducer and a detector. [23] Briefly, a crushed sample is mixed with an oxidant such as V_2O_5, which improves the oxidation of complex compounds, placed in a tin foil and subjected to high temperature treatment within a reactor. The oxidised

organic compounds are carried by a flowing inert gas (helium) to a column (kept at high temperature) and packed with a copper reducer and oxidising catalyst, WO_3. The oxidising catalyst within the column helps to further oxide partially oxidized compounds. All CHN analyses were done at the School of chemistry, analytical chemistry laboratory.

3.4. Catalyst reducibility studies

3.4.1. Temperature programmed reduction (TPR)

Metal catalysts are usually supported so as to enhance their surface areas. In their precursor state, the metal oxide, the reducibility of the catalysts are quantitatively studied using temperature programmed reduction (TPR), following the process below.

$$M_X O_Y + yH_2 \rightarrow xM + yH_2O$$

The catalyst precursors are usually reduced in a hydrogen environment in the presence of an inert gas such as argon or nitrogen at a programmed heating rate from room temperature to 900 °C. A thermal conductivity detector is used to measure the changes in thermal conductivity as the catalysts is reduced.

For this study, the Micromeritics AutoChem II shown in Figure 3.11, was used to study the catalyst reduction. Briefly, an oxidized catalyst sample (100 mg) was place in a U-tube and degassed for 1 hour at 150 °C in helium gas then allowed to cool to 50 °C. Following that, the catalyst was reduced in 5 % H_2 and 95 % Ar (45 mL/min) from 50 °C and 900 °C (10 °C/min).



Figure 3.11 The Micromeritics AutoChem II.

3.4.2. In situ powder X-ray diffraction (in situ PXRD)

The reduction process of catalysts at high temperatures can be qualitatively studied using in situ PXRD. In this sudy, the reduction studies were carried out in an Anton-Paar XRK900 furnace under flowing hydrogen atmosphere (High purity, 1 atm). This allowed for the *in situ* monitoring of the reduction behaviour of the catalysts. The XRK900 was attached to a Bruker D8 Advance diffractometer (fig. 3.12) equipped with a Cu Kα X-ray source (40KV, 40 mA); 0.6 mm fixed divergent slit; 2.5 ° primary and secondary beam Söller slits; and a VÅNTEC linear position sensitive detector (LPSD) with an effective angular range of 12° *2θ*. PXRD data was collected every 20 °C in the temperature region from 30 °C to 450 °C.

The samples were prepared using the packing preparation method. Briefly, the sample holder was cleaned using isopropanol and allowed to dry. The catalysts were placed on the holder till full and then the sample was pressed down to obtain a completely flat surface. The sample was then placed inside the analysis chamber. The reducing process was conducted by a flow of hydrogen (50 mL H_2 in 50 mL N_2,) passed at 20 mL/min while ramping the temperature from 30 °C to 450 °C in increments of 50 °C. The experiments were done using a scan range of 2θ = 10° - 90° and a step size of 0.026°. The crystalline phase identification was done using DIFFRAC.EVA (release 2014) using the ICDD PDF2 database (release 2016). Phase quantification was done using the Rietveld method as implemented in Bruker AXS TOPAS software (version 5, 2014). The gases used were of ultra-high purity grade and provided by African Oxygen (AFROX) Ltd.

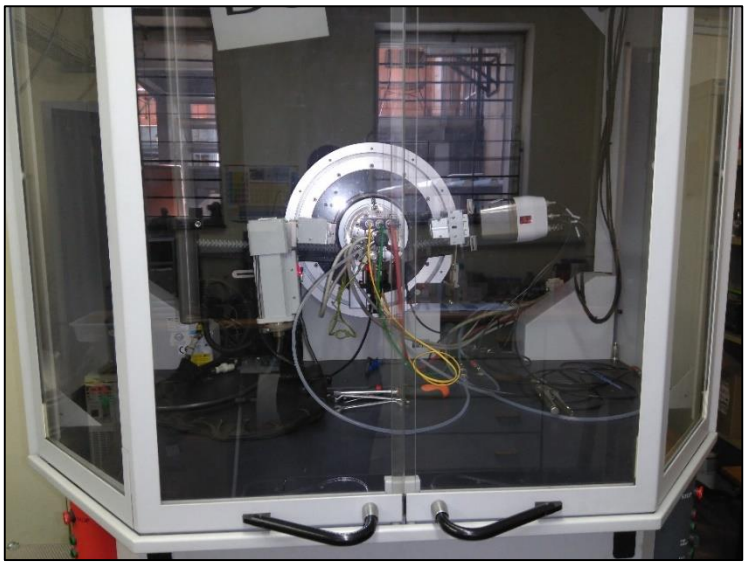


Figure 3.12 A Bruker D8 Advance AXS diffractometer.

3.5. Catalyst testing: reactor set-up and equations

3.5.1. Fischer-Tropsch synthesis reactor set-up

Fischer-Tropsch synthesis (FTS) is a heterogeneous catalytic process where gaseous reactants carbon monoxide and hydrogen (synthesis gas) are carried by nitrogen gas to the surface of a solid catalyst and are catalytically converted to hydrocarbons that are necessary for the productions of fuels and various chemical products.

Represented by figure 3.13, is the schematic rig set up used during the Fischer-Tropsch synthesis (FTS). The main components of this set up are the fixed bed reactor, pressure regulators, thermocouples, cold and hot traps, flow meters and detectors.

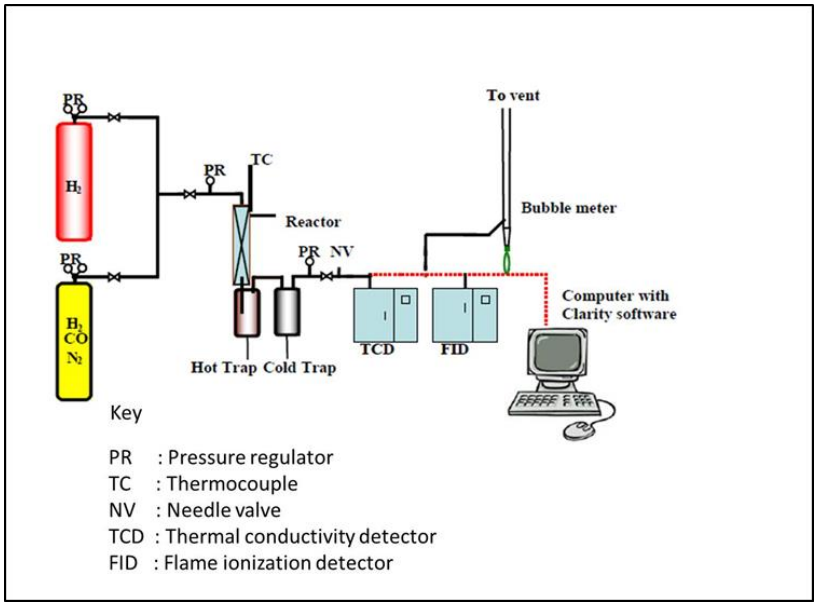


Figure 3.13 A schematic illustration of the rig reactor design. [24]

During the catalytic synthesis, a tubular fixed bed reactor, made of stainless steel, was used. The dimensions of reactor were 250 mm height and 16 mm inner diameter. Additionally the reactor was internally fitted with 2 mm steel balls and externally covered with fibre-glass. The steel balls and fibre-glass assisted in maintaining the programmed temperature during reduction and catalytic synthesis. A soap bubble flow meter was used to measure the flow rate of the gases. The reactor lines were kept hot, at 150 °C, so as to avoid any blockage during FTS. The pressure regulators and thermocouple respectively regulated and monitored the pressure and temperature during synthesis. The online gas chromatograph (GC) detectors, thermal conductivity detector (TCD) and flame ionization detector (FID), were used to detect the products. The GC-TCD was fitted with a Carboxen-1000 60-80 mesh packed column and

successfully detected N_2 gas, CH_4, CO_2 and unreacted syngas. The hydrocarbons which have low boiling points (cannot be condensed) were detected using the online GC-FID fitted with a Porapak Q packed column. The condensable heavy hydrocarbon, waxes and oil fractions, were respectively collected form the hot (130 °C) and cold (25 °C) traps. These products were further analysed on the offline GC-FID. Briefly, a small amount of samples (0.2 μL) was injected into the detector using a micro syringe. The data obtained during synthesis was captured using the Clarity software package.

3.5.2. Catalytic experiments

The experimental catalytic evaluations of the catalysts were conducted using a fixed bed low temperature FTS reactor, by initially reducing of the catalysts followed by reaction with reactants (syngas). Briefly, 0.5 g of calcined catalyst was placed inside the fixed bed reactor and was reduced in-situ at 350 °C under a constant flow of H_2 gas (45 mL/min, 5 bar, 18 hours). Subsequently, syngas was introduced (10 bar; 20 mL/min) and the temperature was gradually increased from room temperature to the FTS temperatures (220 °C and 240 °C). The maximum reaction time at each temperature was 50 hours.

3.5.3. Instrument calibration and product analysis

Prior to stating the catalyst testing, the system was pressure tested as to check for leakages. Briefly, the inert gas N_2 gas opened, set to a pressure of 4 bar and was allowed to flow for 12 hours. N_2 gas is unreactive under FTS conditions and hence was used as an internal standard as to give accurate mass balance calculations.

Two successive methods were used to check for leakages, that is using soapy water and pressure testing. Firstly, soapy water was sprayed on the connecter knobs found along the gas lines. The presence of a gas leak resulted in the formation of soapy bubbles around the knobs. To correct the leak, knobs were tightened using spanners. Secondly, the pressure gauge of the gas line was monitored. A leakage in the system would result in the decrease in pressure. To rectify this decrease in pressure, the gas line knobs were tightened.

The mass balance calculation was performed on the carbon content under steady state conditions for about 50 hours. The reaction reached steady state activity after approximately 15-20 hours. The resulting products analysis was divided in two parts. The gaseous products

were analyzed using the online gas chromatographs, while the heavy oil and wax were analyzed using the offline GC. The online thermal conductivity detector was applied for analysing gaseous compound such as CH_4, H_2, N_2 CO and CO_2, while the online flame ionization detector was used for detection of the hydrocarbons (C_1 - Cx). Prior to the start of reaction and analysis of the products the online GCs were calibrated using a gas mixture with components of known concentrations. The gas mixture used contained CO (10%), CO_2 (5%), CH_4 (2.5%), C_2H_4 (0.2%) and C_2H_6 (0.5%) in an argon balance. Synthesis gas (30% CO, 10% N_2 and H_2 balance) was also applied as a calibrant to calculate the number of moles of the reactants entering the reactor via the gas inlet feed stream. All the gases were of ultra-high purity grade and provided by African Oxygen (AFROX) Ltd. Gas traces produced from the calibration gases were recorded and plotted using a DataApex Chromatograph software package known as Clarity.

The products in the traps were collected separately then weighed and analyzed using the offline GC. The analysis was performed by injecting 0.2 μL into the offline gas chromatograph.

A typical chromatograph recorded by the detectors (FID and TCD) are shown in the figures (3.14 - 3.16) below. The areas under the peaks were attributed to the number of moles of each product in the stream. The FTS reaction conditions are also tabulated below (Tables 3.1-3.3). The calculations used where similar to those used by Dlamini. [24]

The outlet gas flow rate (Fout) of the gas stream was measured everyday using a bubble meter. And used to calculate the inlet gas flow (Fin). Since the total mass flow in and out of the reactor is equal, the internal standard N_2 was used as an inert tracer during the FTS reaction. The total molar inlet gas flow was expressed in relation to the total molar outlet gas flow as:

$$F_{in} = \frac{N_{2,in}}{N_{2,out}} X\, F_{out}$$

Where, N_2,*in* is the calibration peak area for N_2, $N_{2,out}$ is the peak area for N_2 during FT synthesis and F_{out} is the flow rate of the exit stream

The molar percentage of any gaseous component $N_{C,\,out}$ in the outlet stream was calculated based on the integrated peak areas of the component gases obtained using the Clarity software as:

$$N_{C,out} = \left[\frac{A_C}{A_{C,cal}}\right] . X_{C,cal.}\, F_{out}.t$$

Where, A_C is the integrated peak area for component C, $A_{C,cal}$ is the peak area for component C in the calibration gas, $X_{C,cal}$ is the mole fraction of component C in the calibration gas, F_{out} is the flow rate of the exit stream and t is the overall mass balance time.

The fraction of carbon monoxide that was converted to hydrocarbons was calculated using data recorded on the TCD, and was expressed as a percentage as:

$$\%CO = \left[\frac{N_{CO,in} - N_{CO,out}\, X\, \frac{N_{2,in}}{N_{2,out}}}{N_{CO,in}}\right] X100$$

Where, $CO_{,in}$ is the calibration peak area for CO , $N_{2,in}$ is the calibration peak area for N_2, $CO_{,out}$ is the peak area for CO during FTS, and $N_{2,out}$ is the peak area for N_2 during FTS.

The rate of CO conversion (mol/min/gcat) can be computed as:

$$R_{CO} = \left[\frac{F_{CO,in} - F_{CO,out}}{M_{cat}}\right]$$

Where, FCO,in and FCO,out are the molar flow rates (mol/min) of CO fed into the reactor and exiting the reactor, respectively.

From the carbon balance calculations, the product selectivity of individual hydrocarbon was calculated as follows:

$$\%\, S_{i=}\left[\frac{N_i}{r_{CO}.t}\right] X\ 100$$

Where, N_i is the number of moles of hydrocarbon containing i carbon atoms, r_{CO} is the rate of CO conversion and t is the overall mass balance time.

The olefin to paraffin ratio was calculated as:

$$R_{C_x} = \frac{C_x^{=}}{C_x^{-}}$$

Where, R_{Cx} is the olefin to paraffin ratio, $C_x^{=}$ is the number of carbon moles for the olefin containing x carbon atoms and C_x^{-} is the number of carbon moles for a paraffin containing x carbon atom.

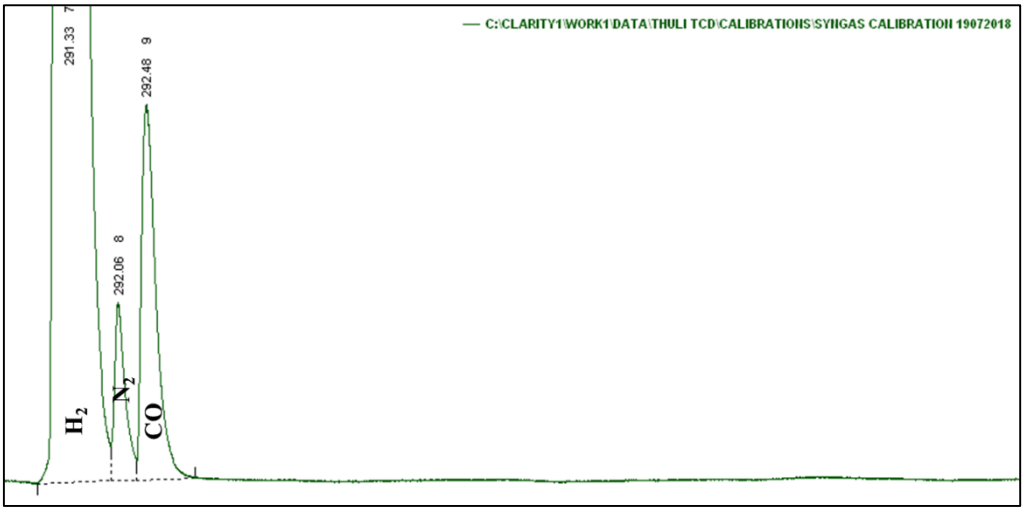


Figure 3.14 A GC-TCD trace recorded during syngas calibration.

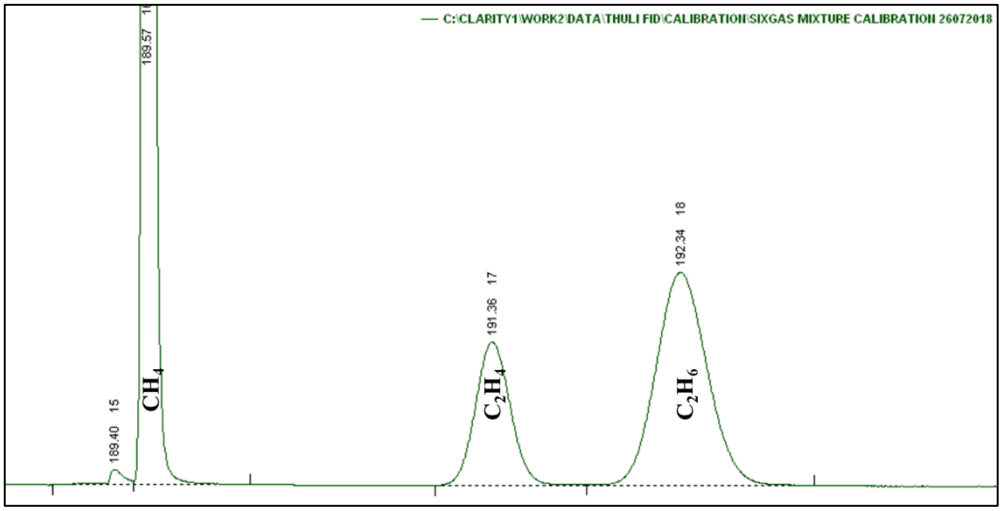


Figure 3.15 A GC-FID trace recorded during six gas mixture calibration.

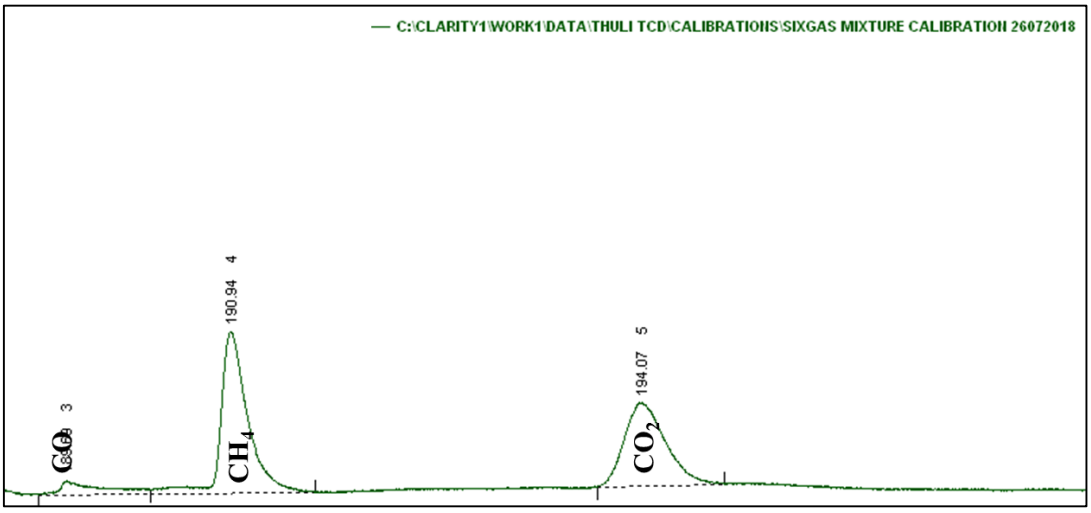


Figure 3.16 A GC-TCD trace recorded during six gas mixture calibration.

3.5.4. Fischer-Tropsch synthesis conditions

Before carrying out FTS, the amount of syngas in the inlet stream was determined as outlined in the **section 3.5.3**. During FTS the non-condensable amounts of un-reacted syngas and the low boiling FT products from the outlet stream were analysed. After FTS the condensable oil fraction and wax fraction were analysed off-line.

Table 3.1 The GC operating conditions during synthesis. [24]

	Online gas chromatogram	Online gas chromatogram	Offline gas chromatogram
Detector	Thermal conductivity detector (TCD)	Flame ionization detector (FID)	Flame ionization detector (FID)
Column type	Packed, stainless steel, 2m x 2.2mm, O.D = 1/8"	Packed, stainless steel, 1.5 m x 2.2 mm, O.D = 1/8"	30 m x 5 µFT, O.D.= 0.53 mm
Stationary phase	Carboxen-1000, 60-80 mesh	Porapack q, 80/100 mesh	ZB-1
Model type	PYE Unicam (Series 204)	Hewlett Packard 5890	Varian 3700
Detector temperature	220 ℃	220 ℃	220 ℃
Carrier gas	Argon	Nitrogen	Nitrogen

3.5.5. Mass balance equations: catalyst activity and selectivity

Table 3.2 The equations used in the FTS calculations

	Equation	Description
1	$\%CO = \left[\frac{N_{CO,in} - N_{CO,out}\, X\, \frac{N_{2,in}}{N_{2,out}}}{N_{CO,in}}\right] X100$	CO conversion
Where, $CO_{,in}$ is the calibration peak area for CO , $N_{2,in}$ is the calibration peak area for N_2 $CO_{,out}$ is the peak area for CO during FT synthesis, and $N_{2,out}$ is the peak area for N_2 during FT synthesis.		
2	$N_{C,in} = F_{in}.t.\ X\ CO_{in}$	number of moles of carbon in the feed stream
Where, F_{in} is flow rate **of** the total feed , t is the overall mass balance time and $CO_{,in}$ is the calibration peak area for CO.		
3	$F_{in} = \frac{N_{2,in}}{N_{2,out}} X\ F_{out}$	The inlet feed flow rate to the reactor
Where, N_2,in is the calibration peak area for N_2, $N_{2,out}$ is the peak area for N_2 during FT synthesis and F_{out} is the flow rate of the exit stream		
4	$N_{C,out} = \left[\frac{A_C}{A_{C,cal}}\right].X_{C,cal.}\ F_{out}.t$	Number of moles of all gaseous products
Where, A_C is the integrated peak area for component C, $A_{C,cal}$ is the peak area for component C in the calibration gas, $X_{C,cal}$ is the mole fraction of component C in the calibration gas, F_{out} is the flow rate of the exit stream and t is the overall mass balance time		

Table 3.3 The equations used in the FTS calculations

	Equation	Description
5	$\%\, S_{i=}\left[\frac{N_i}{r_{CO}.t}\right] X\ 100$	Product selectivity
Where N_i is the number of moles of hydrocarbon containing *i* carbon atoms, r_{CO} is the rate of CO conversion and t is the overall mass balance time.		
6	$r_{FTS} = r_{CO} - r_{CO_2}$	Reaction rate
Where, r_{CO} is the rate of CO conversion and r_{CO2} is the rate of CO_2 production.		
7	$r_{WGS} = r_{CO_2}$	Rate of the water gas shift reation
Where r_{CO2} is the rate of CO_2 production		
8	$\frac{n_i^{=}}{n_i^{=} + n_i^{-}}$	Alkene to alkane ratio
Where $n^{=}_i$ is the moles of alkenes containing i carbon atoms and n^{-}_i is the moles of alkanes containing i carbon atoms.		

3.6. References

1. Thomas, A.; Goettmann, F.; Antonietti, M. *Chemistry of Materials* **2008**, *20* (3), 738–755.
2. Kubo, S.; Demir-Cakan, R.; Zhao, L.; White, R. J.; Titirici, M. M. *ChemSusChem* **2010**, *3* (2), 188–194.
3. Xie, Y.; Kocaefe, D.; Chen, C.; Kocaefe, Y. *Journal of Nanomaterials* **2016**, *1*, 1–11.
4. Li, S.; Pasc, A.; Fierro, V.; Celzard, A. *Journal of Materials Chemistry A* **2016**, *4*

(33), 12686–12713.

5. Parkhomchuk, E. V.; Semeykina, V. S.; Sashkina, K. A.; Okunev, A. G.; Lysikov, A. I.; Parmon, V. N. *Topics in Catalysis* **2017**, *60* (1–2), 178–189.
6. Liang, C.; Li, Z.; Dai, S. *Angewandte Chemie - International Edition* **2008**, *47* (20), 3696–3717.
7. Wang, Y.; Chang, B.; Guan, D.; Dong, X. *Journal of Solid State Electrochemistry* **2015**, *19* (6), 1783–1791.
8. Wu, Z.; Webley, P. A.; Zhao, D. *Journal of Materials Chemistry* **2012**, *22* (22), 11379–11389.
9. Alex, P.; Majumdar, S.; Kishor, J.; Sharma, I. G. *Materials Sciences and Applications* **2011**, *2* (9), 1307–1312.
10. Toebes, M. L.; Van Der Lee, M. K.; Tang, L. M.; In 'T Veld, M. H. H.; Bitter, J. H.; Van Dillen, A. J.; De Jong, K. P. *Journal of Physical Chemistry B* **2004**, *108* (31), 11611–11619.
11. Levine, I. N. *Physical chemistry*, 6th edition **2009**, New York: McGraw-Hill Companies, Inc.
12. **http://wwwoutreach.phy.cam.ac.uk/camphy/xraydiffraction/xraydiffraction_exp.htm.** 13/09/2018. Braggs law demonstration.
13. Brunauer, S.; Emmett, P. H.; Teller, E. *Journal of the American Chemical Society* **1938**, *60* (2), 309–319.
14. Ferrari, A. C.; Basko, D. M. *Nature Nanotechnology* **2013**, *8* (4), 235–246.
15. Ferrari, A. C.; Robertson, J. *Phys. Rev. B* **2000**, *61* (20), 14095–14107.
16. Williams D. B.; Carter, C. B. *Transmission electron microscope: A textbook for material science* **1996**, Springer.
17. http:/warwick.ac.uk/fac/sci/physics/current/postgraduate/regs/mpagswarwick/ex5/techniques/structural/tem/ **10/09/2018**.
18. Qureishy, T. *Synthesis and structural studies of* $Mg_2Si_{1-x}Sn_x$ **2012**. University of Oslo, Department of Physics.
19. Bagus, P. S.; Ilton, E.; Nelin, C. J. *Catalysis Letters* **2018**, *148* (7), 1785–1802.
20. Fuggle, J. C.; Burr, A. F.; Watson, L. M.; Fabian, D. J.; Lang, W. *Journal of Physics C: Solid State Physics* **1974**, *4* (2), 335–342.
21. Leofanti, G.; Padovan, M.; Tozzola, G.; Venturelli, B. *Catalysis Today* **1998**, *41* (1–3), 207–219.

22. Titantah, J. T.; Lamoen, D. *Diamond and Related Materials* **2007**, *16* (3), 581–588.
23. Fadeeva, V. P.; Tikhova, V. D.; Nikulicheva, O. N. *Journal of Analytical Chemistry* **2008**, *63* (11), 1094–1106.
24. M. W. Dlamini, *Spherical carbons as model supports for Fe, Co and Fe-Co Fischer-Tropsch catalysts* **2016**, PhD thesis, University of the Witwatersrand, Johannesburg.

CHAPTER 4

The study and characterization of cobalt and ruthenium nanoparticles encapsulated in N-doped hollow carbon spheres: evaluation of N-doped HCSs as a hydrogen transport layer and as a nanoreactor

4.1. The evaluation of N-doped HCSs as a support for Co and Ru nanoparticles

4.1.1. Introduction

Carbon, along with its allotropes, is an important element in material science due to its properties and potential applications. Carbon nanomaterials with different shapes and sizes have been widely explored in catalysis research as catalyst supports for Co catalysts.[1-4] The success of a carbon nanomaterial as a Co catalyst support is attributed to its physiochemical properties (high surface area; porosity; graphitic nature; good electrical conductivity and chemical inertness). These properties allow for a high dispersion of the active catalytic phase (Co), a minimum active phase-support interaction and thus a high catalytic activity to be achieved.

New generation carbon nanoreactors e.g. hollow carbon spheres (HCSs) are a promising type of carbon support. The HCSs have a specific spherical structure that is composed of a hollow core that is surrounded by a porous shell as shown in fig.1. [5] The hollow core of the HCSs facilitates encapsulation and stabilization of metal nanoparticles such as Co. [6] The HCSs structure can control the amount of metal, such as Co, contained inside the HCSs and also the particle size of the Co metal, thus improving the Co dispersion. The porous shell assists in facilitating mass transfer of reactants and products to and from the metal active sites during reactions.



Figure 4.1 Structure of a hollow carbon sphere with a porous shell. [7]

The principal synthesis method used to make HCSs is the hard templating method. The templating method is commonly achieved using chemical vapour deposition or hydrothermal synthesis proceedures.[8] The conditions of the synthesis techniques (temperature; time; gas flow rate etc.) determine the chemical nature of the resultant HCSs. Polystyrene is a hard template that has been found attractive in material science during the templating synthesis of HCSs. [9, 10] This is because the polystyrene template is easy to synthesize, has a narrow size distribution and easy to decompose thermally at 400 °C, and can be removed by dissolving in N, N-dimethylformamide.[7, 9]

HCSs have been reported to be good model supports for Co catalysts and for studying the reducibility of promoted Co catalysts. Dispersed Co nanoparticles with a limited metal-support interaction are obtained when HCSs are used as supports, as a result of their high surface area and inertness. Additionally, the sintering of nanoparticles is limited because nanoparticles encapsulated within a hollow core in a particular sphere cannot sinter with other nanoparticles that are on the outside of the HCS or inside other spheres. The morphological structure of HCSs allows for effective hydrogen spillover studies for promoted Co catalysts, through the ability to vary the contact between the promoter and Co catalyst.

As mentioned above, the surface of carbon supports is relatively chemically inert, and may require chemical surface functionalization. One commonly used method of functionalizing the surface of a carbon support is by nitrogen doping. This can be achieved by either in-situ doping or by post doping. Nitrogen doping incorporates N within the carbon matrix thus resulting in the formation of nitrogen containing functionalities (pyrollic-N, pyridinic-N, quartnery-N oxidized-N) [11] The nitrogen containing functional groups are known to increases the electronic conductivity of the carbon support, to reduce the graphitic nature

(hydrophobicity) of the carbon support and to give better anchoring of the supported metal nanoparticles, such as Co.

Many studies have already been done on the use of HCSs as a support and as a nanoreactor, however there has been no report on the use of N-doped hollow carbon spheres as nanoreactors. Herein, we report on a study of N-doped nanoreactors prepared by varying the annealing time and type of nitrogen doping process (in-situ and post doping). These nanoreactors were used to study the effect of cobalt metal reducibility by hydrogen.

4.1.2. Methodology

Carbonaceous spheres with spherical and hollow morphology were synthesized using the hard templating technique. The hard templating technique is comprised of three main steps, namely, (i) synthesis of the template, (ii) shell formation of the desired material on the template surface i.e. loading metal catalyst and/or coating with carbon source around the template and (iii) template decomposition. The process is schematically showed on figure 4.2. Polystyrene spheres, resorcinol-formaldehyde, melamine and hydrated metal salts ($Co(NO_3)_2.6H_2O$ and $RuCl_3.H_2O$) were used as the spherical hard template, carbon precursor, the nitrogen precursor and metal precursors, respectively. Subsequently, the metal loaded template was coated with the carbon precursor followed by coating with the nitrogen precursor. The obtained composite was carbonized to decompose the template, anneal the carbon matrix and incorporate nitrogen atoms within the carbon matrix. After carbonization, nitrogen-doped hollow carbon spheres with metal nanoparticles encapsulated within the hollow core were obtained (e.g. Co@NHCS catalyst). The Ru nanoparticles were then supported outside of the Co@NHCS thus giving the Co@NHCS@Ru catalyst. The catalysts were calcined at 210 °C for 2 hours under a flow of 5% O_2/bal Ar (50mL/min) gas mixture. The detailed synthesis process is described in section 3.2.

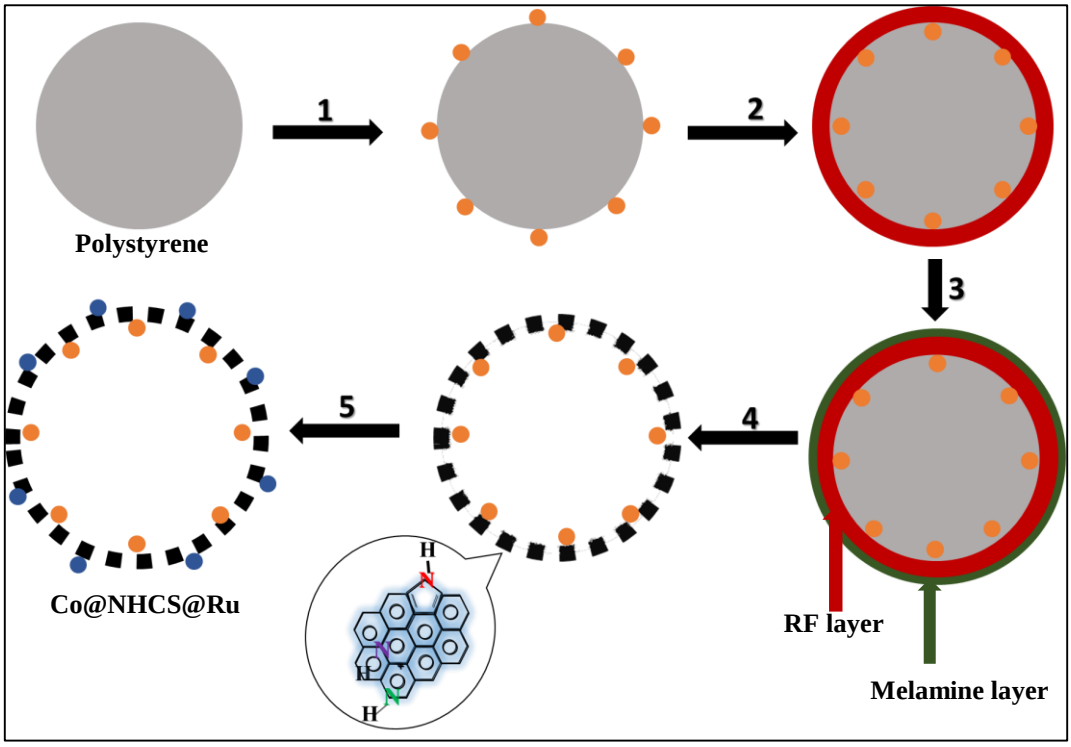


Figure 4.2 Schematic representation of the synthesis methodology. **(1)** metal (Ru and Co) onto a polystyrene template; **(2)** resorcinol-formaldehyde (carbon precursor) coating; **(3)** melamine (nitrogen precursor) coating, **(4)** template decomposition and annealing and **(5)** Ru metal loaded onto the carbon support.

4.1.3. Characterization.

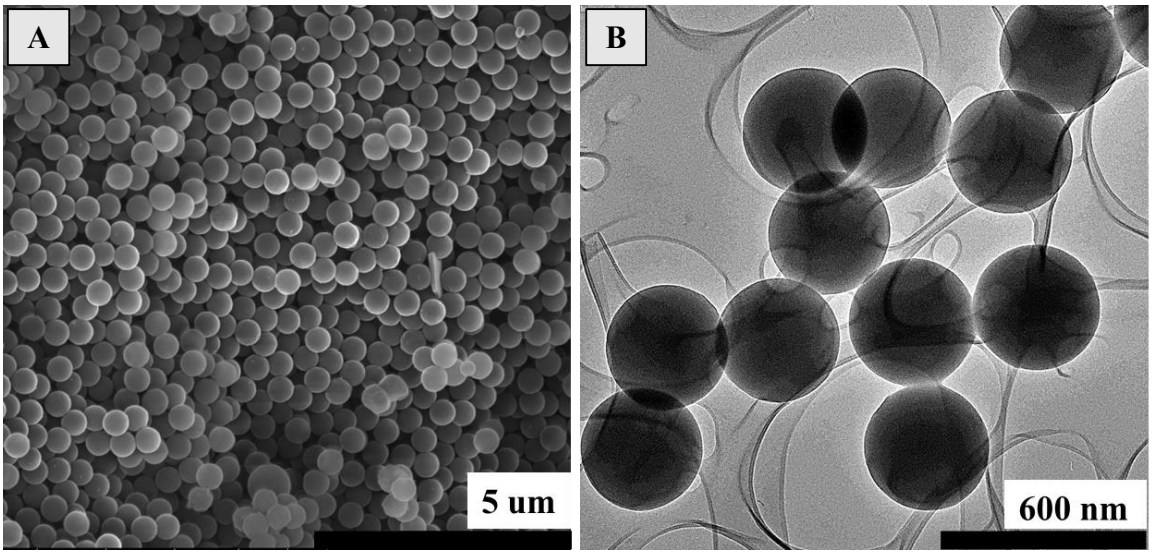
Several analytical techniques were employed to evaluate the chemical and physical properties of the polystyrene template, NHCSs and calcined catalysts. Detailed explanations of the characterization techniques and sample preparation methods used are provided in chapter 3. Briefly, transmission electron microscopy (TEM) was used to determine the features of the internal morphology and scanning electron microscopy (SEM) was used to evaluate the external morphology of the materials; Laser Raman spectroscopy (LRS) was used to establish the graphitic nature of the carbon support; Brunauer–Emmett–Teller (BET) analysis was used to facilitate the surface area and pore volume measurements, powder X-ray diffraction (PXRD) was used to establish the crystallographic planes of the metals; thermo gravimetric analysis (TGA) to establish the thermal stability and metal loadings of the catalysts; X-ray photoelectron spectroscopy (XPS) was used to determine the bonding configurations within the carbon support and CHNS elemental analysis was used for the determination of light

elements. The reducibility of the catalysts was assessed using the in situ powder X-ray diffraction (in situ PXRD) and temperature programmed reduction (TPR) techniques.

4.1.4. Results and discussion

4.1.4.1. Structural analysis of the polystyrene template

Designing carbon nanoreactors with porous shells is a stepwise templating process that involves, namely:- the synthesis of the template, the formation of the template and carbon precursor composite and the removal of the template.[13] Polystyrene is the template that was used in this study to synthesize nitrogen doped hollow carbon spheres (NHCSs). The templating process is highly dependent on the success of the synthesis of the template. Hence prior to templating, the template needs to be characterized. Polystyrene spheres were prepared by a polymerization reaction, using styrene as a monomer.[12] Monodispersed polystyrene spheres were obtained with spherical and solid morphology as shown by the SEM and TEM images (fig. 4.3A and fig. 4.3B). The particle size distribution (PSD) of the polystyrene spheres showed that the polystyrene spheres had an average diameter of 310 ±25 nm (insert in fig. 4.3A). The PRXD pattern (fig. 4.3C) confirmed the presence of amorphous carbon with the 002 plane centred at 2θ value of 22.2 °. Figure 4.3D, represents the TGA pattern and the DTGA pattern of the polystyrene spheres. The sphere thermally degrade at 400 °C. Similar results for polystyrene spheres have been obtained in related literature studies. [13, 14]



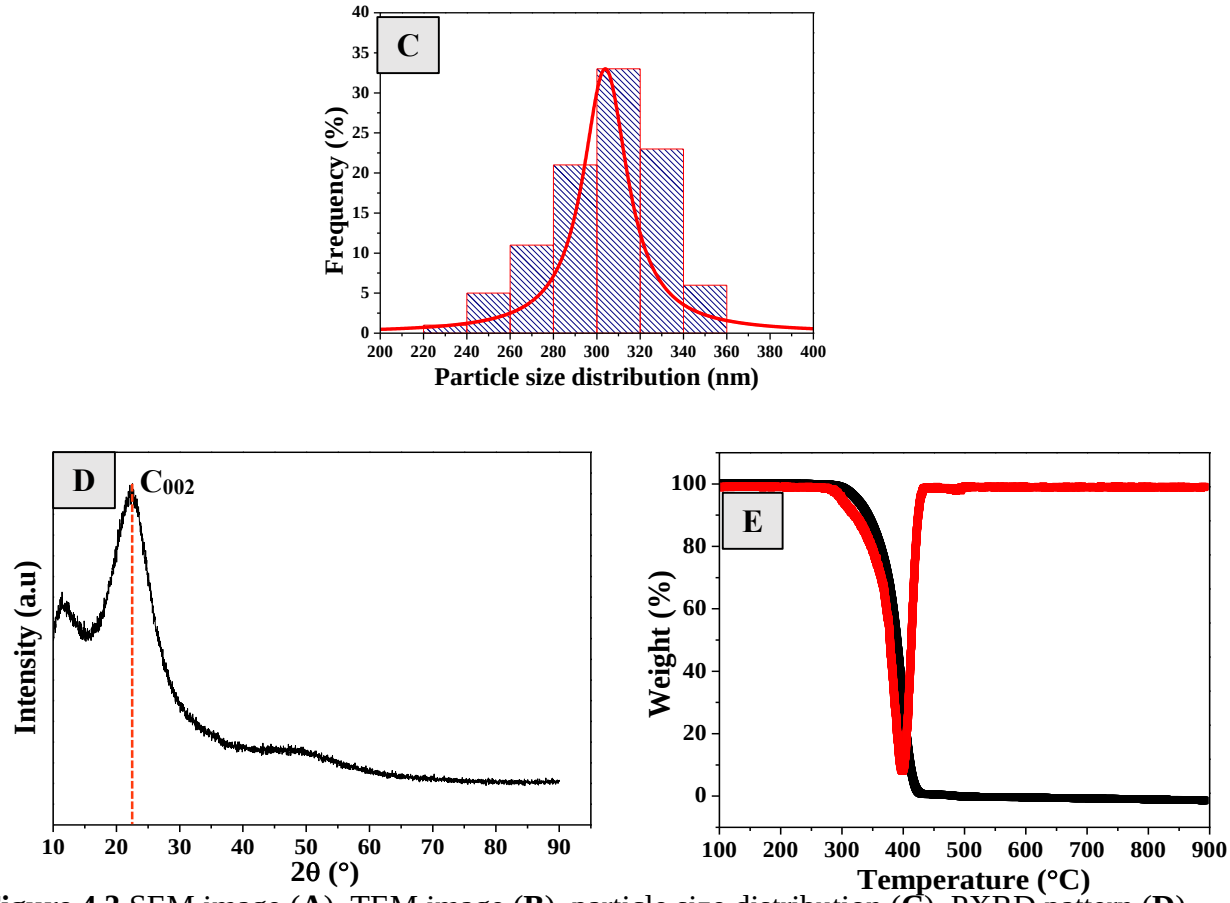


Figure 4.3 SEM image (**A**), TEM image (**B**), particle size distribution (**C**), PXRD pattern (**D**) and TGA with DTG (**E**) for polystyrene spheres.

4.1.4.2. N-doped hollow carbon spheres

SEM and TEM analysis of NHCSs

To synthesize nitrogen doped hollow carbon spheres (NHCSs), the pristine polystyrene sphere template (PSS) was coated with a carbon precursor and followed by a nitrogen precursor and the composite PSS@RF-melamine was obtained. This composite was then subjected to heat treatment under an inert environment to anneal the carbon shell, incorporate nitrogen and decompose the template. The resulting NHCSs maintained a spherical morphology of the template (fig. 4.4A and fig. 4.4B), with the majority of the spheres not broken (< 5 %). The hollow spheres had a diameter of 380 ±20 nm and a shell thickness of 40 ±15 nm. This is shown by the TEM image (fig. 4.4A). Furthermore, the SEM image (Fig.4.4B) of a broken sphere confirms the hollow morphology of the spheres and confirms

the complete decomposition of the polystyrene template thus, leaving a void/hollow space inside a sphere.[15]

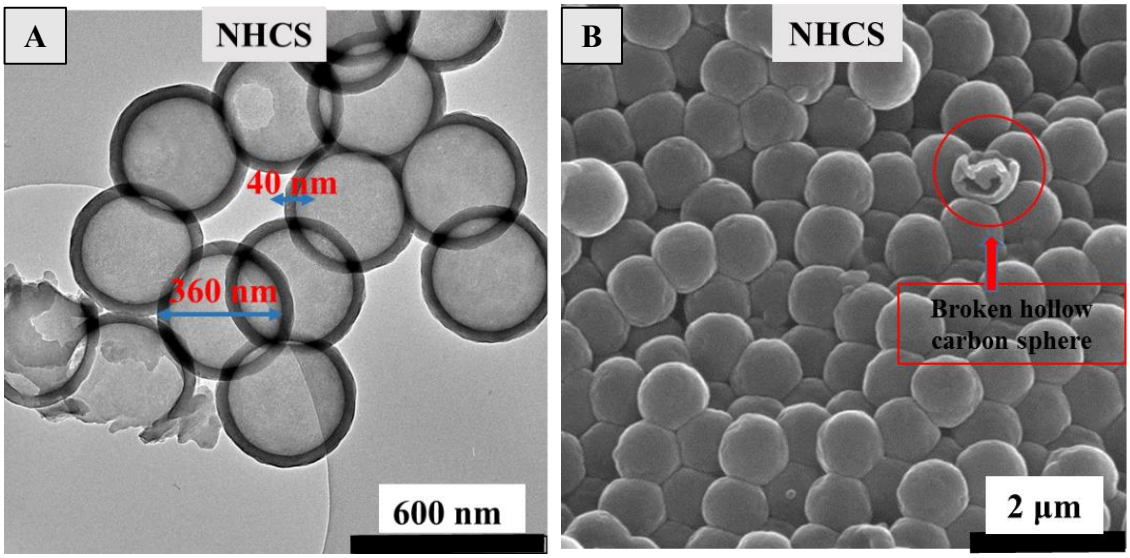


Figure 4.4 TEM (**A**) and SEM (**B**) image of N-doped hollow carbon spheres (NHCSs).

TEM analysis of catalysts

The synthesis of catalysts (metal encapsulated in NHCSs) were synthesized similarly to the method used to make the pristine NHCSs, as explained above. The only difference was that metal was loaded on the polystyrene spheres (PSS/Co and PSS/Co-Ru) prior to coverage by a carbon layer and a melamine layer. TEM analysis was used to evaluate the new products. The spheres were spherical and with most of the spheres not broken in comparison to those without metals inside (fig. 4.4). This observation suggests that the metal aids in catalysing the formation of the carbon spheres from resorcinol-formaldehyde.[7] The SEM images of the catalysts and corresponding EDX spectra, which confirms the presence of Co and Ru metals, are provided in the supplementary information (fig. 4S.1).

Loading of Ru metal on the Co@NHCS catalyst was done using the wetness impregnation method. The theoretical metal loading was calculated to be 10 % of Co and 0.5 % of Ru. TEM images (fig. 4.5) show good dispersion with narrow particle size distribution of the metal nanoparticle encapsulated inside the NHCSs. The particle size distribution of the catalysts were found to be 6.0 ±1.5 nm for the Co@NHCS and 6.2 ±1.5 nm for Co@NHCS@Ru catalyst.

The Co-Ru@NHCS catalyst showed an average particle size of 4.5 ±0.8 nm. The decrease in particle size of the nanoparticles in the bimetallic catalyst (Co-Ru@NHCS) can be attributed to the additional nucleation sites for nanoparticle growth provided by the Ru metal. A similar observation have been reported by other authors. [16, 17]

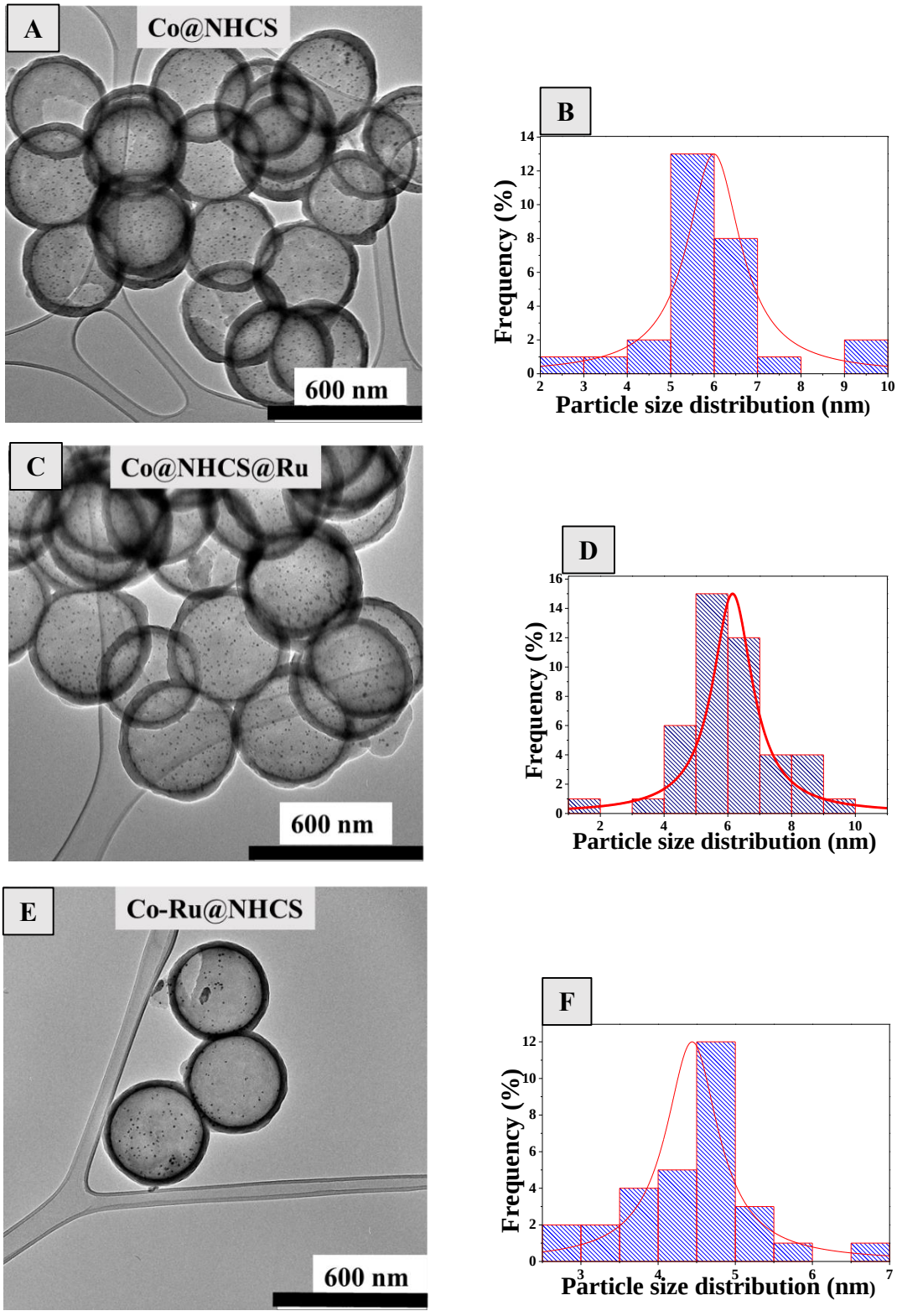


Figure 4.5 TEM images with respective particle size distributions of the catalysts, (**A** and **B**) 10% Co@NHCS; (**C** and **D**) 10% Co@NHCS@Ru; (**E** and **F**) 10% Co-Ru@NHCS.

PXRD and TGA analysis of the catalyst support and catalysts

The PXRD patterns of catalysts (Co@NHCS, Co@NHCS@Ru and Co-Ru@NHCS) the calcined in O_2 /Ar are shown in fig. 4.6A. Additionally, the PXRD pattern for nitrogen doped carbon support (NHCS) is shown as a reference. The NHCS support shows two broad diffraction peaks at 2θ values of 22.2 ° and 44.3 °. These diffraction peaks can be attributed to 002 and 004 reflections of amorphous carbon. [18]

The supported catalysts (Co@NHCS, Co@NHCS@Ru and Co-Ru@NHCS) also show a noticeably broad XRD peak at 2θ value of 22.2 °. This peak is attributed to the 002 reflection of amorphous carbon. The amorphous nature of the carbon can also be attributed to the presence of defects e.g. nitrogen.[19] The supported catalysts show the presence of cobalt oxide by the 2θ values of 35° and 45°. [2] The broadness of these peaks confirm that the particle sizes of the metals are in the nanometer range, thus agreeing with the observation from the TEM analysis. Using the full width at half maximum (FWHM) of the Co_3O_4 peaks, the size of the Co_3O_4 nanoparticles was estimated using the Scherrer equation (table 4.1; eq. 4S.1). These were 7.3 nm (Co@NHCS), 8.1 nm (Co@NHCS@Ru) and 5.5 nm (Co-Ru@NHCS). There were no diffraction peaks for Ru and this may be attributed to the low loading (0.5 %) and small crystallite sizes of the Ru metal.

The thermal stabilities of the calcined supported Co catalysts and the catalyst support were evaluated using TGA analysis. The observations are shown in fig. 4.6B which shows that the NHCS start decomposing at 468 °C. Addition of Co to the carbon (Co@NHCS, Co@NHCS@Ru and Co-Ru@NHCS catalysts) assisted in catalysing the carbon oxidation hence the carbon oxidation occurred at lower temperatures (308°C - 340°C). This phenomena is shown by the red arrow and the data is summarized in table 4.1. The actual effect can be attributed to the catalytic nature of Co_3O_4 nanoparticles which catalyses early decomposition of the carbon support. [20] The derivative thermographs (fig. 4S.2) of the catalyst support and supported Co catalysts show the temperature at which the majority of the carbon is oxidized. The TGA data showed a residual weight (9 % - 16 %) after the carbon oxidation (also stated in table 4.1). This weight residue corresponds to Co_3O_4 and RuO_2. Using the residual wt %,

the theoretical Co metal loadings were calculated to be 7 % -11 % which is close to the estimated loading of 10 % Co.

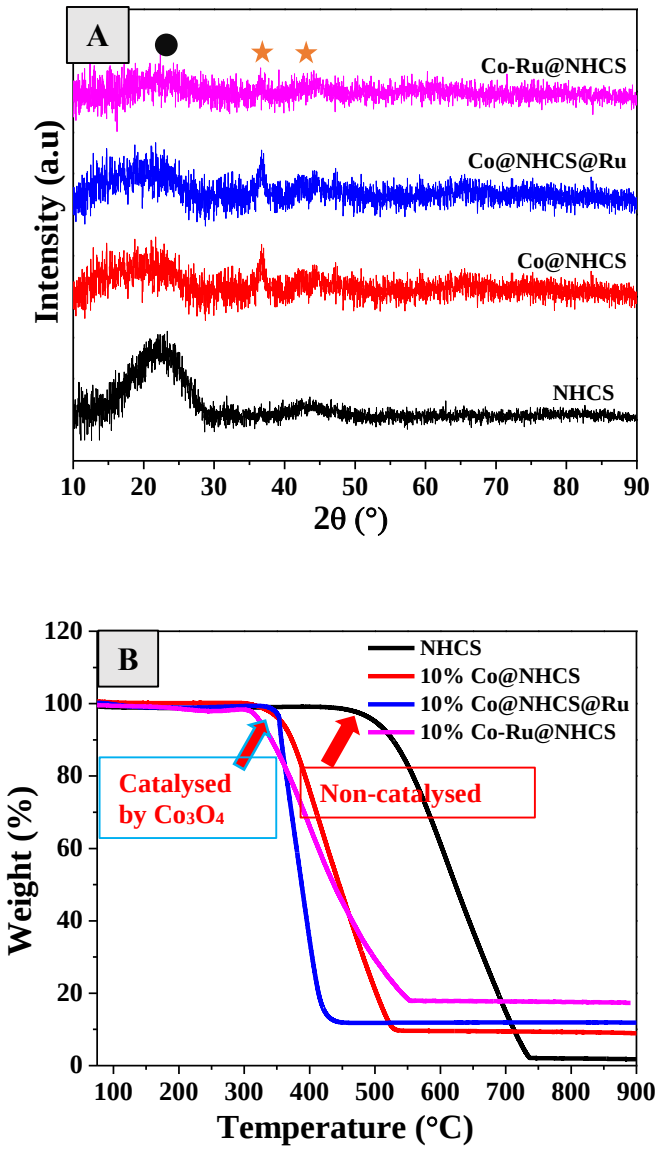


Figure 4.6 PXRD patterns (**A**) and TGA profiles (**B**) of catalysts. Carbon (●); Co_3O_4 (★)

Table 4.1 Decomposition temperature, metal loading and particle size of the catalysts.

Sample	Initial decomposition temperature (°C)	Co_3O_4 wt % (TGA)	Particle size (nm)	
			TEM	PXRD[b]
NHCS	468	-	-	-
Co@NHCS	340	9	6.0 ±1.5	7.3
Co@NHCS@Ru	348	12 [a]	6.2 ±1.5	8.1
Co-Ru@NHCS	308	16 [a]	4.5 ±0.8	5.5

[a] metal loading is a combination of Co_3O_4 and RuO_2; [b] particle sizes of Co_3O_4 were estimated using the Scherrer equation.

Raman, CHNS and XPS analysis

Raman spectroscopy (532 nm excitation wavelength), was used to evaluate the graphitic nature of the catalyst carbon supports. The observed Raman spectra are shown in figure 4.7A and the data summarized in table 4.2. Characteristic Raman, G- band and D-band peaks, were observed. The G-peak represents the vibrations of sp^2 hybridized carbon atoms and the D-peak represents the defects in the graphite structure. The intensity ratio of the D-band to the G-band represents the degree of graphitization of the carbon supports. [21] The D-band and G-band for the supported catalysts (Co@NHCS, Co@NHCS@Ru and Co-Ru@NHCS) were observed at 1337 cm^{-1} and 1596 cm^{-1} respectively. The catalyst support, NHCS, shows a slight shift of its D-band peak position towards the higher wavenumbers (marked by the blue line in fig. 4.7A) but without any shift in its G-band peak position. This D-band peak is observed at 1355 cm^{-1} and is noticeably broad. These observations are usually associated with the presence of defects within the carbon matrix. [22-24]

The chemical composition of the nitrogen doped carbon support was analysed using CHNS analysis and XPS analysis. It is noteworthy that CHNS is a bulk analysis technique and XPS is a surface analysis technique. [25] The wide XPS survey spectra of the catalyst support and supported catalysts are shown in fig. 4.7B and fig. 4.7C. The wide XPS survey spectra shows the samples are composed of carbon, nitrogen and oxygen with binding energy of 248 eV, 398 eV and 532 eV respectively. The trend in the binding energy of the elements (C, N and O) correlates to their electronegativity. [26, 27] The Co nanoparticles encapsulated inside the

carbon support were not detected because XPS analysis is a surface technique and penetrates the carbon shell (40 nm) to a maximum depth of 10 nm. [28] Table 4.2 summarizes the chemical composition of the supports. Both the XPS and CHNS analysis techniques showed similar chemical compositions. The nitrogen content on the supported catalysts (Co@NHCS, Co@NHCS@Ru and Co-Ru@NHCS) is ~ 5% whereas on the catalyst support (NHCS) it is ~7%. The higher nitrogen content (more defects) in the NHCS is in agreement with observations of the Raman analysis (shift of the D-peak towards higher wavenumbers) and PXRD analysis (broad carbon peak). The observed ratios are in contrast to these observations, showing that the NHCS which contains the highest nitrogen content, has an I_D/I_G ratio of 0.77 (least amount of defects). This anomaly can readily be attributed to other factors determining this ratio that have been outlined in a study by Ferrari and Robertson [24]. They report that a Raman spectrum is dependent on (i) the configuration of sp^2 hybridized carbons (aromatic or aliphatic), (ii) clustering, (iii) the sp^2:sp^3 ratio and (iv) to a certain extent, on the excitation wavelength. Their study reports that in a Raman spectrum, the G peak is inclusive of all carbons with sp^2 carbon sites and that the intensity of the D peak is dependent on the presence of aromatic rings. In the study it is also stated that the photon energy of a visible excitation (e.g. 532 nm λ radiation) used in visible Raman is enough to excite sp^2 sites only. [24, 29, 30, 31] The supported Co catalysts (Co@NHCS, Co@NHCS@Ru and Co-Ru@NHCS) had analogous Raman spectra and I_D/I_G ratios (0.92 and 0.93) which indicated their similar chemical properties. [29] A similar study shows that the presence of Co can decrease graphitization by raising the amount of defects present. [32]

In this section, a more detailed explanation of the XPS data e.g. N1s spectra are not given but will be discussed in the following section (section 4.2), where their presence and effect is more relevant.

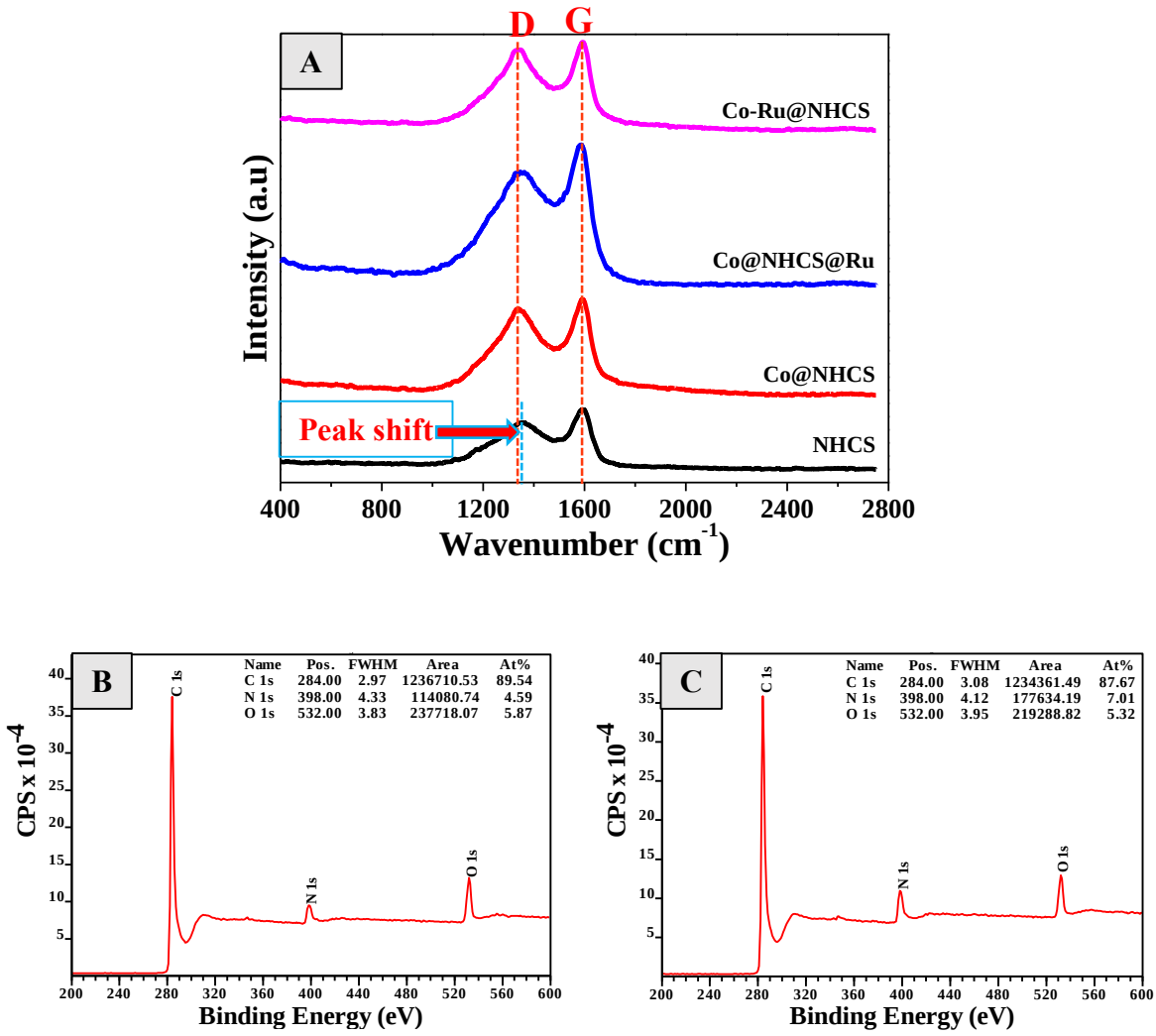


Figure 4.7 Raman spectra of catalysts (**A**) and survey XPS spectra of 10% Co@NHCS (**B**) and survey XPS spectra of NHCS (**C**).

Table 4.2 The nitrogen content and Raman spectroscopy data

Sample	Elemental content: atomic concentration % (XPS)			Elemental content: elemental analysis % (CHNS)		Wavenumber (cm^{-1})		I_D/I_G
	C	N	O	C	N	D-band	G-band	
NHCS	87.76	7.01	5.32	85.37	7.21	1355	1596	0.77
Co@NHCS	89.54	4.59	5.87	87.50	5.06	1337	1596	0.92
Co@NHCS@Ru	-	-	-	88.23	5.55	1337	1595	0.93
Co-Ru@NHCS	-	-	-	86.21	5.13	1337	1596	0.93

BET analysis

The surface area and porosity of the nitrogen doped carbon support (NHCS) and the supported Co catalysts (Co@NHCS, Co@NHCS@Ru and Co-Ru@NHCS) were evaluated using nitrogen physisorption. The observed isotherm and pore size distribution of the NHCS is shown in fig. 4.8A and fig.4.8B, respectively. Similar isotherms and pore size distribution were observed with all the supported catalysts as well the as the catalyst support (fig. 4S.3). The corresponding surface areas, pore volumes and pore sizes of the carbon support and catalysts are summarised in table 4.3. The observed similarity in porosity of the catalysts suggested that the materials had structures with similar pore size. The observed isotherm is a type 4 isotherm and possesses mesopores. A hysteresis loop is observed at 0.6-0.9 P/P_o with the majority of the pores being at 2.50 nm. By using the IUPAC guidelines, the nitrogen doped carbon shell of NHCSs can be classified as mesoporous. [33, 34] The NHCS had the highest surface area of 188 m^2/g.

When the Co nanoparticles were encapsulated inside the NHCS, the surface of the supported catalyst decreased (Co@NHCS = 143 m^2/g). There was a decrease in the surface area when the Ru nanoparticles were loaded on the outside of the catalyst (Co@NHCS@Ru = 129 m^2/g). It was observed that the surface area of the Co-Ru@NHCS catalysts also decreased (102 m^2/g). The observed decrease in surface area could be that (i) bulky nitrogen groups are formed thus blocking the pores because post nitrogen doping process was used to incorporate

the nitrogen within the carbon matrix. It is possible that not all the nitrogen was incorporated within the carbon matrix and some nitrogen may have formed a nitrogen layer around the carbon shell, (ii) Co nanoparticles could be blocking some pores and (iii) may be due to the different metal loadings obtained. [35] More studies will have to be done to confirm these assumptions. However, in summary, these catalysts had a mesoporous carbon shell of diameter 3.3 nm - 4.7 nm.

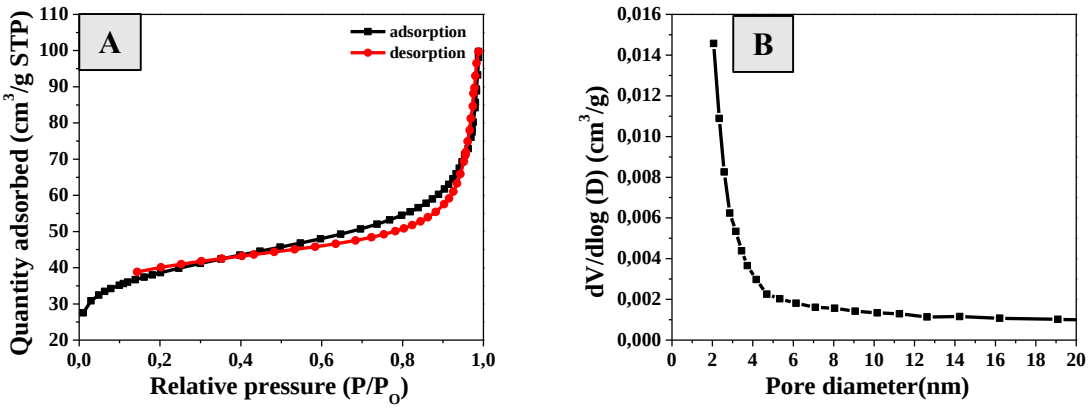


Figure 4.8 N_2 adsorption-desorption isotherm (**A**) and the corresponding adsorption pore size distribution (**B**) for the NHCSs.

Table 4.3 BET surface area, pore size and pore volume data.

Sample	Surface area (m^2/g)	Pore volume (cm^3/g)	Pore size (nm)
NHCS	188 ± 7	0.23	2.5
Co@NHCS	143 ± 4	0.19	4.7
Co@NHCS@Ru	129 ± 3	0.17	4.6
Co-Ru@NHCS	102 ± 6	0.14	3.3

TPR analysis.

Temperature programmed reduction (TPR) was used to assess the reducibility of the Co oxide in a hydrogen environment with increasing temperature, using a NHCSs as a support. The reduction of Co oxide to metallic Co, occurs in two steps, (i) $Co_3O_4 \rightarrow CoO$ and (ii) $CoO \rightarrow Co$. The reduction process may be accelerated by hydrogen spillover. The reduction

temperature of a supported Co catalyst promoted by Ru is dependent on the size of Co nanoparticles, the nature of the support as well as the presence and location of an electronic promoter Ru. This study aimed to investigate the effects of nitrogen defects on the carbon support on hydrogen spillover from Ru to Co oxide. In the presence of Ru, the reduction of Co oxide catalyst is facilitated by hydrogen spillover. Hydrogen spillover can occur by a primary hydrogen spillover event or by a secondary hydrogen spillover event. [36] Primary hydrogen spillover occurs when the Co oxide nanoparticle and the Ru nanoparticle are in close contact whereas secondary hydrogen spillover occurs when the Co oxide nanoparticle and the Ru nanoparticle are separated by a barrier e.g. a carbon support. [37]

The TPR analysis was conducted on catalysts calcined in 5% O_2/Ar because it was necessary to convert all the Co nanoparticles to the Co_3O_4 phase in order to effectively assess the reduction process. The calcination process was carried out on the three catalysts (210 °C, 2 hours). The reduction profiles obtained for the Co catalysts supported on nitrogen doped carbon support (Co@NHCS, Co@NHCS@Ru, Co-Ru@NHCS) are presented in fig. 4.9. The nitrogen doped carbon support (NHCS) was used a reference. The NHCS support shows a single negative peak at 684 °C which is due to the gasification of the carbon support (methanation). [38]

The Co@NHCS catalyst shows two reduction peaks corresponding to hydrogen consumption. The first reduction peak is observed at 271 °C, corresponding to the Co_3O_4 →CoO reduction. A second reduction peak observed at 434 °C corresponds to the CoO →Co reduction.

When the Co and Ru are both placed in the interior of the NHCS and are in close approximity to each other (Co-Ru@NHCS), a single reduction peak is observed at 269 °C. This reduction peak corresponds to the complete two step Co_3O_4→Co reduction and shows the process of primary hydrogen spillover. In a recent study, Phaahlamohlaka studied similar catalysts but using a non-doped mesoporous carbon support (MHCS). [20] The reduction temperatures obtained from the study are shown in table 4.4. In this related study, a similar reduction temperature was obtained when the metals were in close proximity (Co-Ru@MHCS, 264 °C).

When the Ru promoter was added to the surface of NHCS (Co@NHCS@Ru) i.e. the metals are separated by the support, a new peak is observed a lower temperatures 153 °C. This reduction peak can be attributed to the reduction of RuO_2 to Ru. [39, 40] Two other reduction

peaks are observed at 347 °C and 420 °C. This could suggest that the cobalt is present as CoO in two different environments, both affected by the presence of Ru. The peak around 347 °C could be due to the CoO that is in better contact with the nitrogen doped material. Secondary hydrogen spillover can be evoked to explain the downshift of the second peak (420 °C). Thus the presence of Ru metal nanoparticles promoted CoO →Co reduction. This study will need to be repeated as the data obtained do not fit conventional processes.

A comparison of this catalyst with an equivalent catalyst made with no nitrogen on the support has been reported. [20] The non- doped catalyst showed similar reduction temperatures in comparison to those obtained in our study, [Co@MHCS (323 °C, 415 °C); Co@MHCS@Ru (312 °C, 414 °C)]. The similar study showed that secondary hydrogen spillover on the Co@MHCS@Ru catalyst only improved Co_3O_4 →CoO reduction. The effect of particle size on the reducibility of Co_3O_4 nanoparticles [41] can be ruled out as catalysts had similar particle size (~6 nm).

The negative peak of due to the carbon spheres methanation at high temperature (> 600 °C) was also seen for all catalysts supported on nitrogen doped supports and was positioned at similar temperatures.

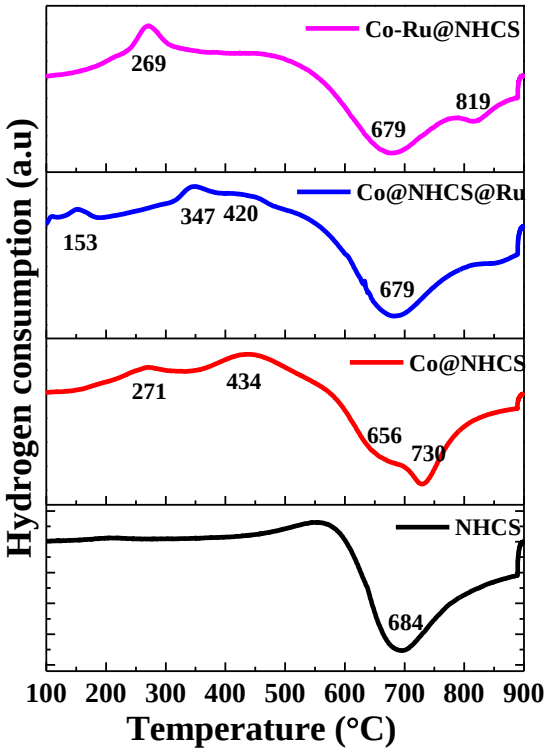


Figure 4.9 TPR reduction profiles for Co catalysts and catalyst support.

Table 4.4 TPR reduction peak positions of catalysts and catalyst support.

Sample	Cobalt oxide reduction temperature (°C)				Methanation temperature (°C)
	$Co_3O_4 \rightarrow CoO$ peak		$CoO \rightarrow Co$ peak		
NHCS	-		-		684
Co@NHCS	271	***323***[a]	434	***415***[b]	656, 730
Co@NHCS@Ru	347	***312***[a]	420	***414***[b]	679
Co-Ru@NHCS	269	***264***[a]	269	***264***[b]	679, 819

[a,b] Reduction temperature obtained from a similar study done using non-doped carbon support.[20]

In situ PXRD analysis: isothermal H_2 reduction at high temperature.

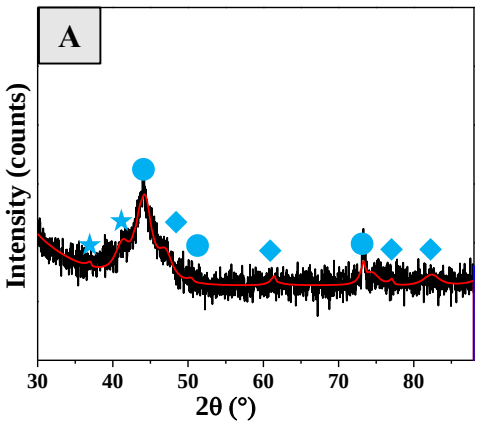
To assess the reducibility of supported calcined Co catalyst, in situ PXRD experiments were conducted. The promoted and unpromoted Co catalysts supported inside the nitrogen doped carbon support (Co@NHCS, Co@NHCS@Ru and Co-Ru@NHC) were subjected to isothermal reduction using a 50% H_2 /50% N_2 gas mixture passed over the sample at 450 °C for 4 hours. The obtained reduction patterns are shown in figure 4.10. The Co phases and position obtained for each catalyst were also tabulated (table S4.1). Rietveld refinement was used to quantify the relative Co phases that were obtained as to approximate the degree of reduction. The obtained values for the respective catalysts are shown in table 4.5. Noticeable from the obtained PXRD data of the supported Co catalysts is that (i) the reducibility of Co oxide was dependent on the presences and location of the Ru promoter metal. The presence of the Ru determined the degree of reduction of the Co oxide, (ii) catalysts showed characteristic Co reduction as the obtained phases were the CoO phase and the metallic Co phase and (iii) the peak intensity of the reduced Co phases indicated that more of the reduced Co was present (high intensity e.g. Co (fcc) = 44°).

The PXRD pattern for the unpromoted Co@NHCS (fig. 4.10A) catalyst after reduction showed peaks for CoO, hexagonal close packed Co (Co_{hcp}) and face centered cubic Co (Co_{fcc}) cobalt phases at 2θ value of 37.96, 47.11 and 50.94 respectively. [42] The other peaks corresponding to these phases have been tabulated elsewhere (table 4S.1). The relative values

were; 24% Co_{fcc}, 35 % Co_{hcp} and 41 % CoO. The Co_{hcp} phase was more abundant than the Co_{fcc} phase.

The addition of a Ru promoter to the Co catalyst (Co-Ru@NHC, fig.4.9C) showed improved Co oxide reduction. This catalysts was obtained with 58% Co_{fcc}, 41 % Co_{hcp} and 1 % CoO. The catalyst promoted more Co_{fcc}. The incomplete reduction (1 % CoO) could be due to the nanoparticles interacting strongly with the nitrogen groups. In another study where undoped carbon was used as a support, the opposite was observed and it was reported that more of the Co_{fcc} phase was produced. [20] This difference could be attributed to the nature of the support. [43, 44] The high reducibility of the Co-Ru@NHCS catalyst can be attributed the direct contact between the Co oxide and the Ru metal thus facilitating primary hydrogen spillover. This observation is in agreement with TPR analysis.

The Co@NHCS@Ru catalyst (fig. 4.10B), in which the Co oxide and the Ru metal were separated by the nitrogen doped carbon support, showed 9 % Co_{fcc}, 88 % Co_{hcp} and 3 % CoO. The catalyst showed improved Co oxide reduction and also promoted the formation of Co_{hcp}. The improved reduction can be attributed to a secondary hydrogen spillover effect. In summary, the degree of reduction (fig. 4.11) was obtained as 59 %, 97 % and 99 % for Co@NHCS, Co@NHCS@Ru and Co-Ru@NHCS catalysts, respectively. This observation is in agreement with hypothesis that the presence of the Ru promoter improves the reduction of the Co catalysts by hydrogen spillover. The lower degree of reduction on the unpromoted Co@NHCS catalyst can be attributed to absence of hydrogen spillover.



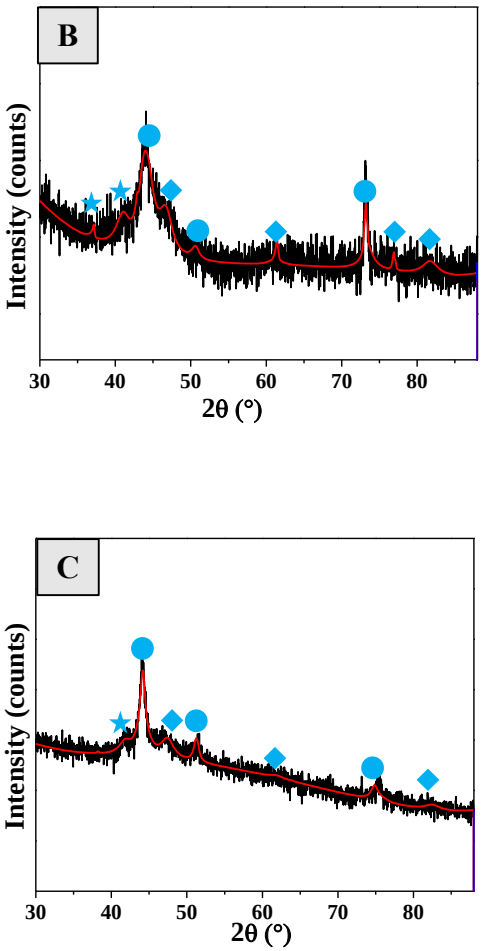


Figure 4.10 PXRD patterns of Co catalysts, reduced in H_2 gas at 450 °C for 3 hours. (**A**) Co@NHCS, (**B**) Co@NHCS@Ru, (**C**) Co-Ru@NHCS; CoO (★), Co_{hcp} (◆), Co_{fcc} (●)

Table 4.5 PXRD patterns of Co catalysts, reduced in H_2 gas at 450 °C for 3 hours.

Sample	Co phase (%)			Degree of reduction (%)
	CoO ★	Co_{hcp} ◆	Co_{fcc} ●	
Co@NHCS	41	35	24	59
Co@NHCS@Ru	3	88	9	97
Co-Ru@NHCS	1	41	58	99

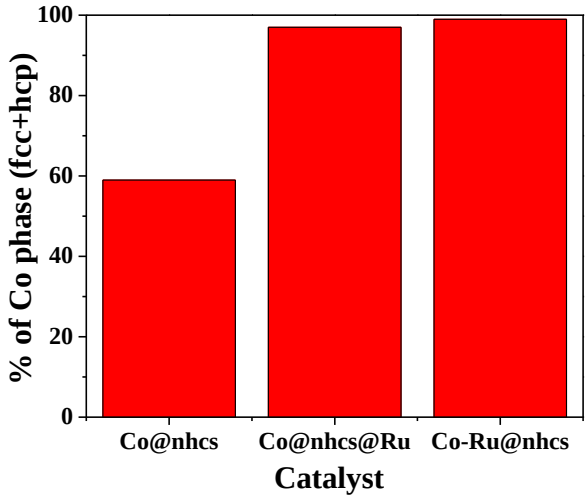


Figure 4.11 Degree of reduction for Co catalysts.

4.1.5. Conclusions

Nitrogen doped hollow carbon spheres (NHCS) were synthesized using polystyrene as a template and used as a support for Ru promoted Co catalysts. The supported Co catalysts were studied using TPR analysis to assess hydrogen spillover by Ru nanoparticles when the carbon support was doped with nitrogen. To distinguish between primary hydrogen spillover and secondary hydrogen spillover effects, the Co and Ru nanoparticles were placed on different regions of the nitrogen doped carbon support. Therefore it can be said that:-

- Polystyrene was a good and stable template for synthesizing the NHCSs as the carbon support was spherical and had a hollow morphology.
- NHCS was a good support and the hollow core effectively stabilized the Co and Ru metal nanoparticles as they were obtained in small sizes and with a with narrow particle size distribution.
- CHNS analysis and XPS analysis confirmed the successful presence and incorporation N-atoms within the carbon matrix.
- The presence of Co and Ru nanoparticles when placed together inside nitrogen doped carbon shell (Co-Ru@NHCS; direct contact) promoted primary hydrogen spillover. A secondary hydrogen spillover effect was observed when Co and Ru nanoparticles were separated by the nitrogen doped carbon shell (Co@NHCS@Ru; indirect contact). Both primary and secondary hydrogen spillover processes showed the

highest degree of reduction due to the presence of the Ru promoter which led to a shorter distance being travelled by the hydrogen atom from the Ru to the Co oxide in primary spillover, while the support facilated facile hydrogen transport in the secondary spillover.

- The observed TPR reduction temperatures for the Co catalyst supported on a nitrogen doped carbon support were similar to those obtained when a non-doped carbon support was used.
- Thus it can be said that the data suggests that there was no pronounced improvement of hydrogen spillover in the presence of nitrogen functional groups when the melamine carbon coated HCS was used.
- The Co_{fcc}: Co_{hcp} ratio is affected by the type of spillover effect found for the Co/Ru catalysts.

4.2. Synthesis of N-doped hollow carbon spheres: effect of annealing time

4.2.1 Introduction

Porous carbon nanoreactors have attracted attention in material science research due to their potential use as supports in catalysis research. [45] Optimisation studies are usually preformed on catalyst supports to improve their properties and applications. In particular, a HCS with tuneable properties such as graphitic nature, surface functionality, surface area and porosity have been studied. These properties depend on the synthesis conditions used such as the type of carbon precursor, the temperature and the growth time. The organic carbon precursor resorcinol-formaldehyde and melamine –formaldehyde have been used and found to be good carbon precursors and carbon/nitrogen precursors as they can be polymerized at room temperature in the presences of an acidic or a basic catalyst. [46, 47] Following the polymerization of the precursors, pyrolysis of the polymer under inert conditions is required to produce the porous carbon network. This is a thermally induced activation step which helps to remove oxygen groups and any unstable molecules that could cause pore blockages. The variation of the pyrolysis conditions such as pyrolysis time and pyrolysis temperature has a great effect on the properties of the resulting carbon network. [48, 49] Herein we report a study on the effect of varying the pyrolysis time (1 h and 2 h) under similar thermal conditions (600 °C) on the properties of post nitrogen doped hollow carbon supports.

The NHCS support and Co@NHCS catalyst reported in section 4.1 were annealed for 2 hours (data reported in tables 4.1- 4.4). In the section we shall compare these two samples with those annealed for 1 hour, i.e. with samples called $NHCS_{1hr}$ and $Co@NHCS_{1hr}$.

4.2.2. Methodology and characterization

A similar synthesis method was used as reported in section 4.1.2 and is shown in figure 4.9. Briefly, Ru and Co nanoparticles were precipitated onto the polystyrene template using hydrazine as the precipitating agent to give Co/PSS. The Co/PSS composite or prisitine PSS was coated with the carbon precursor resorcinol formaldehyde followed by coating with the nitrogen precursor, melamine. The resulting composite, Co/PSS@RF-melamine or PSS@RF-melanime, was thermally activated under inert conditions in a horizontal furnace by decomposing the template at 350 °C for 1 hour and annealing the polymer composite at 600 °C for 1 hour. The obtained black product obtained was ground and stored in a sample vial

labelled Co@NHCS$_{1hr}$ or NHCS$_{1hr}$. The Co@NHCS$_{1hr}$ catalyst was calcined at 210 °C for 2 hours under a flow of 5% O_2/bal Ar gas mixture to ensure that most of the metallic Co is converted to the Co_3O_4 phase.

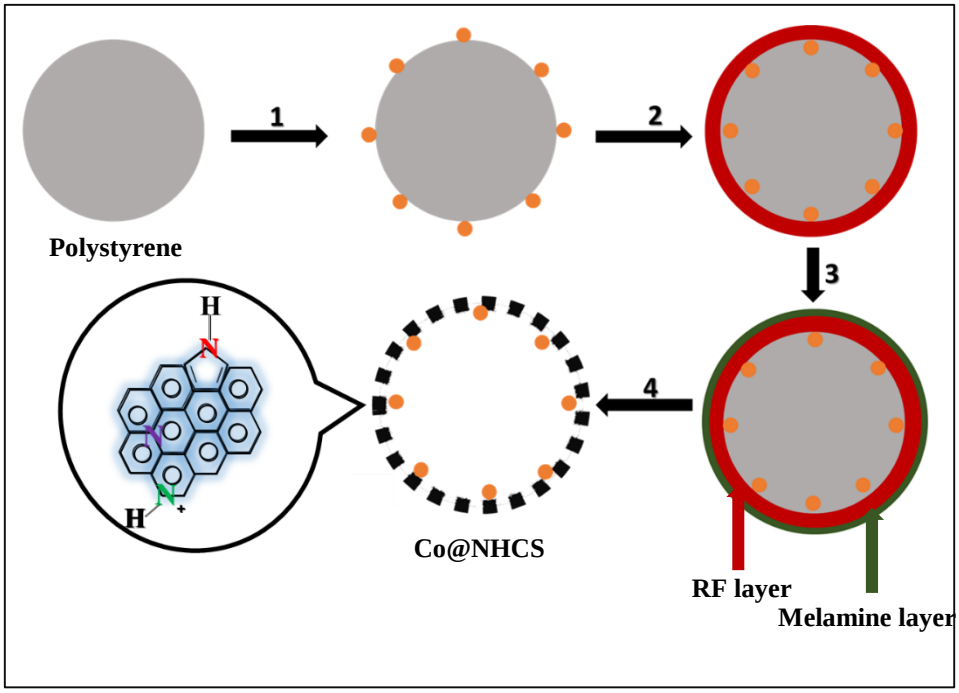


Figure 4.12 Schematic representation of the synthesis methodology. **(1)** loading Co metal onto a polystyrene template; **(2)** resorcinol-formaldehyde (carbon precursor) coating; **(3)** melamine (nitrogen precursor) coating and **(4)** template decomposition and annealing

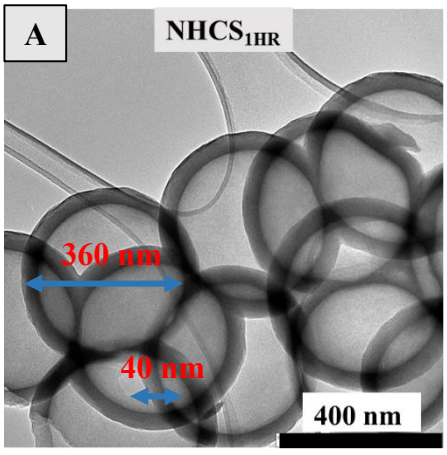
4.2.3. Results and discussion

The data from section 4.1 for the two samples, NHCS and Co@NHCS, has been included here. The difference between the samples in section 4.1 and the ones prepared in this section was the duration of annealing step at 600 °C which was done for 1 hour instead of 2 hours. This does lead to some repetition, but it allows one to make a comparison between the NHCS naterials prepared using different annealing durations. To make for an easier read the samples from section 4.1 are called NHCS$_{2hr}$ and Co@NHCS$_{2hr}$ in this section.

TEM analysis.

The synthesis route used to make the nitrogen doped carbon support (NHCS) and catalysts supported inside nitrogen doped carbon supports (Co@NHCS) involved the successive coating of the template (polystyrene) or metal loaded template with a shell of a carbon precursor and a nitrogen precursor, resorcinol-formaldehyde and melamine, respectively. Subsequently, the resulting composites were annealed for 1 hour and 2 hours at 600 °C, under a N_2 environment. Annealing the composites was done to decompose the template and transform the coated shell to a purely nitrogen-doped carbon shell. The synthesis method is presented in fig. 4.12.

The external morphology of the NHCS and particle size of the Co metal nanoparticles encapsulated inside the NHCSs were studied using TEM analysis. The obtained TEM images and particle size distribution are shown in fig. 4.13. The NHCS support annealed for 1 hour and 2 hours had the same shell diameter of 360 ±20.3 nm and shell thickness of 40 ± 15.2 nm. This shows that increasing the annealing time from 1 hour to 2 hours had no effect on the shell thickness or the diameter of the NHCS support (fig. 4.13**A**; $NHCS_{1hr}$ and fig. 4.13**C**; $NHCS_{2hr}$). The shell thickness and diameter of the spheres are affected by the resorcinol: formaldehyde: melamine ratio and size of the template, respectively. [45] However, Co nanoparticles encapsulated in the NHCS (Co@$NHCS_{1hr}$ and Co@$NHCS_{2hr}$) were affected by the increase in annealing time (fig. 4.13C and fig. 4.13F). The average diameter of the nanoparticles (table 4.6) increase from 4.1 ± 1.0 nm to 6.0 ± 1.5 nm with increase in the annealing time.



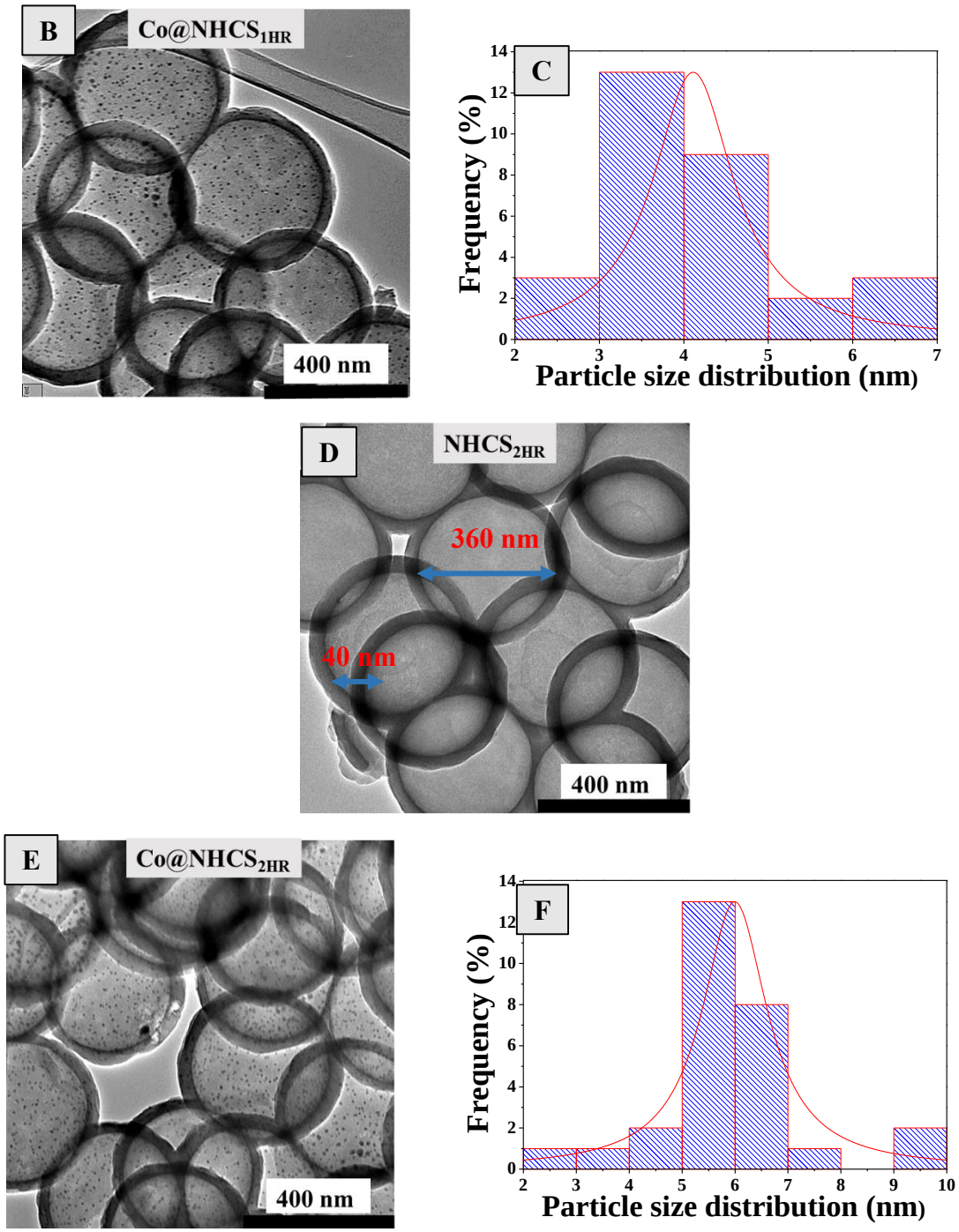


Figure 4.13 TEM images of catalyst supports and supported catalysts with corresponding metal particle size distribution when annealed for 1 hour (**A, B, C**) and 2 hours (**D, E, F**). **(1hr)** 1 hour annealing time; **(2hr)** 2 hours annealing time.

PXRD and TGA analysis

PXRD analysis was done to qualitatively assess the bulk composition of the catalyst supports (NHCS) and the supported catalysts (Co@NHCS), annealed for 1 hour and 2 hours. PXRD

patterns of the catalyst support and the supported catalyst annealed for 1 hour ($NHCS_{1hr}$ and $Co@NHCS_{1hr}$) and 2 hours ($NHCS_{2hr}$ and $Co@NHCS_{2hr}$) are shown in fig. 4.14A and fig. 4.14B, respectively. The $NHCS_{1hr}$ and $NHCS_{2hr}$ catalyst supports show two diffraction peaks, at approximately 22° and 44.5°, which can be attributed to 002 interlayer reflection of stacked carbon and 101 in-plane scattering of graphitic ordered carbon, respectively. [50] The PXRD pattern of $Co@NHCS_{1hr}$ shows diffraction peaks at approximately 2θ values of 22°, 37° and 46°. The diffraction peak at 22° can be attributed to 002 reflection plane of carbon. The broad diffraction peaks at 37° and 46° can be attributed to face centred cubic phase of Co_3O_4. [50] The Co_3O_4 peaks are broad and the broadness can be correlated to the small crystallite size which is in agreement with the nano-size particles seen in the TEM micrographs. The $Co@NHCS_{2hr}$ catalyst showed similar peaks but there is a downshift of the 002 peak to 20° from 22°. This is due to the decrease in the crystallinity of the material.[51] The PXRD data could not be used for any Co quantitative measurement due to the low resolution of the obtained diffraction patterns because a Cu Kα radiation source was used. Better resolution in the diffraction patterns would have been obtained if a Co Kα radiation source had been used when analysing Co containing samples. [52]

TGA analysis was done to assess the thermal stability and Co % loading of the annealed catalyst supports and supported catalysts produced after the two different annealing times. The thermographs obtained are shown in fig. 4.14C and fig. 4.14D. The observed onset decomposition positions and weight % of the residues are summarized in table 4.6. The samples annealed for 1 hour (fig. 4.14C) had an onset decomposition of 403 °C for the $NHCS_{1hr}$ catalyst support and at 331°C for the $Co@NHCS_{1hr}$ supported catalyst. The samples annealed for 2 hours (fig. 4.14D), had higher onset decomposition positions of 468 °C for the $NHCS_{2hr}$ catalyst support and 330°C for the $Co@NHCS_{2hr}$ supported catalyst. The longer annealing time decreased the more amorphous regions and increased the ordering with the matrix. The lower onset decomposition of the supported Co catalysts (331 °C and 340 °C) is due to Co_3O_4 nanoparticles catalysing the oxidation process. [20] The derivative thermographs (fig. 4S.4 and 4S.5) of the catalyst support and supported Co catalysts show the temperature at which the majority of the carbon atoms are oxidized. A similar oxidation trend was observed. Residual wt % of the supported Co catalysts was 8.5 % and 9.0 %. This residue corresponds to Co_3O_4. Using the residual wt %, the theoretical Co loading were calculated to be 6 % and 7 % which was lower than the estimated loading of 10 % Co.

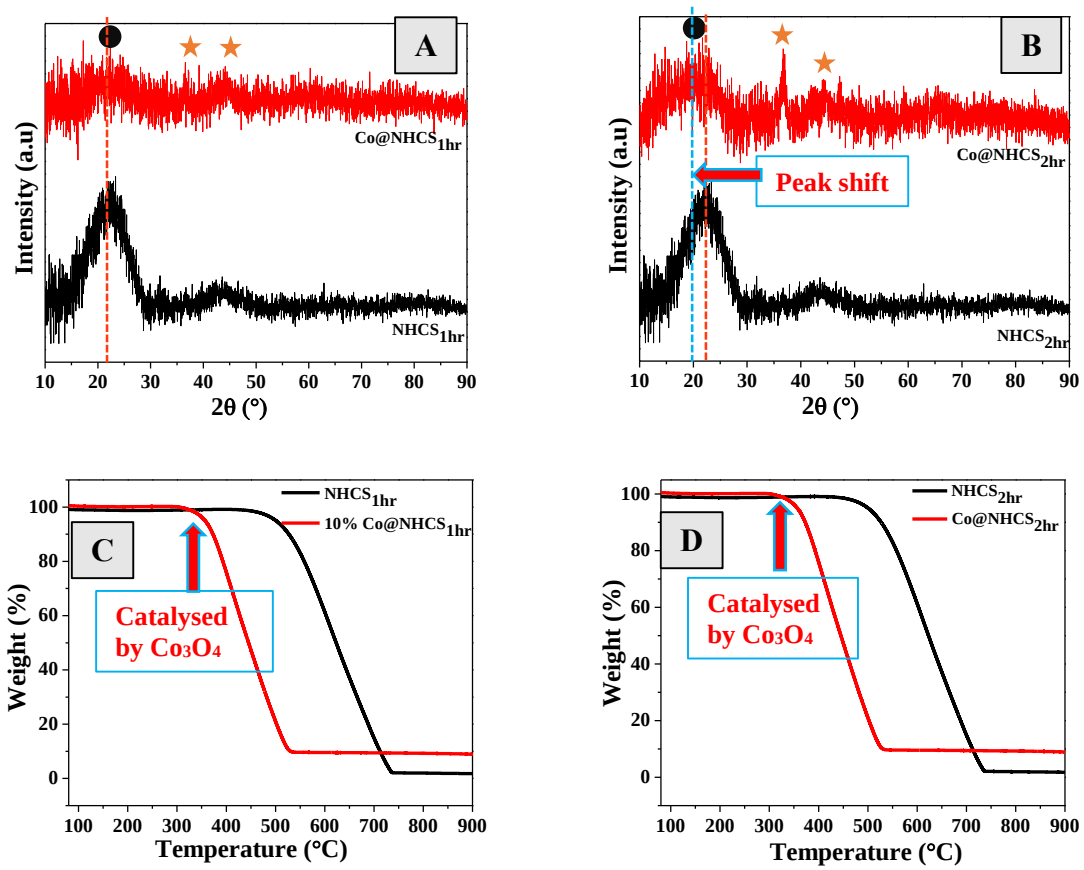


Figure 4.14 PXRD patterns (**A, B**) and TGA profiles (**C, D**) of catalysts. (**1hr**) 1 hour annealing time; (**2hr**) 2 hours annealing time; Carbon (●); Co_3O_4 (★)

Table 4.6 Thermal decomposition temperature, Co loading and Co particle size of the catalysts.

Sample	Decomposition temperature (°C)	Co_3O_4 wt % (TGA)	Particle size (nm) TEM
NHCS1hr	408	-	-
NHCS2hr	468	-	-
Co@NHCS1hr	331	8.5	4.1 ±1.0
Co@NHCS2hr	340	340	6.0 ±1.5

(**1hr**) 1 hour annealing time; (**2hr**) 2 hours annealing time.

XPS analysis

Nitrogen doped carbon supports have been widely studied and have been reported to assist in providing increased stability and durability to supported metal nanoparticles. The enhanced stability has been attributed to the electron donating abilities of nitrogen. Nitrogen species are seen as negative defects and hence make metal (positive ions) migration unfavourable. They also promote the adjacent carbons to be positively charged.[53, 54]

XPS analysis was used to analyse the quantity of nitrogen added into the carbon and to analyse the bonding configurations of nitrogen atoms that were incorporated within the carbon matrix during the post nitrogen doping process. The observed XPS N1s spectra of the nitrogen doped carbon support and of the Co catalysts supported inside the nitrogen doped carbon support, which were annealed for different durations, are shown in fig. 4.15. The XPS N1s spectra for the samples were deconvoluted into 4 component peaks and these peaks were attributed to pyridinic-N, pyrrolic-N, quaternary-N and oxidised-N configurations.[48] The quantities of each of the nitrogen bonding configurations determined are summarized in table 4.7. The catalyst support and the supported Co catalyst annealed for 1 hour ($NHCS_{1hr}$, $Co@NHCS_{1hr}$) show four deconvoluted peaks positioned at 389.2 eV, 399.4 eV, 400.7 eV and 402.3 eV. These peaks are attributed to pyridinic-N, pyrrolic-N, quaternary-N and oxidised-N configurations, respectively. [55] The $NHCS_{1hr}$ catalyst support has 47 % pyridinic-N, 28 % pyrrolic-N, 23 % quaternary-N and 2 % oxidised-N. The $Co@NHCS_{1hr}$ catalyst has 56 % pyridinic-N, 22 % pyrrolic-N, 20 % quaternary-N and 2 % oxidised-N. It is also noticeable that the low binding energy N-configurations, pyridinic-N and pyrrolic-N, are present in higher concentrations relative to the quaternary-N and oxidised-N. This could be attributed to pyridinic-N and pyrrolic-N being edge defects and hence they are easier to incorporate at the edges of the carbon matrix.[48, 56] It has been reported that pyridinic-N and pyrrolic-N are useful in FTS as metal anchoring sites. [38]

Increasing the annealing time to two hours, resulted in an increase in the concentration of oxidised species in the $NHCS_{2hr}$ (11 %) and $Co@NHCS_{2hr}$ (9 %) samples. It was noticeable that there was a marginal chemical shift towards lower binding energy of the oxidized species in $NHCS_{2hr}$ (401.8 eV) and $Co@NHCS_{2hr}$ (401.9 eV). The observed chemical shift may be attributed to w (i) the removal the non-valence electron charge, (ii) surface modification of the carbon and (iii) the change in the chemical environment of the carbon. [26, 57]

The Raman spectroscopy I_D/I_G ratio (table 4.7) represents the level of graphitization in the nitrogen doped carbon matrix. The Raman spectroscopy I_D/I_G ratios for $NHCS_{1hr}$ and $Co@NHCS_{1hr}$ are 0.88 and 0.93, respectively. This observation of a high I_D/I_G ratio for $NHCS_{1hr}$ and $Co@NHCS_{1hr}$ also agreement with the XPS data.

Additionally, it was observed that the presence of metal (Co or Ru) promoted rearrangement within the carbon matrix leading to a higher concentration of graphitic nitrogen. [2] Normally nitrogen doping is done in situ while making the HCSs. In this case the nitrogen was incorporated after the HCS was formed and after the metal was added. It is possible that the presence of the metals, Co and Ru, may have assisted any catalytic matrix rearrangement during the incorporation of nitrogen. [32]

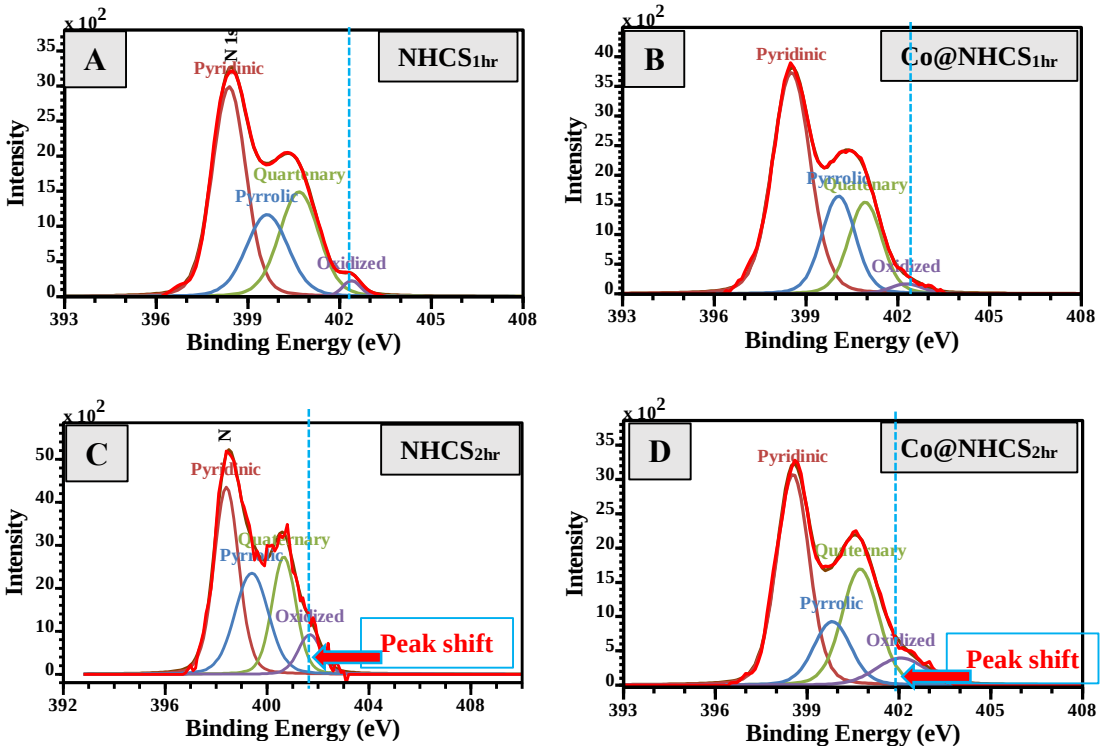


Figure 4.15 XPS N1s deconvulated spectra for the catalyst supports (**A**, **C)** and supported catalysts (**D, E)**. (**1hr)** 1 hour annealing time; **(2hr)** 2 hours annealing time.

Table 4.7 Nitrogen content, nitrogen cofiguration and Raman data of catalysts.

Sample	%N (XPS)	Pyridinic-N		Pyrrolic –N		Quaternary-N		Oxidised-N		I_D/I_G
		Peak position (eV)	%	Peak position (eV)	%	Peak position (eV)	%	Peak position (eV)	%	
$NHCS_{1hr}$	4.8	398.2	47	399.4	28	400.7	23	402.3	2	0.88
$NHCS_{2hr}$	7.0	398.2	31	399.4	36	400.7	22	401.8	11	0.77
$Co@NHCS_{1hr}$	5.3	398.2	56	399.4	22	400.7	20	402.3	2	0.93
$Co@NHCS_{2hr}$	6.7	398.2	46	399.4	16	400.7	29	401.9	9	0.92

(1hr) 1 hour annealing time; **(2hr)** 2 hours annealing time.

BET analysis

The physical properties of the catalysts i.e. surface area, pore volume and pore sizes were analysed using BET analysis and the results are summarized in table 4.8. The surface areas decreased with increase in the annealing time. This suggests that the removal of nitrogen leads to removal of defects (and porosity). The catalysts supports, $NHCS_{1hr}$ and $NHCS_{2hr}$, had the higher surface areas (201 m^2/g and 188 m^2/g) and the supported catalysts, $Co@NHCS_{1hr}$ and $Co@NHCS_{2hr}$, had lower surface areas (169 m^2/g and 143 m^2/g). The decrease of surface area could be attributed to the blockage of pores by the Co nanoparticles. [35] The catalysts support and supported catalysts had a mesoporous shell with pore sizes being between 2.5 nm and 5.3 nm. The low surface area for $Co@NHCS_{2hr}$ catalyst was unexpected. The catalyst was characterised several times but a similar surface area was obtained. Therefore, more studies will have to be performed to interpret this finding.

Table 4.8 Surface areas, pore volume and pore size of catalyst supports and supported catalysts. **(1hr)** 1 hour annealing time; **(2hr)** 2 hours annealing time.

Sample	Surface area (m^2/g)	Pore volume (cm^3/g)	Pore size (nm)
$NHCS_{1hr}$	201 ±4	0.31	4.5
$NHCS_{2hr}$	188 ±7	0.23	2.5
$Co@NHCS_{1hr}$	169 ±4	0.22	5.3
$Co@NHCS_{2hr}$	143 ±4	0.19	4.7

TPR analysis

The reducibility of the calcined (5% O_2/Ar) Co catalyst supported inside the nitrogen doped hollow carbon support and annealed for different durations ($Co@NHCS_{1hr}$ and $Co@NHCS_{2hr}$) were studied using TPR analysis. The recorded reduction patterns of the Co catalysts are shown in fig. 4.16 and the position of the reduction peaks are shown in table 4.9. The supported Co catalyst annealed for 1 hour, $Co@NHCS_{1hr}$, showed 3 reduction peaks. The first two peak at 185 °C and second peak at 266 °C (which is made up of 2 peaks) can be attributed to the $Co_3O_4 \rightarrow CoO$ reduction step. The third peak (386 °C) can be correlated to the reduction step $CoO \rightarrow Co$. The TPR pattern for this catalyst is not common and the synthesis and the characterization of the catalyst was repeated but similar results were always obtained (figure 4S.7). The supported Co catalyst annealed for 2 hours, $Co@NHCS_{2hr}$, showed 2 reduction peak. The first observed at 271 °C can be attributed to the $Co_3O_4 \rightarrow CoO$ reduction step and the second peak at 434 °C to the $CoO \rightarrow Co$ reduction step. It can be seen that $Co@NHCS_{1hr}$ catalyst resulted in cobalt oxide nanoparticles that were easier to reduce compared to the Co oxide nanoparticle of the $Co@NHCS_{2hr}$ catalyst. Usually larger sizes of Co oxide particles are reduced more easily compared those that are smaller.[17, 19, 20] Hence it would be expected that the larger particles of the catalyst $Co@NHCS_{2hr}$ (6.0 nm) to be reduced at lower temperatures compared to the smaller cobalt oxide particle of the catalyst $Co@NHCS_{1hr}$ (4.1 nm). The opposite was observed in this study. It is possible that the reduction of Co oxide could be dependent on the type of nitrogen incorporated (table 4.6 and fig.4.12). A short annealing time (1hour) resulted in the incorporation of more pyrrolic-N and

pyridinic-N which are known to be surface defects on the carbon matrix. It could be proposed that the pyrrolic-N and pyridinic-N enhanced the electronic conductivity hence improving the migration of the hydrogen ions on the surface of the support, thus allowing for the reduction of the Co oxide to occur at lower temperatures.

At high temperatures (>600 °C) during TPR analysis of carbon supported catalysts, the carbon catalyst support undergoes gasification ($C + H_2 \rightarrow CH_4$) and is seen as negative peaks in the TPR profiles. [58] The gasification process can be catalysed by reduced Co nanoparticles. The two supported Co catalyst showed two methanation peaks which were at 586 °C and 696 °C for the Co@NHCS$_{1hr}$ catalyst and were at 665 °C and 730 °C for the Co@NHCS$_{2hr}$. The peaks at 586 °C and 586 °C may be attributed to regions containing oxygen functionalities which are known to have the least thermal stability. [26, 58] Another possible explanation to these findings could be that the resorcinol-formaldehyde did not sufficiently anneal in the Co@NHCS$_{1hr}$ sample, hence the less stability and this is in agreement with the TGA analysis.

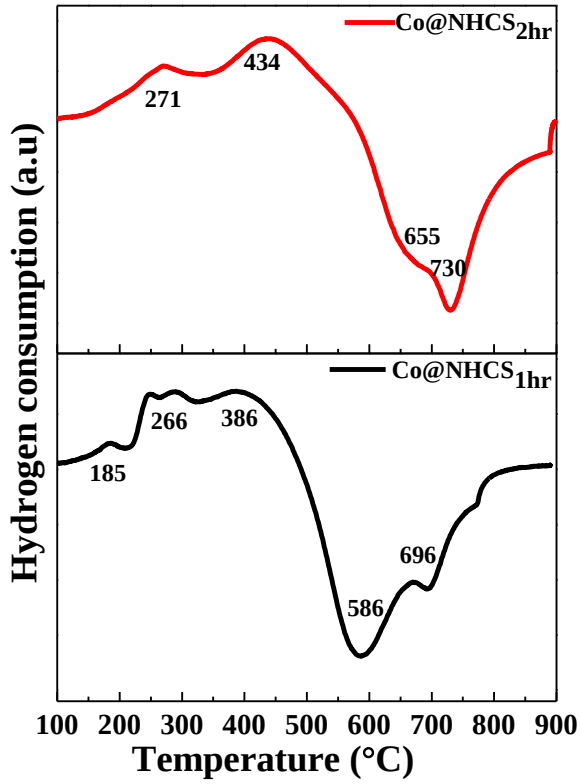


Figure 4.16 TPR profile for supported catalysts. **(1hr)** 1 hour annealing time; **(2hr)** 2 hours annealing time.

Table 4.9 TPR reduction peak positions of Co catalysts.

Sample	Cobalt oxide reduction temperature (°C)		Methanation temperature (°C)
	$Co_3O_4 \rightarrow CoO$	$CoO \rightarrow Co$	
Co@NHCS$_{1hr}$	185, 266	386	586, 696
Co@NHCS$_{2hr}$	271	434	655, 730

(1hr) 1 hour annealing time; **(2hr)** 2 hours annealing time.

4.2.4. Conclusions

The effect of varying the annealing time (1 hour and 2 hours) during synthesis of a nitrogen doped hollow carbon sphere (NHCS) and catalyst supported on a nitrogen doped hollow carbon sphere support (Co@NHCS) was studied. This was done to assess the effect of annealing on the structure of the support. The supported catalysts were used to study the reducibility of the Co oxide nanoparticles.

- TEM analysis showed that the annealing time had no effect on the shell thickness (40 nm) of the NHCS supports but influenced the particle size of the Co nanoparticle supported inside the nitrogen doped carbon support (Co@NHCS$_{1hr}$; d_{Co} = 4.1 nm and Co@NHCS$_{2hr}$; d_{Co} = 6 nm).
- TGA analysis revealed that the catalyst supports annealed for 1 hour oxidized more easily when compared to the catalyst support that was annealed for 2 hours (408 °C versus 468 °C).
- The TGA of the Co supported catalyst showed that Co_3O_4 catalysed the oxidation of the carbon support. However, the annealing time played no significant role.
- XPS analysis revealed that the annealing time has an effect on the N-type that results, i.e. more oxidized-N was observed when the annealing was done for 2 hours.
- Given the limited data set, no new conclusions can be drawn from the data at this time. Some interesting observations were noted, e.g. the increase in N-content in the XPS data with annealing time. In future experiments it is recommended to generate data (30 minutes; 4 hours) to see if trends can be reproduced.

4.3. Synthesis of N-doped hollow carbon spheres: in situ doping versus post doping

4.3.1. Introduction

Nitrogen doping is a method of modifying the structure of the carbon support through the incorporation of the heteroatom nitrogen within the carbon matrix. Nitrogen doping modifies the physiochemical properties of carbon materials thus increasing their use of as supports. [59] Incorporation of nitrogen within the matrix of a carbon support can be done via two different approaches, namely in situ nitrogen doping and post nitrogen doping. In situ doping entails the incorporation of nitrogen atoms during the growth of the carbon matrix thus resulting in nitrogen atoms being present throughout the carbon matrix of the support. In contrast, during post nitrogen doping, nitrogen atoms are introduced after the carbon matrix has formed and hence nitrogen atoms are incorporated only on the surface of the carbon. [60]

The nitrogen doping method has an effect on the type of nitrogen that is incorporated within the carbon matrix, the amount of nitrogen and the porosity. [61] The knowledge of these effects is important for any intended application of the material. [62]

4.3.2. Methodology and characterization

The synthesis of Co catalysts encapsulated inside the in situ nitrogen doped carbon support was done using the hard templating method. The synthesis methodology is shown in fig. 4.17. Briefly, a metal loaded template (Co/PSS; 2 g) was added into a homogeneous water-ethanol-ammonia solution (50 mL water; 100 mL ethanol, 1 mL ammonia) and sonicated for 30 minutes as to disperse the template. A separated homogenous mixture was prepared containing 25 mL ethanol, 25 mL H_2O, 1 g CTAB, 0.4 g resorcinol, 0.4 g melamine and 1.5 mL formaldehyde. The two mixtures were added together and sonicated for 10 minutes and further stirred at room temperature for 4 hours to coat the resorcinol-formaldehyde-melamine (RFM) polymer around the spherical template. This mixture was further heated at 70 $^{\circ}$C for 24 hours to speed up the process of RFM coating. The resulting reddish-brown solution was filtered, washed 4 times with 100 mL distilled water and dried at 80 $^{\circ}$C for 12 hours. The dried samples were ground and stored in a sample vial labelled Co/PSS@ RFM. Carbonization of the Co/PSS@ RFM was conducted using a horizontal CVD reactor, under inert conditions using inert gas (nitrogen) at a flow rate of 50 mL/min. This was done in a

successive two-step process, which involved the decomposition of the template (350 °C) and carbon annealing (600 °C). Briefly, 0.5 g composite Co/PSS@ RFM was weighed into a quartz boat, placed in the middle of a quartz tube and placed (quartz tube with boat) inside the horizontal CVD reactor. The decomposition temperature of the template was set to 350 °C, with a ramping rate of 3°C/min and holding time of 1 hour. The annealing temperature of the polymer was set to 600 °C with a ramping rate of 3°C/min and holding time of 2 hours. The black product was ground and stored in a sample vial labelled Co@$NHCS_I$. Prior to analysis the sample was calcined at 210 °C for 2 hours under 5% O_2/Ar as to convert all the cobalt to the Co_3O_4 phase.

The synthesis of Co catalysts supported on the post nitrogen doped hollow carbon sphere (NHCSs) support shown in fig. 4.17. Loading Co and Co-Ru metals onto the post nitrogen doped carbon support was done by the wetness impregnation (WI) method. Briefly, the metal salt (Co or Co-Ru) was dissolved in an ethanol solvent. The metal salt solution was added drop wise onto the NHCSs while stirring vigorously to form a thick paste. The paste was allowed to stir until the ethanol solution had evaporated and dried at 60 °C for 12 hours. The dried sample was thermally treated at 300 °C for 2 hours under nitrogen to decompose the metal precursor. The catalysts were labelled as Co-Ru/$NHCS_P$ and Co/$NHCS_P$. The catalysts were calcined at 210 °C for 2 hours under 5% O_2/Ar. The theoretical loading was estimated to be 10 % Co and 1 % Ru.

The calcined catalysts were characterized by transmission electron microscopy (TEM), Brunauer–Emmett–Teller (BET), powder X-ray diffraction (PXRD), thermo gravimetric analysis (TGA) and CHNS analysis. The reducibility of the Co catalysts was assessed using the temperature programmed reduction (TPR) technique. These characterization techniques and sample preparation method are detailed in chapter 3.

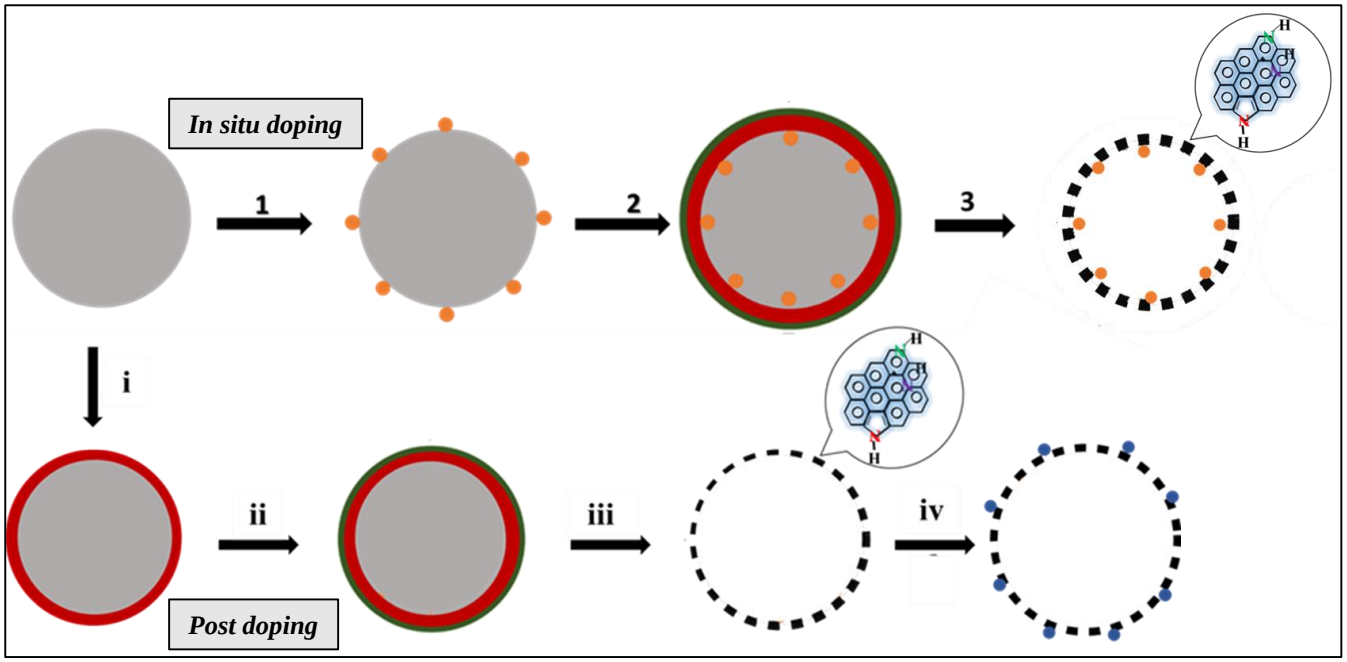


Figure 4.17 Schematic representation of the synthesis methodology. *In situ N-doping:* **(1)** metal (Ru and Co) wt % loaded onto a polystyrene template; **(2)** resorcinol-formaldehyde (carbon precursor) and melamine (nitrogen precursor) coating and **(4)** template decomposition and annealing. *Post N-doping:* **(i)** resorcinol-formaldehyde (carbon precursor) coating onto polystyrene template; **(ii)** melamine (nitrogen precursor) coating; **(iii)** template decomposition and annealing and **(iv)** metal (Co-Ru and Co) loaded onto nitrogen doped carbon support.

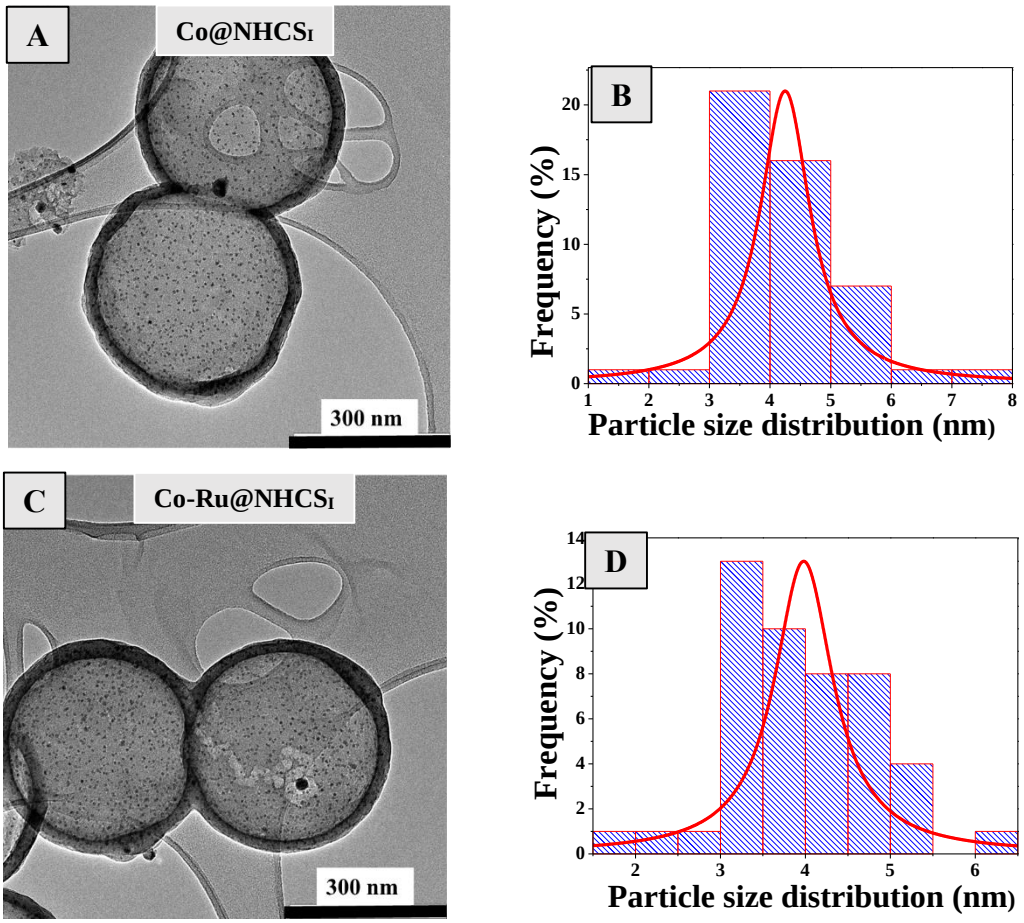
4.3.3. Results and discussion

The NHCSs sample from section 4.1 has been included here. However, this section it was used as a post nitrogen doped carbon support for the Co and Ru nanoparticles, therefore it has different structural properties which are necessary for this particular comparative study. The support is called $NHCS_p$.

TEM analysis

TEM images and corresponding particle size distributions of the Co catalyst supported inside the in situ nitrogen doped ($Co@NHCS_I$ and $Co\text{-}Ru@NHCS_I$) and Co catalysts supported on the outer surface of post nitrogen doping ($Co/NHCS_P$ and $Co\text{-}Ru/NHCS_P$) are shown in fig. 4.18. The in situ nitrogen doped carbon supports had a diameter of 380 nm and a shell

thickness of 25 nm. The Co@NHCS$_I$ (15% Co loading) catalyst was obtained with highly dispersed nanoparticles encapsulated inside the spherical nitrogen doped carbon support (fig. 4.18A) with a narrow particle size averaged at 4.2 ± 1.2 nm (fig. 4.18B). The Co-Ru@NHCS$_I$ (15 % Co loading) catalyst was also obtained with dispersed Co-Ru nanoparticles averaged at 4.0 nm (fig. 4.18C and fig. 4.18D). The wetness impregnation method (WI) was used to load metal nanoparticles (10% Co loading) onto the pre-synthesised post nitrogen doped hollow carbon support. Prior to characterization the metal loaded catalysts were treated in nitrogen (2 hours; 300 °C) to decompose the metal precursors and further treated in 5%O_2/Ar to convert all the Co to Co_3O_4. The nanoparticles were successfully loaded on to the support. Fig. 4.18E to fig. 4.18H shows the TEM images with their particle size distributions. The metal nanoparticles obtained showed some agglomerations (circled in red) and with a wide particle size distribution (2 nm to 16 nm) for the Co/NHCS$_P$ and Co-Ru/NHCS$_P$ catalysts. The WI impregnation method is a facile procedure commonly used for loading metal nanoparticles. The WI method has drawbacks such as low metal distribution and low dispersion of metal nanoparticles. [63]



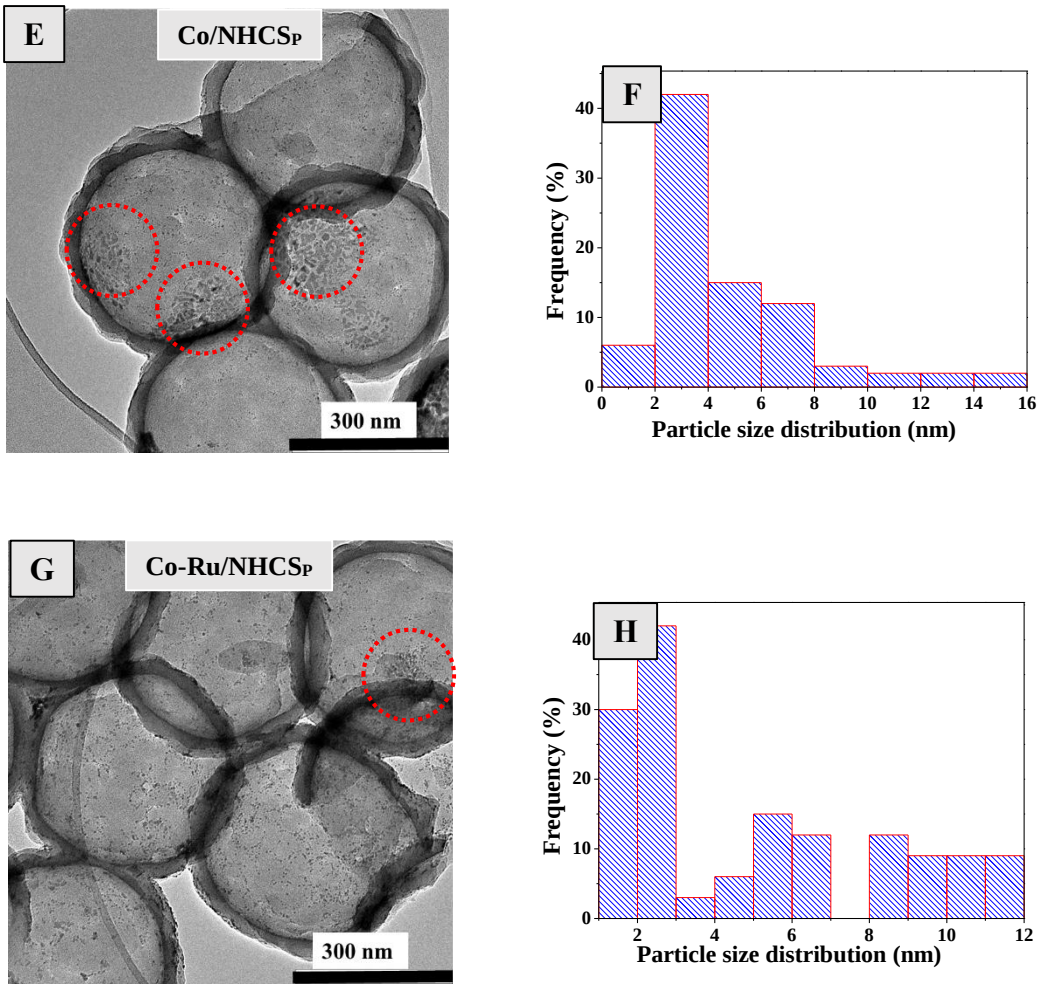


Figure 4.18 TEM images and particle size distributions of the supported catalysts. **(I)** in situ nitrogen doping; **(P)** post nitrogen doping.

PXRD and TGA analysis

Figure 4.19A shows PXRD patterns of the calcined catalysts encapsulated inside the in situ nitrogen doped hollow carbon sphere supports (Co@$NHCS_I$ and Co-Ru@$NHCS_I$) and catalyst supported on the post nitrogen doped hollow carbon sphere support (Co/$NHCS_P$ and Co-Ru/$NHCS_P$). The PXRD data diffraction patterns of the supported Co catalysts have a very low resolution because a $Cu_{K\alpha}$ radiation source was utilised. [52] The wavelength of a $Cu_{K\alpha}$ source is 1.54Å and matches the d-spacing of most crystalline solids.

A similar observation on all the catalysts is that there is no carbon diffraction peak to be seen, which is attributed to the low crystallinity carbon shell. The supported catalysts only show Co_3O_4 spinel phase and no Ru phases. The catalysts Co@$NHCS_I$ and Co-Ru@$NHCS_I$ show a broad diffraction at 45 ° which is attributed to Co_3O_4. The catalysts Co/$NHCS_P$ and Co-

Ru/$NHCS_P$ show diffraction peaks at 2θ values of 19 °, 31 °, 36 °, 45 °, 57 ° and 65 ° which are attributed to the Co_3O_4 spinel phase. [64] The broad peaks obtained correlate with the highly dispersed nanoparticle seen in the TEM micrographs, fig. 4.18.

The percentage loading of the Co nanoparticles supported on the nitrogen doped carbon spheres and stability of the nitrogen doped carbon sphere support were assessed using TGA analysis. The thermal stability of the catalyst was assessed in an oxidizing environment as the temperature increased linearly from 50 °C to 900 °C. Increasing the temperature in the oxidizing environment, the nitrogen doped carbon support is combusted to release $CO_{2\,(g)}$ and the loaded metal oxide remains as the residue. The obtained thermographs are shown in fig. 4.19B. The onset decomposition temperatures and metal loading are also summarized in table 4.9. The 15% Co@$NHCS_I$ catalyst showed initial carbon combustion at 325 °C and the 15% Co-Ru@$NHCS_I$ catalysts shows the initial carbon combustion at 322 °C. The weight residue which Co_3O_4 for these catalysts was 16 % - 18 %. The Co catalysts supported on post nitrogen doped hollow carbon sphere showed an initial carbon combustion at 395 °C on the 10% Co/$NHCS_P$ catalysts and 392 °C on the 10% Co-Ru/$NHCS_P$ catalysts. The weight residue of the catalysts (Co/$NHCS_P$ and Co-Ru/$NHCS_P$) was 8 % - 10%. The lower decomposition temperatures observed on carbon of the Co@$NHCS_I$ and Co-Ru@$NHCS_I$ catalysts (in comparison to Co/$NHCS_P$ and Co-Ru/$NHCS_P$ catalysts) can be attributed to nitrogen defects being present throughout the carbon matrix as a result of the in situ nitrogen doping and also the Co metal loading. The derivative thermographs (fig. S4.6) of the catalyst support and supported Co catalysts show the temperature at which the majority of the carbon atoms are oxidized. A similar oxidation trend was observed. This residual wt% of the Co catalysts corresponds to Co_3O_4. Using the residual wt %, the theoretical Co loading were calculated to be 6 % - 13 %.

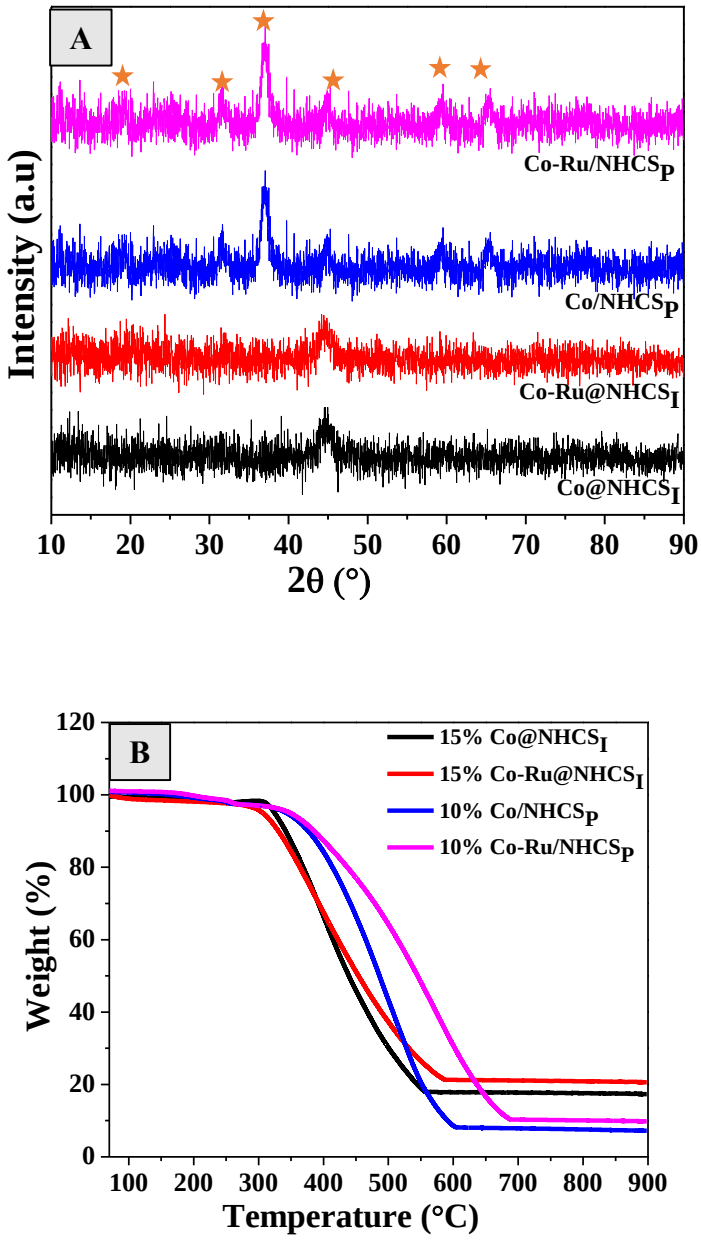


Figure 4.19 PXRD spectra (A) and TGA thermographs (B) of the catalysts. **(I)** in situ nitrogen doping; **(P)** post nitrogen doping. Co_3O_4 (★)

Nitrogen content and Raman analysis

The nitrogen content incorporated into the carbon matrix by in situ nitrogen doping and post nitrogen doping methods was quantified by CHNS analysis. The amounts of nitrogen and carbon obtained are summarized in table 4.10. The catalyst supports synthesized by in situ nitrogen doping have nitrogen content 9.33 % (Co@NHCS$_I$) and 8.39 % (Co-Ru@NHCS$_I$).

Catalyst supports synthesized by post nitrogen doping were characterized prior to loading the metal nanoparticles on the surface of the support. The nitrogen content on the post nitrogen doped carbon support was 7.21 %. The higher nitrogen content obtained on the carbon support synthesized by in situ nitrogen doping is in agreement with the lower thermal stability as seen in the TGA analysis (fig. 4.16B).

Raman analysis was done to assess the level of graphitization and level of disorder on the nitrogen doped carbon support and the results are shown in table 4.10. Two characteristic Raman peaks were obtained, the D-peak (1355 cm^{-1}) and the G-peak (1596 cm^{-1}). The level of defects is represented by the I_D/I_G ratio. The I_D/I_G ratio of the catalyst supported inside the situ doped carbon sphere support ($Co@NHCS_I$ and $Co\text{-}Ru@NHCS_I$) were 0.93 and 0.94 while the ratios of 0.77 and 0.69 were obtained for the catalyst supported on the outside of the post nitrogen doped hollow carbon sphere support ($Co/NHCS_p$ and $Co\text{-}Ru/NHCS_p$). The higher I_D/I_G ratio shows that the in situ doped carbon support had more defects and these results are in agreement with the high nitrogen content, higher Co loading and lower thermal stabilities observed for the catalysts.

Table 4.10 Thermal decomposition temperature, metal loading, elemental content and Raman data of catalyst.

Sample	TGA Decomposition temperature (°C)	Co_3O_4 wt % loading	Elemental content: elemental analysis at % (CHNS)		Wavenumber (cm^{-1})		I_D/I_G
			C	N	D-band	G-band	
$Co@NHCS_I$	325	16	81.34	9.33	1355	1596	0.93
$Co\text{-}Ru@NHCS_I$	322	18	82.91	8.39	1355	1596	0.94
$Co/NHCS_P$	395	8	85.37[a]	7.01[a]	1355	1596	0.77
$Co\text{-}Ru/NHCS_P$	392	10	85.37[a]	7.01[a]	1355	1596	0.69

[a] CHNS elemental analysis done before loading nanoparticles. **(I)** in situ nitrogen doping; **(P)** post nitrogen doping.

BET analysis

Table 4.11 summarizes the textural properties, surface areas, pore volumes and pore sizes, obtained from the BET analysis. The catalysts show surface areas 201 m^2/g ($Co@NHCS_I$), 188 m^2/g ($Co\text{-}Ru@NHCS_I$), 169 m^2/g ($Co/NHCS_P$) and 121 m^2/g ($Co\text{-}Ru/NHCS_P$). The catalyst supported on the in situ nitrogen doped carbon support ($Co@NHCS_I$ and $Co\text{-}Ru@NHCS_I$) show the highest surface area. The supported catalysts display a mesoporous shell with pore sizes between 3 nm and 5 nm.

Table 4.11 Surface area, pore come and pore size of the catalysts.

Sample	Surface area (m^2/g)	Pore volume (cm^3/g)	Pore size (nm)
$Co@NHCS_I$	201 ±4	0.31	4.1
$Co\text{-}Ru@NHCS_I$	188 ±3	0.23	5.0
$Co/NHCS_P$	169 ±4	0.15	3.4
$Co\text{-}Ru/NHCS_P$	121 ±4	0.14	3.3

(I) in situ nitrogen doping; **(P)** post nitrogen doping.

Co catalyst reducibility study: TPR analysis

TPR analysis was done to evaluate the reducibility of the Co catalyst supported on the in situ nitrogen doped carbon and post nitrogen doped carbon support. The reduction profile obtained for the calcined Co catalysts are shown in fig. 4.20 and the reduction peak positions are also summarized in table 4.12. As previously mentioned, the reducibility of cobalt oxide occurs through 2 steps, (i) $Co_3O_4 \rightarrow CoO$ and (ii) $CoO \rightarrow Co$ by the consumption of hydrogen atoms. The Co catalyst encapsulated inside the in situ nitrogen doped carbon support ($Co@NHCS_I$) showed 3 cobalt oxide reduction peak. The first 2 reduction at peaks at 201 °C and 293 °C can be attributed to the $Co_3O_4 \rightarrow CoO$ reduction process. A third reduction peak is seen at 439 °C which can be attributed to the $CoO \rightarrow Co$ reduction of Co oxide. When the Co catalysts was supported on the post nitrogen doped carbon support ($Co/NHCS_P$), similar Co oxide reduction peaks attributed to the $Co_3O_4 \rightarrow CoO$ reduction

process were observed at 199 °C and 293 °C, and a broad peak at 461 °C was for the CoO → Co reduction process.

Addition of a promoter metal, Ru, to the Co catalyst supported on the post nitrogen doped carbon support (Co-Ru/NHCS$_P$) resulted in the reduction of Co_3O_4 → Co occurring at 266 °C. This can be attributed to a primary hydrogen spillover effect. The broad peak observed at 343 °C could be attributed to the Co oxide species that have a stronger interaction with the nitrogen doped carbon support [38]. The TPR peaks observed at 199 °C (Co/NHCS$_P$) and 192 °C (Co-Ru/NHCS$_P$) could also be due to the decomposition of nitrate group. This identity of these chemical species could be verified by using TPR-MS (mass spectroscopy) technique. Negative peaks at higher temperatures (679 °C, 684 °C and 691 °C) were observed in all TPR data and these are attributed to the methanation of the carbon support. Reports have shown that the type of nitrogen doping used to dope carbon materials has an effect on the nitrogen type that is incorporated within the carbon matrix. [38]

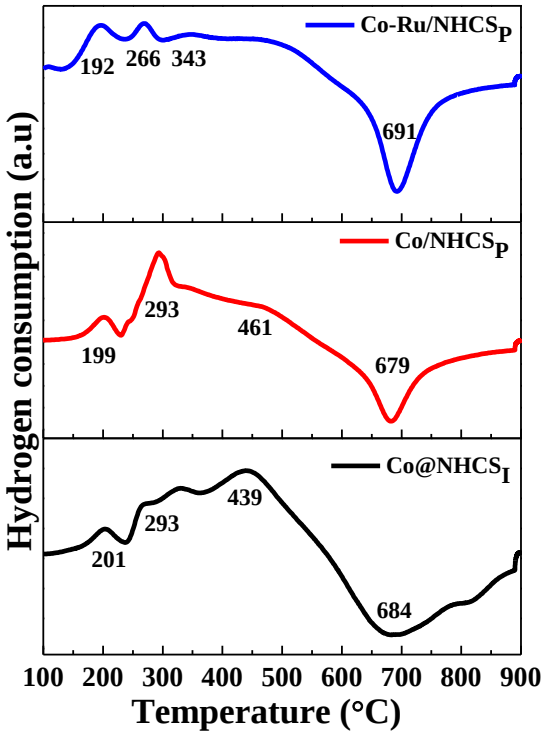


Figure 4.20 TPR profiles of supported catalysts. (**I**) in situ nitrogen doping; **(P)** post nitrogen doping.

Table 4.12 TPR reduction peak positions of supported Co catalysts.

Sample	Cobalt oxide reduction temperature (°C)		Methanation temperature (°C)
	$Co_3O_4 \rightarrow CoO$	$CoO \rightarrow Co$	
Co@NHCS$_I$	201, 293	439	689
Co/NHCS$_P$	293	461	679
Co-Ru/NHCS$_P$	266	266, 342	691

(I) in situ nitrogen doping; **(P)** post nitrogen doping.

4.3.4. Conclusions

Cobalt catalysts were supported on the inside of in situ nitrogen doped hollow carbon spheres (Co@NHCS$_I$) and supported on the outside of post nitrogen doped hollow carbon spheres (Co/NHCS$_P$ and Co-Ru/NHCS$_P$).

- TEM images of both the in situ nitrogen doped and post nitrogen doped hollow carbon support showed that the Co was well dispersed. Agglomeration of the Co nanoparticles supported on the post nitrogen doped carbon support was also observed.
- The Co catalysts supported on the inside of the in situ doped hollow carbon support (Co@NHCS$_I$) showed the lowest oxidative stability (TGA analysis) due to the nitrogen defects being present throughout the carbon matrix.
- The Co catalysts supported inside of the in situ doped hollow carbon support (Co@NHCS$_I$) also showed improved CoO → Co reduction and this is attributed to enhanced electronic conductivity, hence nitrogen defects are present throughout the carbon matrix.
- The loading of nanoparticles on samples Co/NHCS$_P$ and Co-Ru/NHCS$_P$ was done using the wetness impregnation method and thus the difference in behaviour of these samples may not be necessarily due to how the nitrogen as introduced to the sample.

4.4. References

1. Qian, W.; Zhang, H.; Ying, W.; Fang, D. *Chemical Engineering Journal* **2013**, *228*, 526–534.
2. Xiong, H.; Motchelaho, M. A. M.; Moyo, M.; Jewell, L. L.; Coville, N. J. *Journal of*

Catalysis **2011**, *278* (1), 26–40.

3. Yang, Y.; Chiang, K.; Burke, N. *Catalysis Today* **2011**, *178* (1), 197–205.
4. Yang, Y.; Jia, L.; Meng, Y.; Hou, B.; Li, D.; Sun, Y. *Catalysis Letters* **2012**, *142* (2), 195–204.
5. Subramanian, V.; Cheng, K.; Lancelot, C.; Heyte, S.; Paul, S.; Moldovan, S.; Ersen, O.; Marinova, M.; Ordomsky, V. V.; Khodakov, A. Y. *ACS Catalysis* **2016**, *6* (3), 1785–1792.
6. Yang, Y.; Liu, X.; Li, X.; Zhao, J.; Bai, S.; Liu, J.; Yang, Q. *Angewandte Chemie - International Edition* **2012**, *51* (36), 9164–9168.
7. Li, S.; Pasc, A.; Fierro, V.; Celzard, A. *Journal of Materials Chemistry A* **2016**, *4* (33), 12686–12713.
8. Park, J. C.; Lee, H. J.; Kim, J. Y.; Park, K. H.; Song, H. *Journal of Physical Chemistry C* **2010**, *114* (14), 6381–6388.
9. Han, J.; Xu, G.; Ding, B.; Pan, J.; Dou, H.; MacFarlane, D. R. *Journal of Materials Chemistry A* **2014**, *2* (15), 5352–5357.
10. Lee, H. J.; Choi, S.; Oh, M. *Chemical Communications* **2014**, *50* (34), 4492–4495.
11. Matsoso, B. J.; Ranganathan, K.; Mutuma, B. K.; Lerotholi, T.; Jones, G.; Coville, N. J. *RSC Advances* **2016**, *6* (108), 106914–106920.
12. Liang, C.; Li, Z.; Dai, S. *Angewandte Chemie - International Edition* **2008**, *47* (20), 3696–3717.
13. Nandiyanto, A. B. D.; Suhendi, A.; Ogi, T.; Umemoto, R.; Okuyama, K. *Chemical Engineering Journal* **2014**, *256*, 421–430.
14. White, R. J.; Tauer, K.; Antonietti, M.; Titirici, M. *Journal of the American Chemical Society* **2010**, *132* (49), 17360–17363.
15. Chen, A.; Wang, Y.; Yu, Y.; Sun, H.; Li, Y.; Xia, K.; Li, S. *Journal of Materials Science* **2017**, *52* (6), 3153–3161.
16. Girardon, J. S.; Quinet, E.; Griboval-Constant, A.; Chernavskii, P. A.; Gengembre, L.; Khodakov, A. Y. *Journal of Catalysis* **2007**, *248* (2), 143–157.
17. Hong, J.; Chernavskii, P. A.; Khodakov, A. Y.; Chu, W. *Catalysis Today* **2009**, *140* (3–4), 135–141.
18. Ikeda, S.; Tachi, K.; Ng, Y. H.; Ikoma, Y.; Sakata, T.; Mori, H.; Harada, T.; Matsumura, M. *Chemistry of Materials* **2007**, *19* (17), 4335–4340.
19. Fu, T.; Li, Z. *Chemical Engineering Science* **2015**, *135*, 3–20.
20. Phaahlamohlaka, T. N.; Kumi, D. O.; Dlamini, M. W.; Forbes, R.; Jewell, L. L.;

Billing, D. G.; Coville, N. J. *ACS Catalysis* **2017**, *7* (3), 1568–1578.

21. Yuan, C.; Liu, X.; Jia, M.; Luo, Z.; Yao, J. *Journal of Materials Chemistry A* **2015**, *3* (7), 3409–3415.
22. Pimenta, M. A.; Dresselhaus, G.; Dresselhaus, M. S.; Cançado, L. G.; Jorio, A.; Saito, R. *Physical Chemistry Chemical Physics* **2007**, *9* (11), 1276–1291.
23. Han, Z. J.; Huang, C.; Meysami, S. S.; Piche, D.; Seo, D. H.; Pineda, S.; Murdock, A. T.; Bruce, P. S.; Grant, P. S.; Grobert, N. *Carbon* **2018**, *126*, 305–312.
24. Ferrari, A. C.; Robertson, J. *Phys. Rev. B* **2000**, *61* (20), 14095–14107.
25. Zhang, G.; Ni, C.; Liu, L.; Zhao, G.; Fina, F.; Irvine, J. T. S. *Journal of Materials Chemistry A* **2015**, *3* (30), 15413–15419.
26. Mehetre, S. S.; Maktedar, S. S.; Singh, M. *Applied Surface Science* **2016**, *366*, 514–522.
27. Fang, J.; Fan, H.; Li, M.; Long, C. *Journal of Materials Chemistry A* **2015**, *3* (26), 13819–13826.
28. Bagus, P. S.; Ilton, E.; Nelin, C. J. *Catalysis Letters* **2018**, *148* (7), 1785–1802.
29. Qi, J.; Li, Y.; Wei, G.; Li, J.; Sun, X.; Shen, J.; Han, W.; Wang, L. *Separation and Purification Technology* **2017**, *188*, 112–118.
30. Ferrari, A. C.; Basko, D. M. *Nature Nanotechnology* **2013**, *8* (4), 235–246.
31. Ferrari, A. C.; Robertson, J. *Philosophical transaction of the royal society A* **2004**, *362* (1824), 2477–2512.
32. Xing, R.; Zhou, Y.; Ma, R.; Liu, Q.; Luo, J.; Yang, M.; Wang, J. *Journal of carbon research* **2018**, *4* (1), 11.
33. Gregg, S. J.; Sing, K. S. W.; Salzberg, H. J. *Electrochemical Society* **1967**, *114* (11), 2279C−279C.
34. Schneider, P. *Applied Catalysis A, General* **1995**, *129* (2), 157–165.
35. Hulicova-Jurcakova, D.; Seredych, M.; Lu, G. Q.; Bandosz, T. J. *Advanced Functional Materials* **2009**, *19* (3), 438–447.
36. Wang, L.; Yang, R. T. *Catalysis Reviews - Science and Engineering* **2010**, *52* (4), 411–461.
37. Roland, U.; Braunschweig, T.; Roessner, F. *Journal of Molecular Catalysis A: Chemical* **1997**, *127* (1–3), 61–84.
38. Xiong, H.; Motchelaho, M. A.; Moyo, M.; Jewell, L. L.; Coville, N. J. *Applied Catalysis A: General* **2014**, *482*, 377–386.
39. Jae, J.; Zheng, W.; Karim, A. M.; Guo, W.; Lobo, R. F.; Vlachos, D. G.

ChemCatChem **2014**, *6* (3), 848–856.

40. Kobayashi, H.; Matsuhashi, H.; Komanoya, T.; Hara, K.; Fukuoka, A. *Chemical Communications* **2011**, *47* (8), 2366–2368.
41. Taghavi, S.; Asghari, A.; Tavasoli, A. *Chemical Engineering Research and Design* **2017**, *119*, 198–208.
42. Garces, L. J.; Hincapie, B.; Zerger, R.; Suib, S. L. *Journal of Physical Chemistry C* **2015**, *119* (10), 5484–5490.
43. Karaca, H.; Safonova, O. V.; Chambrey, S.; Fongarland, P.; Roussel, P.; Griboval-Constant, A.; Lacroix, M.; Khodakov, A. Y. *Journal of Catalysis* **2011**, *277* (1), 14–26.
44. Elbashir, N. O.; Dutta, P.; Manivannan, A.; Seehra, M. S.; Roberts, C. B. *Applied Catalysis A: General* **2005**, *285* (1–2), 169–180.
45. Fang, X.; Zang, J.; Wang, X.; Zheng, M. Sen; Zheng, N. *Journal of Materials Chemistry A* **2014**, *2* (17), 6191–6197.
46. Jeong, H. M.; Lee, S. Y.; Shin, W. H.; Kwon, J. H.; Shakoor, A.; Hwang, T. H.; Kim, S. Y.; Kong, B. S.; Seo, J. S.; Lee, Y. M.; Kang, J. K.; Choi, J. W. *RSC Advances* **2012**, *2* (10), 4311–4317.
47. Yang, T.; Liu, J.; Zheng, Y.; Monteiro, M. J.; Qiao, S. Z. *Chemistry - A European Journal* **2013**, *19* (22), 6942–6945.
48. Al-Muhtaseb, S. A.; Ritter, J. A. *Advanced Materials* **2003**, *15* (2), 101–114.
49. Wang, Z.; Zhu, Y.; Luo, W.; Ren, Y.; Cheng, X.; Xu, P.; Li, X.; Deng, Y.; Zhao, D. *Chemistry of Materials* **2016**, *28* (21), 7773–7780.
50. Nongwe, I.; Ravat, V.; Meijboom, R.; Coville, N. J. *Applied Catalysis A: General* **2013**, *466*, 1–8.
51. Gong, Q. M.; Li, Z.; Wang, Y.; Wu, B.; Zhang, Z.; Liang, J. *Materials Research Bulletin* **2007**, *42* (3), 474–481.
52. Nachal. Devi.; Subramanian, G. Balaji, Challa S.S.R. Kumar, J. J. S. *Catalysis Today* **2009**, *147*, 100–106.
53. Corpuz, A. R.; Wood, K. N.; Pylypenko, S.; Dameron, A. A.; Joghee, P.; Olson, T. S.; Bender, G.; Dinh, H. N.; Gennett, T.; Richards, R. M.; O'Hayre, R. *Journal of Power Sources* **2014**, *248*, 296–306.
54. Mutuma, B. K.; Matsoso, B. J.; Ranganathan, K.; Keartland, J. M.; Wamwangi, D.; Coville, N. J. *RSC Advances* **2017**, *7* (34), 21187–21195.
55. Yang, Z.; Dai, Y.; Wang, S.; Cheng, H.; Yu, J. *RSC Advances* **2015**, *5* (95), 78017–

78025.

56. Nxumalo, E. N.; Letsoalo, P. J.; Cele, L. M.; Coville, N. J. *Journal of Organometallic Chemistry* **2010**, *695* (24), 2596–2602.
57. Chang, W. M.; Wang, C. C.; Chen, C. Y. *Electrochimica Acta* **2016**, *212*, 130–140.
58. Zhang, H.; Lancelot, C.; Chu, W.; Hong, J.; Khodakov, A. Y.; Chernavskii, P. A.; Zheng, J.; Tong, D. *Journal of Materials Chemistry* **2009**, *19* (48), 9241–9249.
59. Yoon, H.; Ko, S.; Jang, J. *Chemical Communications* **2007**, No. 14, 1468–1470.
60. Yadav, R.; Dixit, C. K. *Journal of Science: Advanced Materials and Devices* **2017**, *2* (2), 141–149.
61. Deng, Y.; Xie, Y.; Zou, K.; Ji, X. *Journal of Materials Chemistry A* **2016**, *4* (4), 1144–1173.
62. Ayala, P.; Arenal, R.; Rümmeli, M.; Rubio, A.; Pichler, T. *Carbon* **2010**, *48* (3), 575–586.
63. Iglesia, E. *Applied Catalysis A: General* **1997**, *161* (1–2), 59–78.
64. Fu, T.; Liu, R.; Lv, J.; Li, Z. *Fuel Processing Technology* **2014**, *122*, 49–57.

CHAPTER 5

Fischer-Tropsch synthesis: Preliminary catalyst testing studies

5.1. Introduction

Fischer-Tropsch synthesis (FTS) is a key commercial technological process where synthesis gas (carbon monoxide and hydrogen) is catalytically activated to produce hydrocarbons which are necessary for the production of energy, fuels and chemicals.[1] The catalytic activation of the synthesis gas is done on the surface of a metal catalyst such as cobalt. A Co catalyst has good selectivity, good activity and is relatively cheap. [2]

The catalytic activity of a Co catalyst is enhanced by supporting the nanoparticles on a porous solid carbon support (e.g. hollow carbon spheres) and by adding a promoter, such as Ru. The promoter helps to improve the catalytic activity by keeping the active sites on a Co catalyst clean and reduced. [3, 4] The high surface area of hollow carbon spheres improves the dispersion of Co nanoparticles. Additionally, the porous carbon shell helps to encapsulate Co nanoparticles, thus limiting particle growth and also provides hollow space in which catalytic reactions can take place. The pores also facilitate the diffusion of the reactants and products. [5] Furthermore, the modification of the carbon support through a nitrogen doping method is a strategy used to improve the activity of Co catalysts. The incorporation of nitrogen within the carbon matrix provides functional groups such as pyrrole and pyridine, which improve the stability of nanoparticles, thus enhancing the catalytic activity. [6]

In this chapter, nitrogen doped hollow carbon spheres (NHCSs) were used as a support for unpromoted and Ru promoted Co FTS catalyst (Co@NHCS and Co-Ru@NHCS). The preliminary FTS results on the Co catalysts are reported. The synthesis procedure and structural characterization of these catalyst has been discussed in chapter 4, section 4.1.2 and section 4.1.4.2.

5.2. Evaluation of FTS performance

The experimental catalytic evaluations of the catalysts were conducted using a tubular fixed bed low temperature FTS reactor. Briefly, 0.5 g of a calcined catalyst was placed inside the fixed bed reactor and reduced in-situ at 350 °C under a constant flow of H_2 gas (45 mL/min, 5 bar, 18 hours). Subsequently, syngas was introduced (10 bar; 20 mL/min) and the temperature was gradually increased from room temperature to the FTS temperature (220 °C, 240 °C). The maximum reaction time at each temperature was 50 hours.

A soap bubble flow meter was used to measure the flow rate of the gases. The reactor lines were kept hot, at 150 °C, so as to avoid any blockage during FTS. The pressure regulators and thermocouple respectively regulated and monitored the pressure and temperature during synthesis. The online gas chromatograph (GC) detectors, thermal conductivity detector (TCD) and flame ionization detector (FID), were used to separate and detect the products. The GC-TCD was fitted with a Carboxen-1000 60-80 mesh packed column and successfully detected N_2 gas, CH_4, CO_2 and unreacted syngas. The hydrocarbons which have low boiling points (cannot be condensed) were detected using the online GC-FID fitted with a Porapak Q packed column. The data obtained during synthesis was captured using the Clarity software package.

5.2.1. Fischer-Tropsch synthesis: Catalyst evaluation

The NHCSs were used as a nanoreactor to encapsulate unpromoted and Ru promoted Co catalyst nanoparticles (Co@NHCS and Co-Ru@NHCS). The activity of these calcined Co catalysts was tested using FTS at 10 bar for 50 hours, at temperatures of 220 °C and 240 °C. Prior to testing, the calcined catalysts were reduced in hydrogen (45 mL) at 350 °C for 18 hours. Figure 5.1 shows the CO conversion with time on stream for the catalysts and table 5.1 show the obtained CO conversion, activity and selectivity at each temperature.

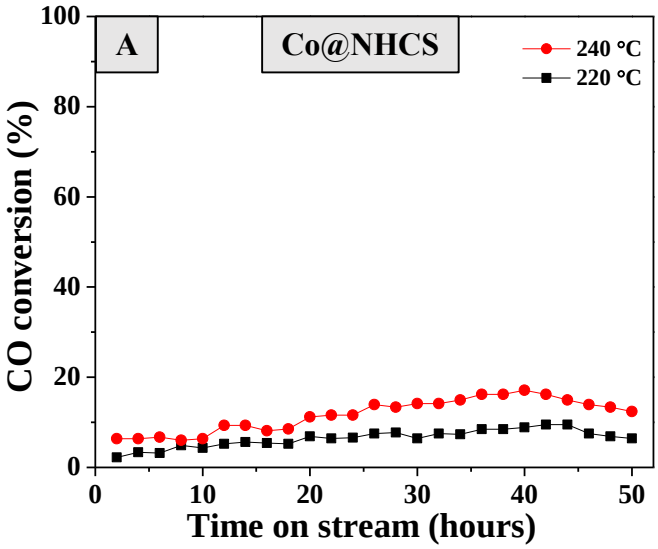
The unpromoted Co@NHCS catalyst (fig. 5.1A) showed CO conversion of 7.1 % and 15.6 % at a temperature of 220 °C and 240 °C, respectively. The catalyst showed an increase in the CO conversion at 10 hours on stream and reached steady state after 20-25 hours on stream.

The promoted Co-Ru@NHCS catalyst (fig. 5.1B) showed lower CO conversion of 6.2 % and 9.2 % at the same respective temperatures. The catalyst shows and increase in CO conversion up to 20-25 hours on stream before the catalyst reached steady state. The lower CO

conversion of the Ru promoted catalysts was unexpected as Ru is known to improve the activity of a catalysts. This observation could be related to the BET analysis findings which showed that the Co-Ru@NHCS catalyst has the lowest surface area. Hence this could be related to low diffusion/mass transfer effects.[7, 8]

The activity and selectivity of the catalysts (table 5.1) followed a similar trend as observed for the CO conversion at each FT temperature. The Co@NHCS catalyst had an activity of 2.46 x 10^{-3} at 220 °C and 5.56 x 10^{-3} at 240 °C while the Co-Ru@NHCS catalyst had activity of 2.03 x 10^{-3} and 3.09 x 10^{-3} at these respective temperatures. The selectivity towards methane (C_1) increased as the reaction temperature was increased. This occurs because at high temperature the hydrogenating property of a Co catalyst is enhanced thus leading to higher methane selectivity. [9] The higher selectivity towards C_{5+} hydrocarbons of the Co-Ru@NHCS catalysts can be attributed to an added reducibility of the Co catalyst by Ru. [10]

The olefin:paraffin ratios of light hydrocarbons (C_2-C_4) for both catalysts is shown in figure 5.2. The olefin:paraffin ratios of the light hydrocarbons decreased with an increase in CO conversion and activity of the catalysts. The increase of the C_4 olefin: paraffin ratio for the Co-Ru@NHCS catalyst compared to the other catalysts could be attributed to difference in polymerization mechanisms. [11, 12]



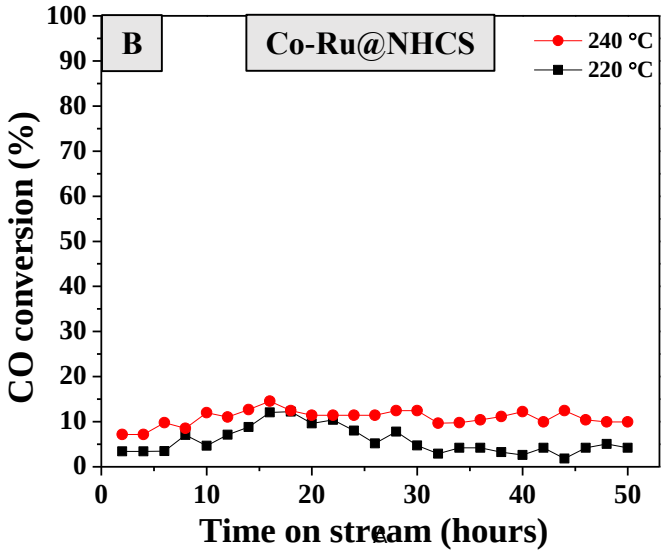


Figure 5.1 CO conversion (%) as a function of time in FTS of Co catalysts, (A) Co@NHCS, (B) Co-Ru@NHCS, at different FTS temperature.

Table 5.1 CO conversions, activity and selectivity of Co catalysts under FTS reaction.

Catalyst	FTS temperature (°C)	CO conversion (%)	Activity ($mol_{CO}/g_{Co}.h$)	Selectivity		
				C1	$C_2 - C_4$	C_{5+}
Co@NHCS	220 °C	7.1	$2.46x10^{-3}$	11.2	9.1	79.7
	240 °C	15.6	$5.56x10^{-3}$	29.8	11.9	58.3
Co-Ru@NHCS	220 °C	6.2	$2.03x10^{-3}$	7.9	2.9	89.2
	240 °C	9.15	$3.09x10^{-3}$	13.5	8.7	77.8

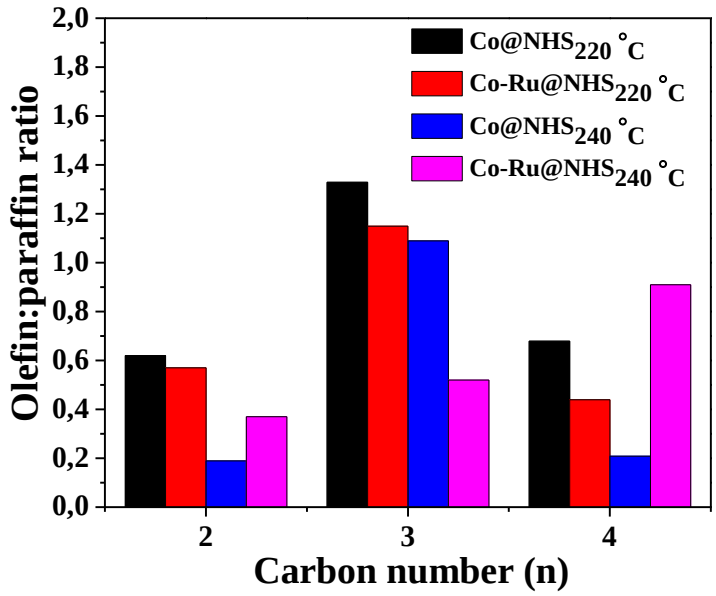


Figure 5.2 Olefin to paraffin ratio of Co catalysts, Co@NHCS and Co-Ru@NHCS, at different FTS temperature.

5.2.2. Conclusions

The unpromoted and Ru promoted Co catalyst supported inside nitrogen doped hollow carbon sphere were tested as low temperature FTS catalysts in a fixed bed reactor at 10 bar for 50 hours at temperatures of 220 °C and 240 °C. From the preliminary results it can be concluded that:-

- The unpromoted Co@NHCS catalyst had a higher CO conversion and catalytic activity than the promoted Co-Ru@NHCS catalyst. This is an unexpected result and will need to be repeated. The low activity of the catalyst could be attributed to low mass diffusion issues.
- The CO conversion and activity of the catalysts increased with temperature. This catalytic increase was followed by an increase in methane selectivity
- The olefin:paraffin ration of the catalysts decreased with increasing activity.

5.3. References

1. Förtsch, D.; Pabst, K.; Groß-Hardt, E. *Chemical Engineering Science* **2015**, *138*, 333–346.
2. Dry, M. E. *Catalysis Today* **2002**, *71* (3–4), 227–241.
3. Fu, T.; Li, Z. *Chemical Engineering Science* **2015**, *135*, 3–20.
4. Wolf, M.; Mutuma, B. K.; Coville, N. J.; Fischer, N.; Claeys, M. *ACS Catalysis* **2018**, *8* (5), 3985–3989.
5. Ikeda, S.; Tachi, K.; Ng, Y. H.; Ikoma, Y.; Sakata, T.; Mori, H.; Harada, T.; Matsumura, M. *Chemistry of Materials* **2007**, *19* (17), 4335–4340.
6. Xiong, H.; Motchelaho, M. A.; Moyo, M.; Jewell, L. L.; Coville, N. J. *Applied Catalysis A: General* **2014**, *482*, 377–386.
7. Prieto, G.; Tüysüz, H.; Duyckaerts, N.; Knossalla, J.; Wang, G. H.; Schüth, F. *Chemical Reviews* **2016**, *116* (22), 14056–14119.
8. Fang, X.; Liu, S.; Zang, J.; Xu, C.; Zheng, M. Sen; Dong, Q. F.; Sun, D.; Zheng, N. *Nanoscale* **2013**, *5* (15), 6908–6916.
9. Yang, J.; Ma, W.; Chen, D.; Holmen, A.; Davis, B. H. *Applied Catalysis A: General* **2014**, *470*, 250–260.
10. Yang, Y.; Liu, X.; Li, X.; Zhao, J.; Bai, S.; Liu, J.; Yang, Q. *Angewandte Chemie - International Edition* **2012**, *51* (36), 9164–9168.
11. Davis, B. H. *Industrial and Engineering Chemistry Research* **2007**, *46* (26), 8938–8945.
12. Komaya, T.; Bell, A. T. *Journal of Catalysis* **1994**, *146* (1), 237–248.

CHAPTER 6

Conclusions and recommendations

6.1 Conclusions

The aims of this study was to synthesize nitrogen doped carbon spheres (NHCSs) using a polystyrene template, to use the NHCSs as a model support for Ru promoted Co FT catalysts and to assess the efficiency of the NHCSs as a hydrogen transport layer. The catalysts were characterised using analytical techniques such as TEM, SEM, TGA, BET, XPS, CHNS, PXRD, Raman spectroscopy, in situ PXRD and TPR analysis. From the characterization results obtained, numerous conclusions were received.

The polystyrene was a good template to use for the synthesis of NHCSs. The NHCSs were obtained with a spherical morphology and attained a hollow morphology following the thermal decomposition of the polystyrene. The NHCSs were obtained with mono-dispersion, good thermal stability, an acceptable porosity and successful incorporation of nitrogen.

The Co and Ru metal nanoparticles encapsulated inside the hollow core of the NHCSs had good dispersion with little or no pronounced agglomeration. However a decrease in surface area of the metal catalysts was observed. The bimetallic catalyst, Co-Ru@NHCS, was obtained with the lowest surface area which was attributed to the blockage of pore by the nanoparticles.

Reduction studies revealed that the presence of Ru metal as a promoter enhanced the reducibility and the degree of reduction (DOR) of the Co oxide nanoparticles and also the Co metal phase. A primary hydrogen spillover effect was evoked to explain the complete Co oxide reduction at a temperature >300 °C and a high DOR of 99 % was obtained for the bimetallic catalyst in which Co oxide and the Ru promoter where placed in close proximity to each other. When the location of the metals was separated using the NHCSs support (Co@NHCS@Ru), a secondary hydrogen spillover effect was observed and a DOR of 97 % was obtained. The complete absence of a promoter gave a catalyst, Co@NHCS with a DOR

of 59 %. The presence of the Ru metal increased the relative abundance of the hexagonal closed packed (hcp) phase of the Co metal.

The preliminary results of the Fischer-Tropsch synthesis process will need to be repeated low activity on the Co-Ru@NHCS catalyst was unexpected and could possibly be due to mass transfer issues. The Fischer-Tropsch activity of the other catalysts will also be assessed.

Varying the annealing time between 1 hour and 2 hours had an effect on the structural properties of the catalysts i.e. particle size, thermal stability, nitrogen content and nitrogen configuration. The small particle size of metals and low thermal stability of the carbon support obtained using a shorter annealing time (1 hour) was expected because the nanoparticles, subjected to the shorter heat treatment, showed less particle growth. Increasing the annealing time to 2 hours showed that the nitrogen content and the relative abundance of oxidised nitrogen increased. This observation was attributed to the opening up of the carbon matrix during pyrolysis thus allowing for an increase in the incorporation of the defects (nitrogen). This observed trend is however not common and hence the generation of more data (30 minutes; 4 hours) is necessary to confirm the observed trend.

Using in situ nitrogen doped carbon versus post nitrogen doped carbon as a support for the Co and Ru nanoparticles showed an influence of the nitrogen on the carbon support. A less stable support was obtained for the in situ doped carbon due to the nitrogen defects being present throughout the carbon matrix.

In summary, the presence of nitrogen on the carbon support did not effectively improve the hydrogen spillover effect but did improve the degree of reduction.

6.2. Recommendations

The NHCSs were a good support for cobalt catalysts but did not improve the hydrogen spillover effect. Future projects will be:

- Repeat the FTS testing on the CoRu@NHCS catalysts.
- This could be done after improving the porosity of the catalyst so as to limit mass diffusion issues.
- Test the catalytic activity of the catalysts supported on the in situ doped carbon support

- To anneal the carbon support at shorter and longer times e.g. 30 minutes and 4 hours, so as to confirm the trends of nitrogen content and nitrogen configurations.
- To characterize the catalysts supported on the in situ nitrogen doped support using the in situ PXRD technique and via XPS analysis.
- Support Co nanoparticles on the outside of in situ doped carbon support.
- Use other nitrogen precursors i.e. urea, dopamine, ammonia etc., to dope the carbon support and observe if there are any improvements on the hydrogen spillover process.

Appendix

Chapter 4: Supporting information

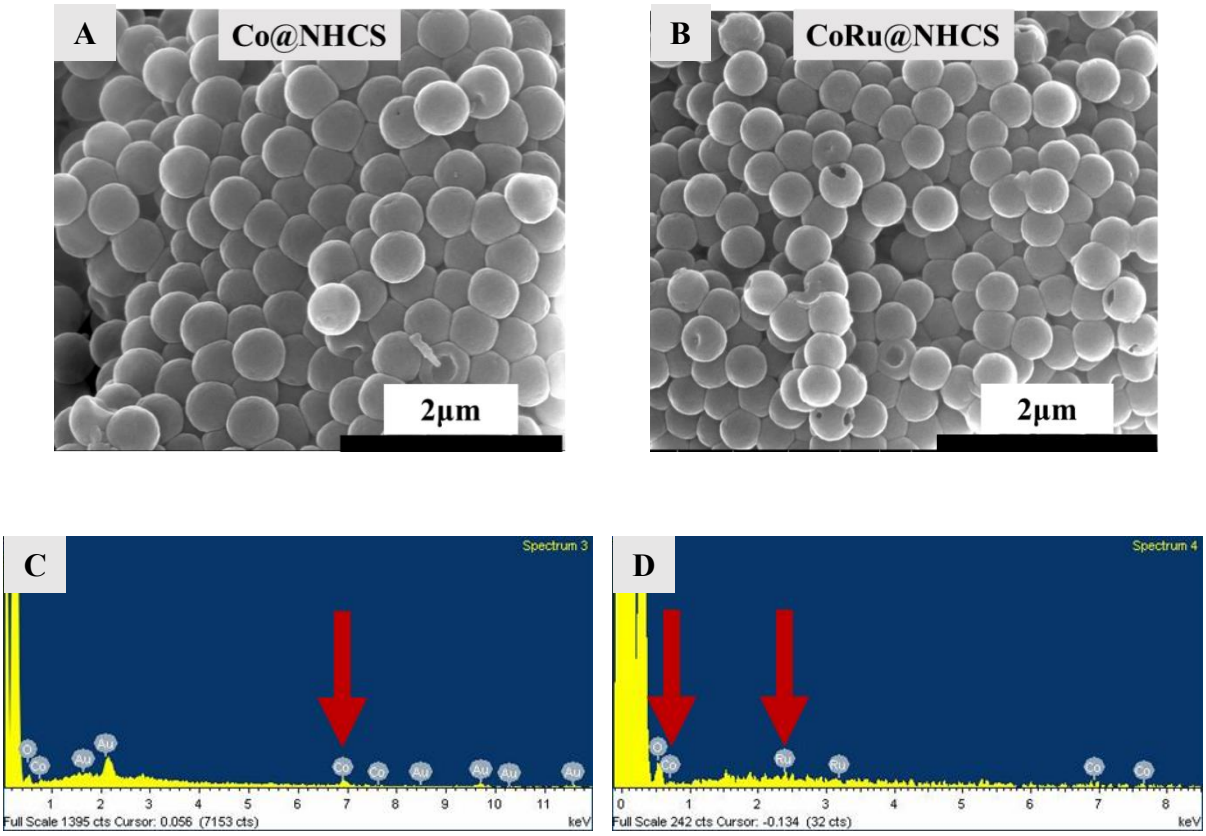


Figure 4S.1 SEM image with respective EDX spectrum of the catalysts, (**A** and **C**) 10% Co@NHCS; (**B** and **D**) 10% Co-Ru@NHCS.

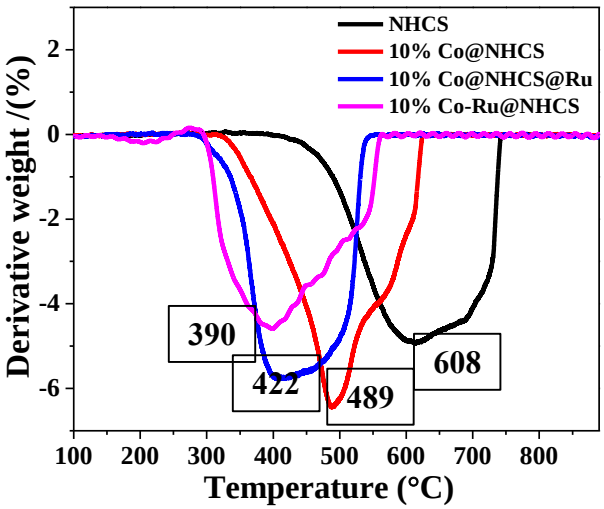
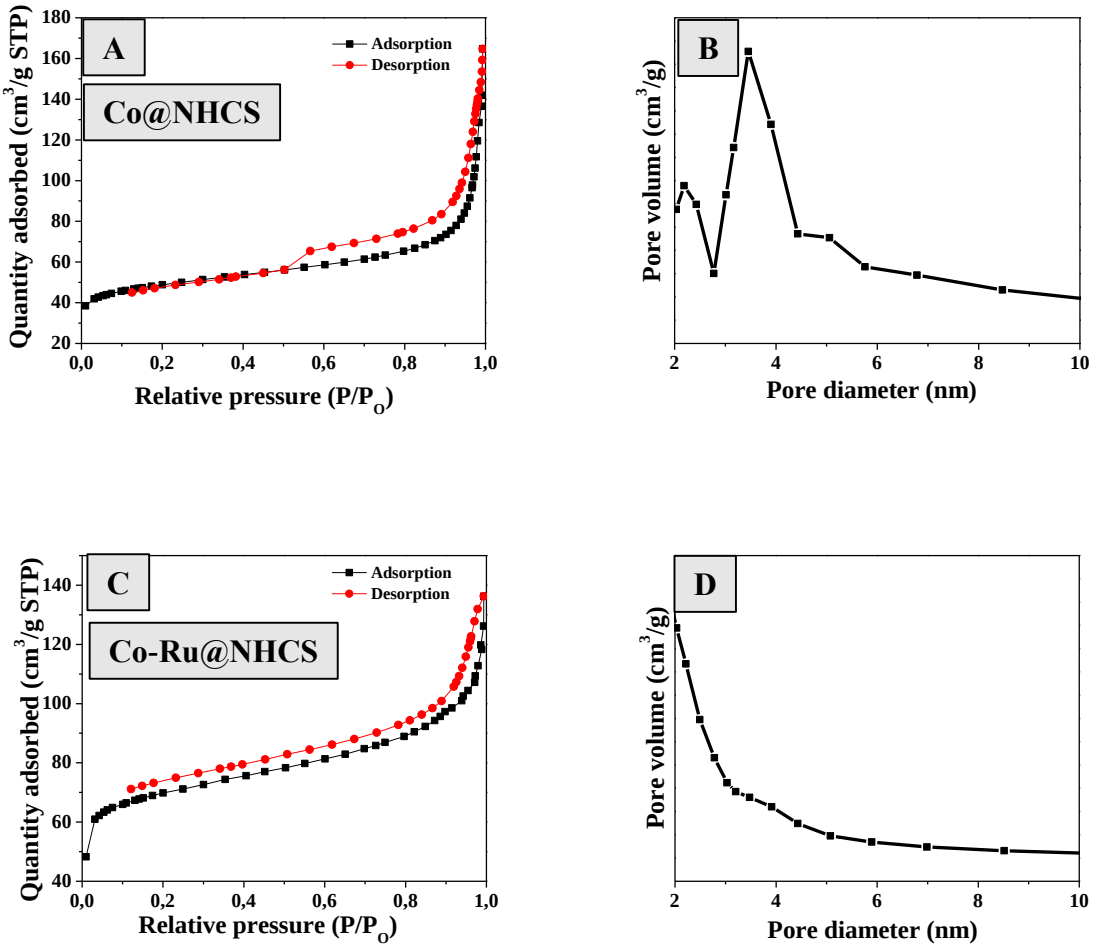


Figure 4S.2 Derivative TGA profiles of catalysts.



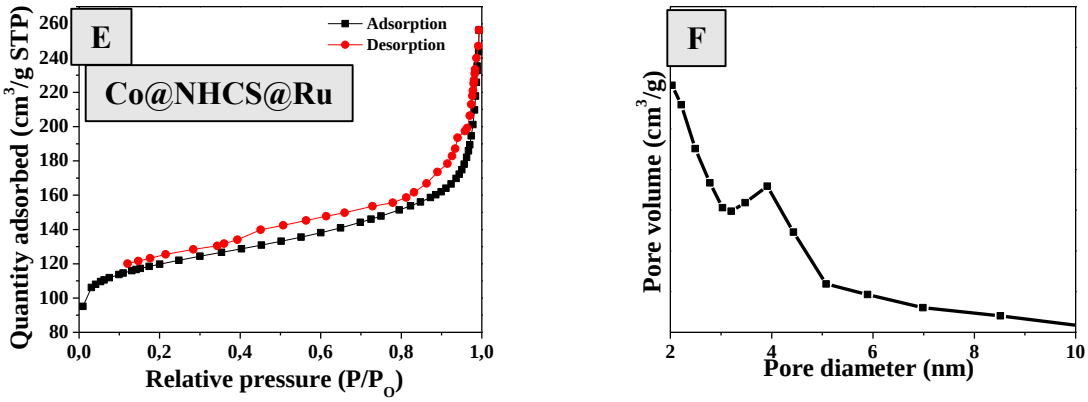


Figure 4S.3 N_2 adsorption-desorption isotherm (**A, C, E**) and the corresponding adsorption pore size distribution (**B, D, F**) for catalysts Co@NHCS, Co-Ru@NHCS and Co@NHCS@Ru, respectively.

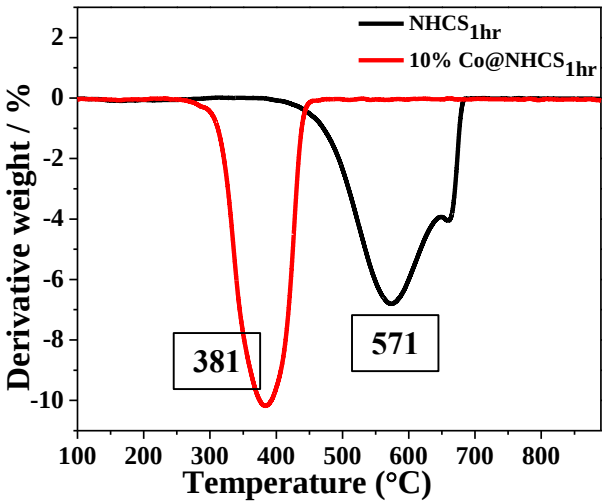


Figure 4S.4 Derivative TGA profiles of catalysts annealed for 1 hour.

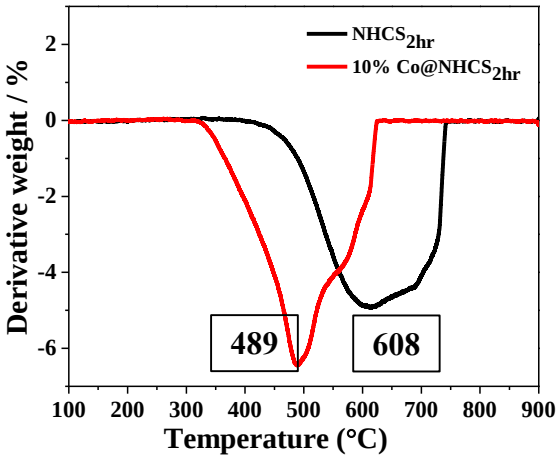


Figure 4S.5 Derivative TGA profiles of catalysts annealed for 2 hours.

Table 4S.1 Co phases obtained for different supported Co catalysts, reduced in H_2 gas at 450 ^{o}C for 3 hours.

Sample	Co phase positions(2θ)		
	CoO ★	Co_{hcp} ◆	Co_{fcc} ●
Co@NHCS	37.96 41.16	47.11 61.38 63.50 77.30 82.20	44.11 50.94 74.79
Co@NHCS@Ru	37.08 41.05	46.54 61.38 81.72	44.10 50.78 73.09 76.90
Co-Ru@NHCS	41.79	47.34 61.58 82.45	44.14 51.37 74.79

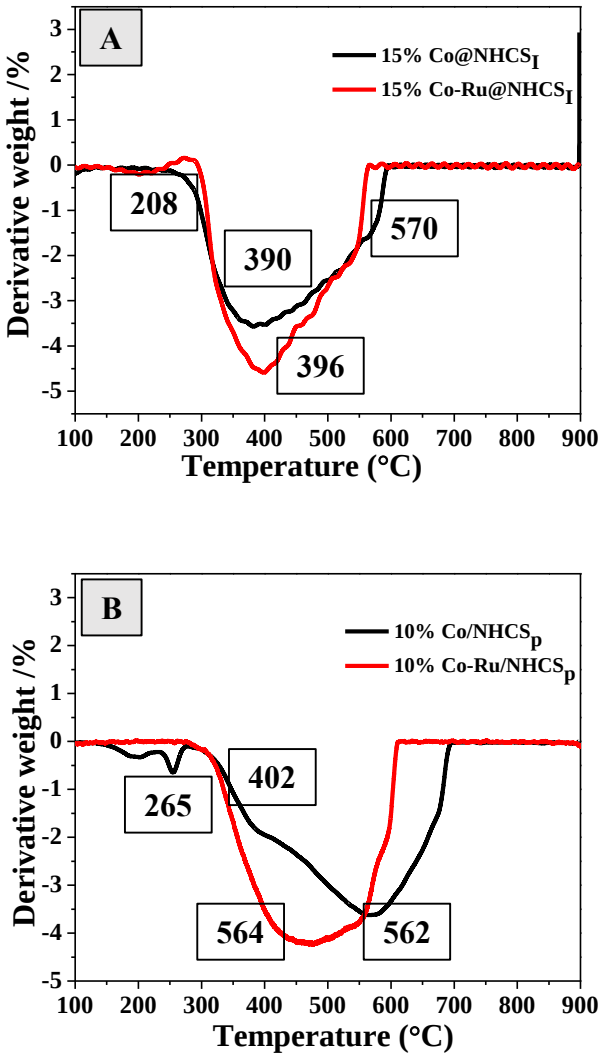
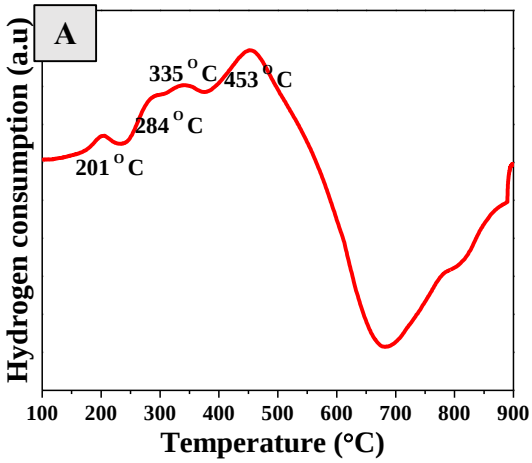


Figure 4S.6 Derivative TGA profiles of catalysts supported (**A**) inside the in situ nitrogen doped carbon and (**B**) on the post nitrogen doped carbon.



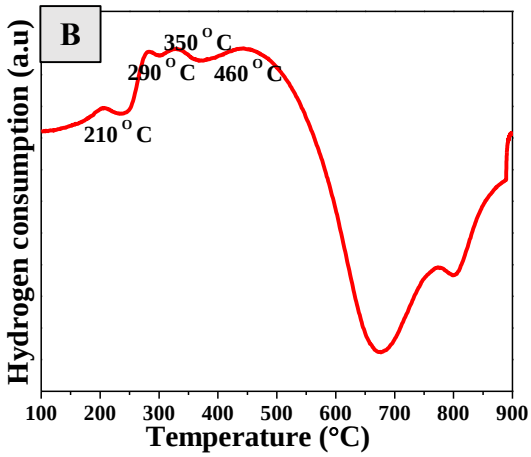


Figure 4S.7 TPR profiles of catalysts supported (**A &B**) of Co@NHCS$_{1hr.}$

Equation 4S.1 Scherrer's equation

$$\text{Particle size} = \frac{k\lambda}{\cos(\theta)(FWHM)}$$

Where, k is the shape factor, λ is the X-ray wavelenght, θ is the angle and FHWM is the full width half maxima.